INFORMATION TO USERS

This manuscript has been reproduced from the microfilm master. UMI films the text directly from the original or copy submitted. Thus, some thesis and dissertation copies are in typewriter face, while others may be from any type of computer printer.

The quality of this reproduction is dependent upon the quality of the copy submitted. Broken or indistinct print, colored or poor quality illustrations and photographs, print bleedthrough, substandard margins, and improper alignment can adversely affect reproduction.

In the unlikely event that the author did not send UMI a complete manuscript and there are missing pages, these will be noted. Also, if unauthorized copyright material had to be removed, a note will indicate the deletion.

Oversize materials (e.g., maps, drawings, charts) are reproduced by sectioning the original, beginning at the upper left-hand corner and continuing from left to right in equal sections with small overlaps.

Photographs included in the original manuscript have been reproduced xerographically in this copy. Higher quality 6" x 9" black and white photographic prints are available for any photographs or illustrations appearing in this copy for an additional charge. Contact UMI directly to order.

ProQuest Information and Learning
300 North Zeeb Road, Ann Arbor, MI 48106-1346 USA
800-521-0600

UMI®

Dissertation

A Resonant Ultrasound Spectroscopy Study of Metals, Alloys and Intermetallics.

Submitted by

Keir Foster

Physics Department

In partial fulfillment of the requirements
for the degree of Doctor of Philosophy

Colorado State University

Fort Collins, Colorado, USA

FALL 2001

COLORADO STATE UNIVERSITY

August 23rd, 2001

WE HEREBY RECOMMEND THAT THE DISSERTATION PREPARED UNDER OUR SUPERVISION BY KEIR FOSTER ENTITLED *A RESONANT ULTRASOUND SPECTROSCOPY STUDY OF METALS, ALLOYS AND INTERMETALLICS* BE ACCEPTED AS FULFILLING, IN PART, REQUIREMENTS FOR THE DEGREE OF DOCTOR OF PHILOSOPHY.

Committee on Graduate Work

Thesis Advisor

Department Chair

ABSTRACT OF DISSERTATION

A Resonant Ultrasound Spectroscopy Study of Metals, Intermetallics and Alloys

The experimental technique of Resonant Ultrasound Spectroscopy (RUS) has been successfully applied to three different systems in condensed matter physics. RUS can determine the full elastic constant tensor and the ultrasonic loss of a material. The results obtained would have been extremely difficult to achieve using more conventional acoustic techniques. The use of RUS has been expanded to investigate hydrogen motion in intermetallic and quasicrystalline hydrides.

The elastic moduli and ultrasonic loss of a C15 Laves-phase intermetallic compound, TaV_2H_x, were measured over a temperature range of 2.8 - 345 K, for a series of hydrogen concentrations, $x = 0.00$, 0.06, 0.10, 0.18, 0.34 and 0.53. Large ultrasonic loss peaks centered at roughly 240 K were observed for all hydrogen containing compounds, for measurement frequencies of about 1 MHz. Shifts in the resonant frequencies of the modes were also observed in the same temperature region. In a novel approach, both the loss and dispersion results were fit simultaneously to a Debye-type relaxation function to obtain parameters of the hydrogen motion, including activation energies, attempt frequencies and relaxation strengths. The results for the activation energies and attempt frequencies were in good agreement with those determined from

nuclear magnetic resonance measurements, for the concentration range where the two techniques overlapped. The present study was conducted over an extended concentration regime compared to that of the NMR work and weak concentration dependent effects were revealed. For the first time, evidence of two parallel Arrhenius processes occurring in this system was discovered with one of the processes being suppressed at higher H concentrations. The magnitude of the effects depended linearly on x implying that it is the relaxation of isolated H atoms that are contributing to the mechanical damping. The results appear to be the first to clearly demonstrate the existence of the so-called Snoek effect in intermetallic hydrides.

Similar measurements were made on the related compound, $TaV_2D_{0.17}$, and the results compared directly to those of $TaV_2H_{0.18}$. The $TaV_2D_{0.17}$ alloy also showed broad attenuation peaks centered at about 240 K which were interpreted in the same way as for the hydrogenated compounds. There was a weak isotope effect with the H hopping rate being somewhat faster than that of D. More importantly, a second, much weaker attenuation peak centered at approximately 20 K was observed for the deuterated compound which was completely absent in the loss data of $TaV_2H_{0.18}$. This peak was attributed to a rapid localized motion of D atoms. This work provided a particularly clear demonstration of a strong isotope effect in a metal-hydride system. Unlike the NMR results, the peaks attributed to the two frequency scales of D motion were separately resolved in temperature. This should aid in elucidating the physics behind these hopping mechanisms. The existence of a large isotope effect at low temperatures implies that the motion is dominated by quantum processes.

The magnitude and temperature dependence of shear elastic modulus $G(T)$ of the $TaV_2H(D)_x$ system was found to be highly dependent on x. $G(T)$ of TaV_2 anomalously increased with increasing temperature from 3 K to 350 K. The effect of adding hydrogen was both to systematically increase the magnitude of $G(T)$ and to completely reverse the temperature dependence for all $x \geq 0.17$. $G(T)$ of $TaV_2H_{0.53}$ was 55 % greater than that of the H free material at 20 K, representing an anomalously strong effect. The elastic constant results were quantitatively described by an electronic band structure model and constitute a remarkable and unusual example of a hydrogen-related electronic effect.

RUS measurements were made on a Ti-Zr-Ni based icosahedral quasicrystal (QC) and a related 1/1 bcc crystal approximant. The shear and bulk moduli were derived over a temperature range of 15 -345 K. The temperature dependencies resembled those of ordinary metals with the moduli of the QC and the approximant phase being almost the same, providing further confirmation of the similarity of the QC and approximant phases. These results represent the very first elastic moduli measurements on the large class of Ti-based QC systems. Both phases absorb hydrogen in solid solution up to H concentrations of $x \leq 1.7$. The ultrasonic loss of the QC and approximant phases for $x = 0.79$ and 0.20 respectively, was measured. Broad attenuation peaks were observed, centered at roughly 250 K for the hydrogenated materials. The peaks were associated with H motion and were fit with a Debye-type relaxation function. A Gaussian distribution of activation energies was required to fit the loss data, with a mean activation energy of 0.40 eV. The results indicated that the H motion in the QC, in this temperature range, is at least one order of magnitude faster than that of the approximant phase. This was the first time that

internal friction measurements have been utilized to derive information about H diffusion in a quasicrystalline system

In a final, more applied study, the texture of rolled sheets of copper and brass was investigated. Texture is related to the non-random orientation of crystallites within a polycrystalline aggregate. Rolled sheets are often assumed to possess macroscopic orthorhombic symmetry. RUS was used to measure all nine elastic moduli of the plates. The elastic constant results were then used to derive the orientation distribution coefficients. The ultrasonically derived values were in good agreement with those obtained by neutron diffraction, as evidenced by the remarkable similarity of the acoustic and neutron pole-figures. This work represented one of the most extensive studies of the suitability of ultrasonic techniques for texture characterization. The results support the idea that acoustic techniques may be used to determine the main features of texture in rolled plates.

Keir Foster
Physics Department
Colorado State University
Fort Collins, CO 80523

Fall 2001

Acknowledgments

There are, of course, a large number of persons whom I must thank for their contributions towards this thesis. First and foremost I must thank my advisor, Prof. Robert G. Leisure, for his knowledge, insights, patience and understanding: his all around support has been tremendous. I suggest that he perhaps think of starting a side-career in croquet sometime soon. I must also mention his wife, Jeanine Leisure and thank her for the delicious brunches, lunches and dinners which always helped revitalize a scrawny graduate student.

There are also a number of collaborators whom I must also acknowledge. We enjoyed an extremely fruitful partnership with Sasha Skripov (Urals Branch of the Academy of Sciences, Ekaterinburg, Russia) who supplied us with the Laves-phase hydride samples used for the project along with many useful insights into this system. A group from Washington University (St. Louis, MO) led by Prof. Ken Kelton provided us with the quasicrystalline samples. Groups from NIST (Boulder, CO) headed by H. Ledbtter and G. A. Alers also provided samples and a number of interesting discussions concerning RUS and related techniques.

I must acknowledge Dr. Frank Willis for helping me get started in the ultrasonics laboratory at Colorado State, and thank my fellow graduated student, Jennifer Hightower, for keeping me going ever since. I also applaud my friends from my starting class who

worked with me through those arduous first two years and who made it not only bearable, but fun; particularly Steve (the leave) Rehse, Rob (the drop) Dadamo, Anthony (the phantom) Glueck, Byron (the compass) Faber, Randy (the blanket) Blessing and Clare Weber.

Finally, I must simply thank my parents, Rosemary and John, for furnishing me with unlimited love, support and Cadbury's chocolate over the past six years.

Contents

CHAPTER 1: INTRODUCTION

1.1 Introduction 1

1.2 Review of Elasticity
- 1.2.1 Motivation 4
- 1.2.2 Basic Formalism: the elastic constants 6
- 1.2.3 Ultrasonic attenuation 11

1.3 Resonant Ultrasound Spectroscopy
- 1.3.1 Introduction 13
- 1.3.2 Other modulus measurement techniques 16
- 1.3.3 Returning to RUS 19
- 1.3.4 RUS: Theoretical background 21

REFERENCES 27

CHAPTER 2: EXPERIMENTAL DETAILS: RESONANT ULTRASOUND SPECTROSCOPY

2.1 Introduction 29

2.2 Sample Preparation 30

2.3 Electronic and Computer Algorithms 33

2.4 Analysis of Resonant Line shapes 35

2.5 Low-Temperature Systems 39

REFERENCES 51

CHAPTER 3: A RESONANT ULTRASOUND SPECTROSCOPY STUDY OF THE C15 LAVES-PHASE COMPOUND TaV_2H_x

3.1 Introduction: Metal-hydrogen Systems
3.1.1 Technological importance 52
3.1.2 Theoretical importance 55

3.2 Ultrasonic Attenuation and Dispersion Due to Hydrogen Motion in the C15 Laves-phase Compound TaV_2H_x
3.2.1 Introduction 63
3.2.2 Experimental details 69
3.2.3 Results and discussion 70
3.2.4 Concluding remarks 85

3.3 Ultrasonic Evidence for Strong Isotope Effects on the Local Motion of H(D) in $TaV_2H(D)_x$
3.3.1 Introduction 87
3.3.2 Experimental details 89
3.3.3 Results and discussion 90
3.3.4 Conclusions 99

3.4 Strong Hydrogen-related Electronic Effects on the Shear Elastic Modulus of $TaV_2H(D)_x$
3.4.1 Introduction 100
3.4.2 Experimental details 103
3.4.3 Results and discussion 106
3.4.4 Conclusions 125

3.5 Concluding Remarks 126

REFERENCES 128

CHAPTER 4: A RESONANT ULTRASOUND SPECTROSCOPY STUDY OF A Ti-Zr-Ni ICOSAHEDRAL QUASICRYSTAL AND A 1/1 BCC CRYSTAL APPROXIMANT

4.1 Background 135

4.2 Elastic Moduli of a Ti-Zr-Ni Icosahedral Quasicrystal and a 1/1 bcc Crystal Approximant
4.2.1 Introduction 139
4.2.2 Experimental details 141

4.2.3 Results and discussion 142
4.2.4 Conclusions 150

4.3 Ultrasonic Study of Hydrogen Motion in a Ti-Zr-Ni Icosahedral Quasicrystal and a 1/1 bcc Crystal Approximant
4.3.1 Introduction 151
4.3.2 Experimental details 153
4.3.3 Results and discussion 154
4.3.4 Conclusions 160

4.4 Summary 161

REFERENCES 163

CHAPTER 5: ACOUSTIC STUDY OF TEXTURE IN POLYCRYSTALLINE

5.1 Introduction 166

5.2 Theoretical Background
5.2.1 Anisotropic elasticity and ODCs 168
5.2.2 Acoustic pole plots 172

5.3 Experimental Details 175

5.4 Results and Discussion 176

5.5 Conclusions 184

REFERENCES 186

CHAPTER 6: CONCLUSIONS 187

Chapter 1

Introduction

- **1.1 Introduction**
- **1.2 Review of Elasticity**
- **1.3 Resonant Ultrasound Spectroscopy**
- **References**

1.1 Introduction

In this thesis, the development and application of a novel experimental technique, resonant ultrasound spectroscopy (RUS), to a number of different systems in condensed matter physics will be detailed. The RUS technique [1][2][3][4] utilizes the mechanical resonance spectrum of samples of specific geometries to determine the full elastic modulus tensor of a specimen. The ultrasonic loss in the material can be derived simultaneously from the quality factor (Q) of the resonant line-shapes.

The following section of chapter 1 will present a review of the theory of the elasticity of solids. Section 1.3 will describe the basic theoretical and experimental considerations involved with the RUS technique. The advantages and disadvantages of the RUS technique over more conventional ultrasonic techniques will be highlighted.

Chapter 2 will discuss the experimental details specific to the RUS measurements made at Colorado State. The design and operation of the cryogenic systems used to make

RUS measurements at low temperatures will also be discussed.

Chapter 3 presents results of a series of RUS measurements made on the C15 Laves-phase compounds TaV_2H_x (x = 0.00, 0.06, 0.10, 0.18, 0.34 and 0.53). Both chapters 3 and 4 present research on metal-hydrogen systems so section 3.1 will introduce a brief historical and theoretical review of this rich field of study. Measurements on TaV_2H_x were made over a temperature range of 0.3 - 350 K. This system proved to be particularly fascinating, displaying a rich variety of unusual features in both the elastic moduli and ultrasonic loss results. Ultrasonic loss measurements showed broad attenuation peaks centered at roughly 240 K for all $x > 0.00$. These peaks were associated with local jumps responsible for the long range diffusion of H about interstitial sites within the host C15 lattice [5][6]. Parameters for the H motion including activation energies, attempt frequencies and relaxation strengths were determined. The results compare favorably to those determined from NMR proton spin-lattice experiments [7].

To explore for possible isotope effects in this system, measurements were made on $TaV_2D_{0.17}$ and the results compared directly to those of $TaV_2H_{0.18}$. The attenuation results for $TaV_2D_{0.17}$ showed similar peaks to those observed for the hydrogenated sample at ≈ 240 K but a second, much smaller peak, was also observed at lower temperatures centered at ≈ 20 K. Remarkably, this peak was completely absent in the loss data for $TaV_2H_{0.18}$. The existence of a strong isotope effect on the H motion, particularly at low temperatures, indicated that the second process was almost certainly of a quantum origin [8]. The second process has been related to rapid localized quantum tunneling of H(D) atoms occurring concurrently with the slower rate-limiting motion described above.

A rather unusual behavior in the aggregate shear modulus C_{44} (G) was observed for these compounds. The shear moduli of the hydrogen free material anomalously increased with increasing temperature across the entire temperature range of study. The effect of adding hydrogen to TaV_2 was two-fold. Firstly, the magnitude of $G(T)$ increased strongly with increasing x. At 20 K the shear modulus of $TaV_2H_{0.53}$ was roughly 55 % greater than that of the hydrogen free alloy. Secondly, the temperature dependence of $G(T)$ systematically shifted with increasing x so that for concentrations of $x > 0.18$ a normal softening with increasing temperature was observed. Both the changes in the magnitude and temperature dependence of $G(T)$ were successfully described in terms of an electronic band structure effect [9][10][11].

Chapter 4 will discuss some of the first ultrasonic measurements made on a Ti-based quasicrystal system. RUS was used to derive the elastic moduli of a Ti-Zr-Ni based *i*-phase quasicrystal and *W*-phase crystal approximant over a broad temperature range. The elastic moduli of both materials exhibited normal stiffening with decreasing temperature and were of almost the same magnitude throughout the temperature range of study [12]. These results constitute the first determination of the elastic moduli of a Ti-based quasicrystalline system.

It has been shown that both the Ti based quasicrystal and approximant absorb hydrogen to rather high concentrations (hydrogen to metal atoms ratios of up to H / M = 1.88) and have generated some interest as hydrogen storage materials [13]. Ultrasonic attenuation measurements were made on hydrogenated samples of both materials and the results related to mechanisms of hydrogen diffusion within the host lattice. These

experiments were the very first internal friction measurements conducted for the purpose of elucidating hydrogen dynamics in a quasicrystalline system [14].

Chapter 5 describes the application of RUS to the characterization of 'texture' in polycrystalline rolled-sheets of copper and brass. Texture is related to the non-random distribution of the orientation of crystallites within an aggregate. Neutron and x-ray techniques can determine the texture of a polycrystalline system to high precision, but it was shown that the significant features of texture in rolled sheets of copper and brass could be characterized with RUS in a non-destructive and relatively time and cost efficient manner. The RUS results were directly compared to neutron measurements on the same materials [15].

Finally chapter 6 summarizes and concludes the findings of the project.

1.2 Review of Elasticity

1.2.1 Motivation

An understanding of the elastic properties of solids is significant both for theoretical and practical considerations [16]. The elastic behavior of a body is directly related to the interactions of atoms and electrons comprising the solid. Quantitative knowledge of the elastic properties can be used in theoretical calculations of interatomic potentials. Ultimately any process within a solid that couples to the lattice can affect a material's elasticity, although the dominating factor is the magnitude and directionality of the interatomic forces. For example, in some materials there can be a strong coupling between an applied strain and the conduction electrons. Measurements of sound velocities

and attenuation in solids can be used to investigate the physics of phase transitions. At a second-order phase transition there may be discontinuities in the elastic moduli, while many thermodynamic quantities may show no obvious evidence of a change. The change in the elastic constants may then be related to physical mechanisms driving the phase transition. For example, various experimental techniques have been used to study the changes in elasticity exhibited at high-temperature superconducting phase transitions [17]. The dynamics of point defects (e.g. light interstitials) or of dislocations also have a significant influence on a material's elastic properties [18].

The elastic constants of a material quantify the nature of the response (strain) of a solid to an external applied force (stress). As will be shown in section 1.2.2 the elastic constants can be considered the 3-d analogue of the spring constant '*k*' familiar from Hooke's law. As second derivatives of a thermodynamic potential the elastic constants are directly related to the solid's thermodynamic properties such as specific heat. Debye temperature and Grüneisen's parameter. A knowledge of the elastic constants as a function of temperature and / or pressure is used in determining the equation of state of a material. The temperature dependence of the elastic constants arises directly from the anharmonic nature of the lattice vibrations though other effects (electronic) may be important in some systems. The velocities of mechanical waves in solids depend entirely on the elastic constants and mass density. Structural engineers use the elastic constants to calculate fundamental and applied parameters of the material including the bulk modulus, Young's modulus, shear modulus, Poison's ratio, load deflection, fracture toughness, residual stress, texture and ductility.

Hopefully the reader has been persuaded that the elastic constants are of importance to a wide variety of theoretical and applied fields of research.

1.2.2 Basic formalism: the elastic constants

A body is deformed when external forces are applied to it. An elastic body is defined as one in which the body returns to its original configuration after the removal of such external forces. The return to the original state arises from the response to internal stresses generated within the body by the application of external forces responsible for the deformation.

The deformation (strain) tensor:

It can be shown [19][20] that the deformation of a solid body can be described by a 3-dimensional tensor of rank 2, ε_{ij}, given by,

$$\varepsilon_{ij} = \frac{1}{2}\left(\frac{\partial u_i}{\partial x_j} + \frac{\partial u_j}{\partial x_i}\right) \tag{1}$$

where u_i are the components of the displacement vector for a point in the body with position components x_i ($i, j, k = 1, 2, 3$). This form of the deformation tensor applies only for small strains. Clearly, the right-hand side of **Eq.** (1) is invariant to the permutation of the i and j indices. Thus ε_{ij} is symmetric, containing just 6 independent components.

$$\varepsilon_{ij} = \varepsilon_{ji} \tag{2}$$

A strain ε_{ij} represents a movement in the i direction of a plane of atoms with plane

normal in the j direction.

The stress tensor:

If a material is homogeneously stressed then every volume element within the body will experience a force acting at the boundary surface. Let a force of component ΔF_i act on an element of surface ΔA_j (perpendicular to the j axis). The stress tensor σ_{ij} can then be defined [19][20] by

$$\sigma_{ij} = \lim_{\Delta A_j \to 0} \frac{\Delta F_i}{\Delta A_j} \tag{3}$$

Fedorov [19] shows that the stress tensor is symmetric with respect to the reversal of the 2 subscripts in the absence of an externally applied net torque. The stress tensor also contains just 6 independent components. A stress σ_{ij} represents an applied force per unit area in the i direction on a plane of atoms with plane-normal in the j direction. Those stresses where $i = j$ are related to the volume compression / expansion of a body and those stresses where $i \neq j$ are the shear stresses.

The elastic constants:

The usual starting point in linear elastic theory is the basic postulation of Hooke's law [19][20] which states that for sufficiently small strains, there is a linear relationship between the components of the stress and deformation tensors,

$$\sigma_{ik} = c_{iklm}\varepsilon_{lm} \tag{4}$$

where $i, j, k, l = 1, 2, 3$. The usual summation over repeated subscripts is assumed throughout. The set of c_{iklm} form a fourth-rank tensor which is referred to as the tensor of the elastic constants. The individual components of the tensor are called the elastic constants. They have dimensions of force per unit area and in this thesis will be expressed in units of GPa. A similar relationship expressing the stress in terms of the deformation tensor can be written

$$\varepsilon_{ik} = s_{iklm}\sigma_{lm} \tag{5}$$

The components of s_{iklm} are referred to as the moduli of compliance. Both the elastic and compliance moduli are quoted commonly in the literature.

Symmetry considerations:

Eqs. (4) and (5) are both written in 'full' notation. It would appear that as c_{iklm} is a 3-dimensional 4th rank tensor there should be $3^4 = 81$ independent elastic moduli. However, after considering [19][20] a series of symmetry arguments the total number is reduced to a maximum of 21 even for the lowest symmetry crystal class (monoclinic).

It can be shown that the elastic moduli are given by the second derivative of a thermodynamic potential Φ with respect to strain [19][20]. For the adiabatic and isothermal elastic constants the appropriate thermodynamic potential is the internal energy and Helmholtz free energy respectively. Due to the symmetric nature of the second derivative,

$$c_{ilkm} = \frac{\partial^2 \Phi}{\partial \varepsilon_{ik} \partial \varepsilon_{lm}} = \frac{\partial^2 \Phi}{\partial \varepsilon_{lm} \partial \varepsilon_{ik}} = c_{lmik} \tag{6}$$

it can be seen that the elastic constants are also invariant to the exchange of subscript pairs as shown. The minimum of the energy with respect to the atomic positions defines the atomic structure. The elastic constants clearly represent the curvature (in space) of the free energy about this minimum. The elastic energy of a deformed body is given by,

$$\Phi = \frac{1}{2} c_{ilkm} \varepsilon_{ik} \varepsilon_{lm} \tag{7}$$

By considering the symmetry relation of **Eq.** (6) and the symmetry of the stress and strain tensors themselves it becomes apparent that the 3-dimensional fourth-rank tensor of the elastic constants can be transformed into a 6-dimensional matrix. This is done by replacing the indices 1, 2 and 3 with ones taking values of 1, 2, 3, 4, 5 and 6 and by considering the symmetry of the pairs, as follows:

$$\begin{gathered} (11) \leftrightarrow 1 \quad (22) \leftrightarrow 2 \quad (33) \leftrightarrow 3 \\ (23) = (32) \leftrightarrow 4 \quad (31) = (13) \leftrightarrow 5 \quad (12) = (21) \leftrightarrow 6 \end{gathered} \tag{8}$$

Following the convention used by Fedorov [19] Greek indices α and β are now used as subscripts in the 6-dimensional formalism. Hooke's law and the elastic energy of a body are now conveniently expressed as

$$\sigma_\alpha = c_{\alpha\beta} \varepsilon_\beta \tag{9}$$

$$\Phi = \frac{1}{2} c_{\alpha\beta} \varepsilon_\alpha \varepsilon_\beta \tag{10}$$

where summation over repeated Greek subscripts is assumed. From **Eq.** (6) it can be seen

that the six-dimensional elastic constant matrix is symmetric

$$c_{\alpha\beta} = c_{\beta\alpha} \tag{11}$$

and takes the following form, with 21 independent components

$$C = c_{\alpha\beta} = \begin{pmatrix} c_{11} & c_{12} & c_{13} & c_{14} & c_{15} & c_{16} \\ c_{12} & c_{22} & c_{23} & c_{24} & c_{25} & c_{26} \\ c_{13} & c_{23} & c_{33} & c_{34} & c_{35} & c_{36} \\ c_{14} & c_{24} & c_{34} & c_{44} & c_{45} & c_{46} \\ c_{15} & c_{25} & c_{35} & c_{45} & c_{55} & c_{56} \\ c_{16} & c_{26} & c_{36} & c_{46} & c_{56} & c_{66} \end{pmatrix}. \tag{12}$$

The total number of elastic constants required to fully describe the elastic response of a crystal to an applied stress depends upon the symmetry of the crystal. By considering the appropriate symmetry elements of a crystal structure the number of independent elastic constants is systematically reduced [19][20]. In the simplest possible case, for isotropic media, only 2 independent elastic moduli are required. In an isotropic material the velocity of shear and longitudinal sounds waves are independent of the direction of propagation. Usually the Lamé constants λ and μ are the moduli quoted in the literature. The shear constant μ replaces c_{44}, c_{55} and c_{66} and λ replaces c_{12}, c_{23} and c_{13}. Figure 1.1 presents the full elastic constant tensor for isotropic, cubic and orthorhombic crystal symmetries, requiring 2, 3 and 9 independent elastic constants respectively.

1.2.3 Ultrasonic attenuation

The attenuation of sound in a material, the exponential decrease in sound intensity with propagation, raises many practical and interesting questions. Sound attenuation is another key parameter in describing the elastic response of a media and is directly related to the ratio of the imaginary to real component of the elastic constant.

In solids the attenuation of sound arises from a variety of mechanisms, including interaction with thermal phonons, conduction electrons, dislocations, line-defects, structural phase-changes, superconductivity and relaxation-attenuation effects. The latter concerns the relaxation of light interstitials, point defects or vacancies under the influence of the applied time-varying strain [18]. Many of these effects depend strongly on frequency. As a practical example, the understanding of these mechanisms has been key in the development of metallic high-damping materials (HIDAMMETs) used for vibrational isolation. Of more theoretical interest, mechanical damping measurements have been used quite extensively to probe the motion of light interstitials in metals and intermetallic compounds.

1.3 Resonant Ultrasound Spectroscopy

1.3.1 Introduction

The experimental technique of resonant ultrasound spectroscopy [1][2][3][4] utilizes the mechanical resonances of solids to determine the elastic constants and ultrasonic attenuation. The vibrational eigen-modes of samples of well defined shapes

$$C_{isotropic} = \begin{pmatrix} \lambda+2\mu & \lambda & \lambda & 0 & 0 & 0 \\ \lambda & \lambda+2\mu & \lambda & 0 & 0 & 0 \\ \lambda & \lambda & \lambda+2\mu & 0 & 0 & 0 \\ 0 & 0 & 0 & \mu & 0 & 0 \\ 0 & 0 & 0 & 0 & \mu & 0 \\ 0 & 0 & 0 & 0 & 0 & \mu \end{pmatrix}$$

(a)

$$C_{cubic} = \begin{pmatrix} c_{11} & c_{12} & c_{12} & 0 & 0 & 0 \\ c_{12} & c_{11} & c_{12} & 0 & 0 & 0 \\ c_{12} & c_{12} & c_{11} & 0 & 0 & 0 \\ 0 & 0 & 0 & c_{44} & 0 & 0 \\ 0 & 0 & 0 & 0 & c_{44} & 0 \\ 0 & 0 & 0 & 0 & 0 & c_{44} \end{pmatrix}$$

(b)

$$C_{ortho} = \begin{pmatrix} c_{11} & c_{12} & c_{13} & 0 & 0 & 0 \\ c_{12} & c_{22} & c_{23} & 0 & 0 & 0 \\ c_{13} & c_{23} & c_{33} & 0 & 0 & 0 \\ 0 & 0 & 0 & c_{44} & 0 & 0 \\ 0 & 0 & 0 & 0 & c_{55} & 0 \\ 0 & 0 & 0 & 0 & 0 & c_{66} \end{pmatrix}$$

(c)

Figure 1.1: Elastic modulus tensor for a) isotropic, b) cubic, and c) orthorhombic symmetry crystals; requiring 2, 3 and 9 independent elastic moduli respectively. The isotropic tensor is given in terms of the Lamé constants, λ and μ.

(cubes, spheres, rectangular parallelepipeds) are measured. If the crystal symmetry, mass density and sample orientation are known the full elastic constant tensor can be determined to high accuracy, potentially for a crystal of any symmetry. The ultrasonic attenuation is determined from the quality factor (Q) of the resonant modes. Low-loss materials produce sharp, high Q resonances and conversely high-loss materials produce much broader resonant line-shapes.

The RUS sample is mounted corner to corner between two piezo-electric transducers as shown in figure 1.2. Care is taken to insure that the contact force is minimized so that the assumption of stress-free boundary conditions is best approximated. The frequency of the driving transducer is swept across a suitable range. Typically for sample sizes of 1 - 2 mm the lower frequency resonances occur in the range of 400 kHz to 4 MHz. When the driving transducer approaches a natural frequency of the sample a large response will be detected by the receiving transducer. A typical resonance spectrum is shown in figure 1.3. This spectrum was taken at Colorado State on the C15 Laves-phase alloy $TaV_2H_{0.06}$ at 155 K. Typically 40 - 50 of the lowest frequency modes are measured and used to derive the elastic moduli. Section 1.3.4 will outline the theoretical framework used to calculate the resonant frequencies and derive the elastic constants. Chapter 2 will discuss in detail the experimental apparatus and techniques used for RUS measurements at Colorado State.

1.3.2 Other modulus measurement techniques

Before discussing the RUS technique further, let us briefly consider some of the

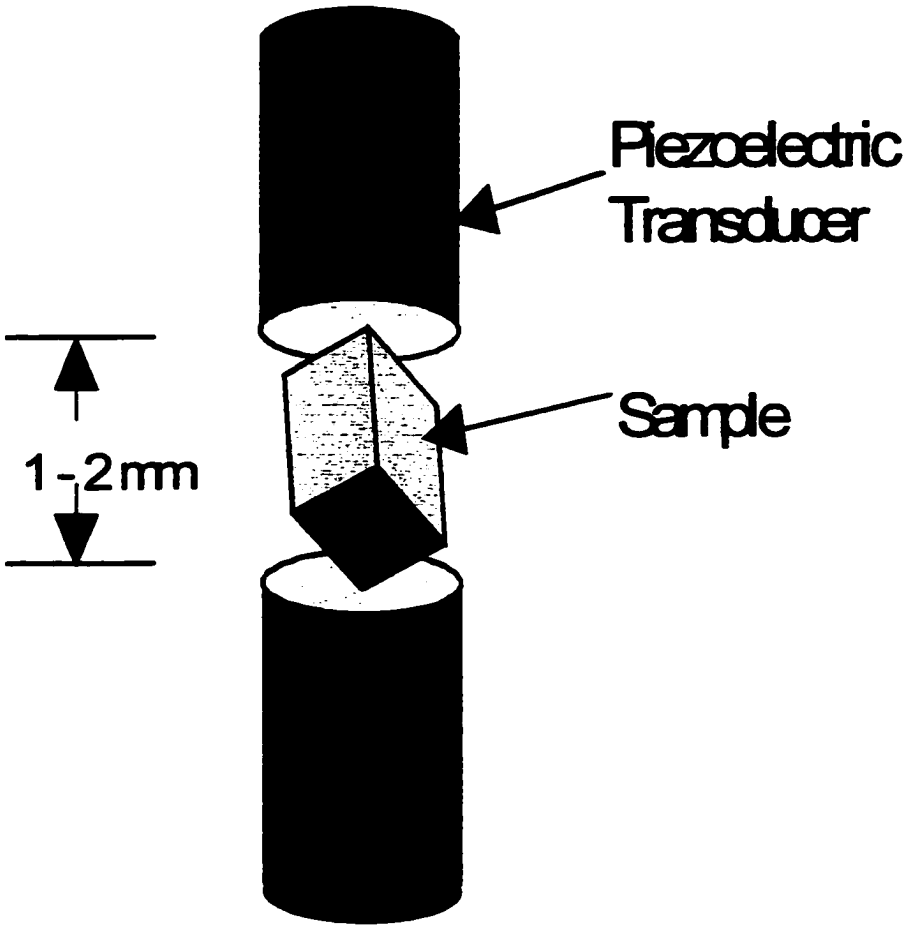

Figure 1.2: Basic schematic of the sample-transducer configuration used in the RUS technique.

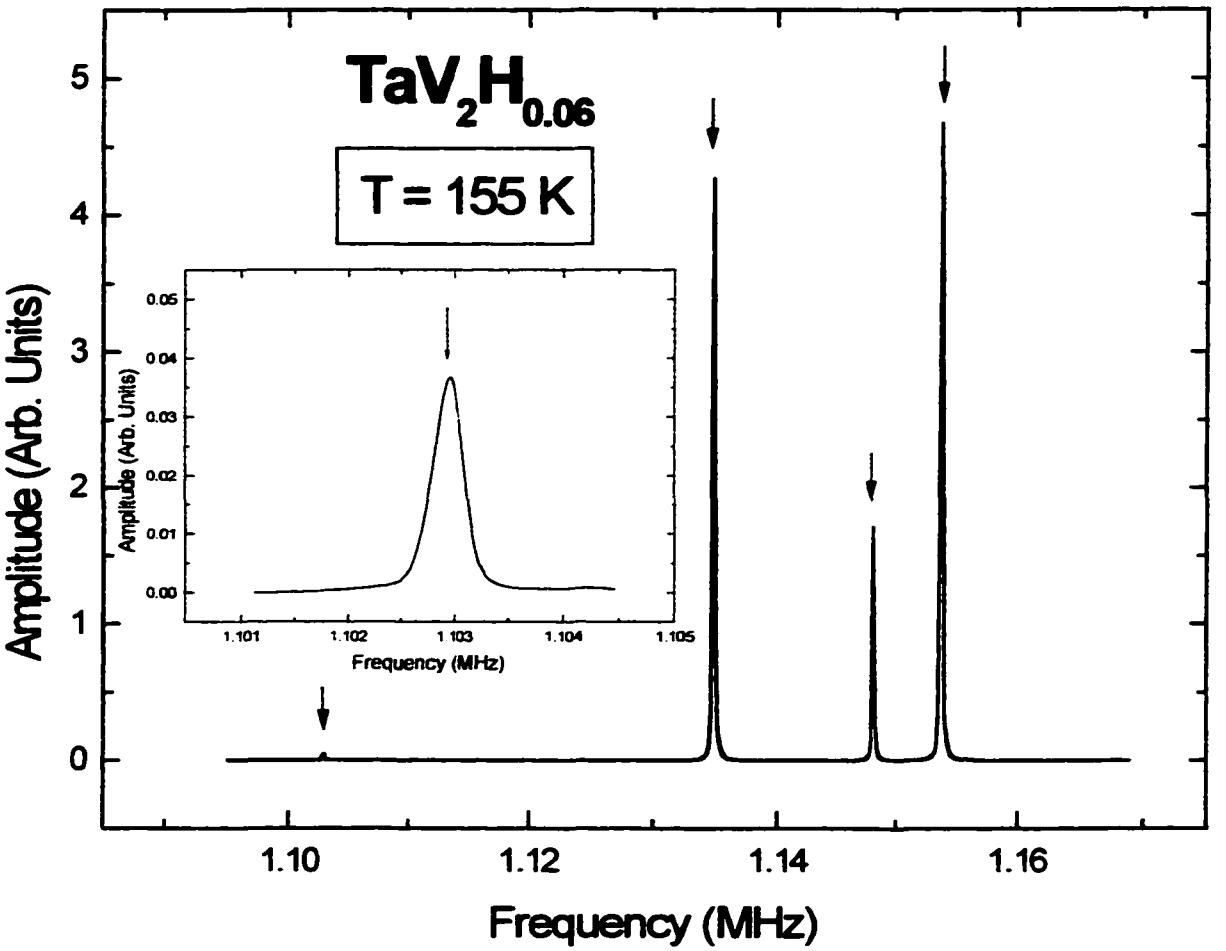

Figure 1.3: Section of a typical resonance spectrum. Three strong modes are observed with one much weaker mode, highlighted in the insert, at 1.103 MHz. This spectrum was taken at Colorado State on the C15 Laves-phase intermetallic alloy $TaV_2H_{0.06}$.

more traditional techniques used to measure the elastic constants. By discussing some of the limitations and indeed advantages of these techniques the importance of RUS can be put into perspective.

The pulse-echo technique [21][22] was perhaps the most widely used method of determining the elastic moduli in solids. The basic experimental arrangement is shown in figure 1.4. One or two transducers are bonded on opposite faces of the sample. Key to the success of the experiment is that opposite faces are both highly parallel and flat. One transducer is excited by an electromagnetic pulse, sending ultrasonic vibrations through the material. The ultrasonic pulse then 'reverberates' backwards and forwards across the sample and the echoes are detected by one or both transducers. The sound velocity is determined simply from the time of flight and sample thickness. The attenuation is found from the exponential decay of the ultrasonic echo amplitude. The elastic moduli are calculated from the sound velocities and from the mass density of the material.

A continuous wave technique uses the same experimental set-up as that shown in figure 1.4 and has been used to measure both the attenuation and elastic moduli of solids. Instead of sending an ultrasonic pulse into the sample, the driving transducer is driven continuously and the resonant response observed. These occur where the sample thickness is some multiple of one half the wavelength of the ultrasound (analogous to the standing waves of a 1-d string fixed at both ends). The sound velocity and attenuation are determined from the frequencies and quality factors of the resonances respectively.

The relationship between the sound velocities and the elastic constants is fairly simple for high symmetry systems but becomes rapidly more complex for lower symmetry

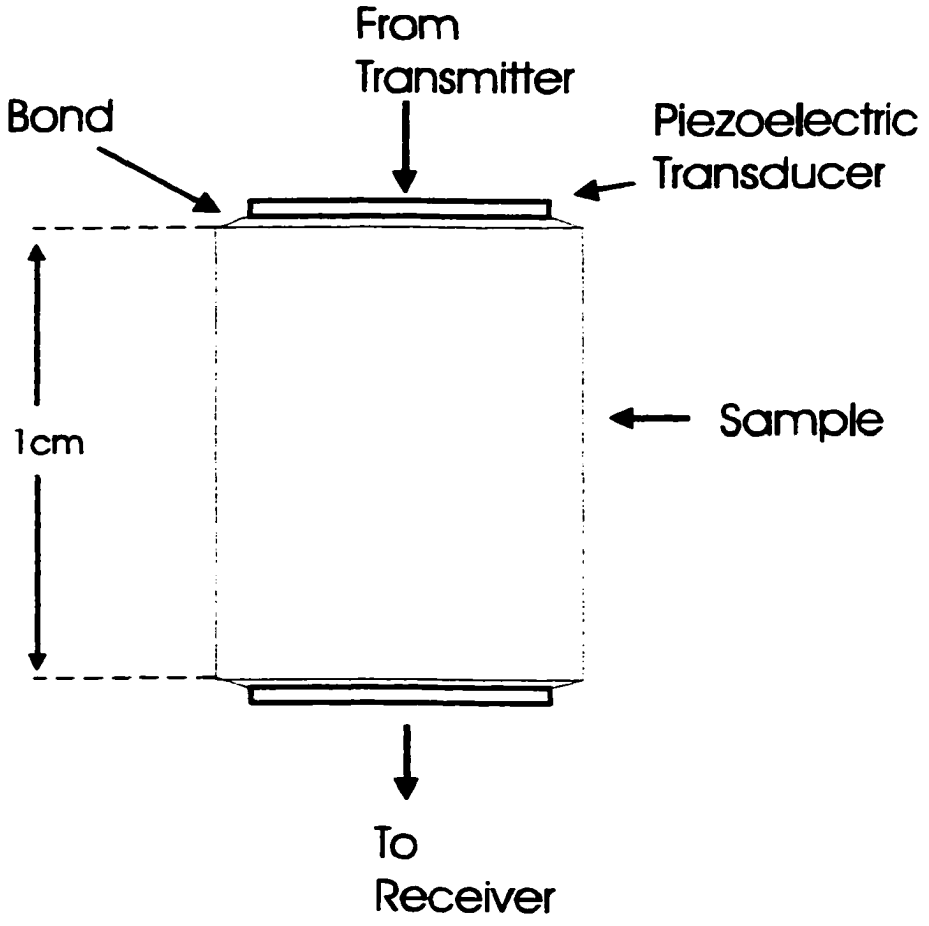

Figure 1.4: Simple schematic of the sample-transducer arrangement used in conventional ultrasonic techniques, such as pulse-echo or standing-wave resonance.

crystals. The sound velocities depend on some linear combination of elastic constants. For example, for orthorhombic crystals nine velocity measurements are required to obtain the full elastic constant tensor. These measurements must be made along six different crystallographic directions. This requires 6 samples, each with a different orientation between the crystallographic axes and the polished faces. This involves considerable effort and perhaps more importantly, rather large quantities of material. The quantity of material required may simply not be available. For this reason both the above techniques are more suited to measuring the elastic parameters of high symmetry crystals, which they do to high accuracy.

Both techniques assume plane-wave solutions to the wave equation in the analysis. The plane wave approximation that is assumed generates a series of difficulties. Firstly, the diameter of the transducers must be much greater than the wavelength of sound in the sample. Sound typically propagates at 10^3 m/s in most metals and this leads to typical transducer diameters of at least 1 cm for measurements at MHz frequencies. Furthermore, the sample dimensions must then be somewhat larger than that of the transducer to minimize diffraction effects. It can often be difficult to impossible to obtain good quality single crystals of this size. Diffraction effects will always be present to some degree in experiments of this nature, limiting the quality of sound velocity and attenuation measurements. The physical bonding of the transducer to the crystal of interest creates further difficulties. The agent used for bonding can introduce non-parallelism of the end faces or produce coupling losses which can further affect the results. Also, by physically adding material to the surface of a crystal the natural resonant response of the sample may

be affected.

In almost all materials the speed of sound is frequency dependent, though usually quite weakly. The transmitted pulse in a pulse-echo experiment will always have some finite bandwidth. This leads to dispersive effects that can further complicate the interpretation of the results. The dispersive effects, non-parallelism of opposite faces and sound-scattering centers (e.g. dislocations, grain boundaries) all act to reduce the intensity of the propagating sound waves. These effects act as extrinsic sources of loss reducing the accuracy of the attenuation measurement.

To summarize, both techniques certainly have an important place in determining the moduli and ultrasonic loss of solids but are particularly suited to higher symmetry crystals.

1.3.3 Returning to RUS.

RUS offers some advantages over many of the techniques mentioned above. Perhaps the greatest asset of all is that RUS can be applied to sub-millimeter sized samples. RUS can study samples three orders of magnitude smaller than the conventional acoustic methods. This vastly increases the range of novel and exciting materials which can be studied ultrasonically. A second advantage of RUS is that it does not assume a plane wave approximation because there are no plane waves present in a freely vibrating sample. Diffraction effects are irrelevant in the context of RUS. Another favorable quality stems from the fact that there is no direct bond between transducer and sample, although there is light contact between the sample corner and transducer. The absence of

a direct bond is especially significant for temperature-dependent work where differential thermal expansion can result in strains being introduced into a sample, or in extreme cases the fracture of the bond itself. This can be especially significant for materials undergoing a structural phase transition involving large changes in unit cell dimensions. Finally, the RUS technique can determine *all* the elastic moduli of a sample to high accuracy, even for crystals of low symmetry, from a single resonance spectrum on a single sample. Therefore, inaccuracies associated with making measurements on multiple samples are avoided. Chapter 5 of this work details how RUS was used to measure all nine elastic moduli for a system of orthorhombic symmetry.

Let us consider RUS and the measurement of ultrasonic attenuation. Poor geometry of the RP samples *will* considerably shift the resonant frequencies but does not affect the Qs of the line-shapes; whereas the non-parallelism of opposite faces in a pulse-echo sample will affect the derived loss value. Attenuation experiments have been performed at Colorado State on small irregularly shaped pieces of material. Scattering centers will also act to shift resonant frequencies, but again do not affect the attenuation measurement. However there are some negative considerations. A RUS sample is in contact with two transducers supporting it. In turn, these transducers must be supported by something else. This provides an acoustic pathway for sound transmitted into the sample, to leave the sample, which effectively acts as an extrinsic source of loss. As the transducers of a pulse-echo experiment are in 'full' contact with the sample they do not need to be supported in the same way. The electrical leads are typically made as small as possible and do not provide an effective means of sound propagation away from the

sample. Ultimately a well designed pulse-echo experiment can reduce the sound propagation away from the sample to negligible amounts. With RUS there is also coupling between the resonating sample and the gas surrounding it, particularly for volume-changing modes. The vibrations of the sample produce longitudinal sound waves in the gas taking energy away from the sample. This is another effect which adds to the measured ultrasonic loss but which is not the true 'interesting' intrinsic thermodynamic attenuation.

The details of how, at Colorado State, we have reduced significantly the sound propagation through the RUS jig and the surrounding gas will be outlined in chapter 2.

1.3.4 RUS: Theoretical background

From the frequencies of the resonant modes the elastic constant tensor can be determined. The process by which the elastic constants are derived from the frequencies is referred to as the inverse problem in RUS. The 'inverse' calculation requires the eigen-frequencies for a sample of a given crystal symmetry, shape, elastic constants and mass density to be accurately and rapidly calculated. The calculation of the natural resonances of a freely vibrating body is referred to as the 'forward' problem.

It is interesting to note that the geophysics community provided much of the initial impetus in developing the RUS technique [3][23][24]. They were interested in understanding the normal modes of vibration of the earth itself. Resonant techniques have also been used in the geophysics community to measure the elastic properties of rocks, often at high temperatures, in order to better interpret seismic data. However, it wasn't

until a group at Los Alomos National Laboratory (LANL) [1][2][17] adopted the technique to analyze resonance measurements on superconducting materials, that the technique was introduced into mainstream physics. The technique was rapidly extended by the LANL group [1][2][17] particularly in terms of the low-noise electronics and computer algorithms required.

The computational aspects of the forward and inverse problems will not be discussed in detail here as they have been covered thoroughly elsewhere [1][2][3][4][17][25], but a short theoretical overview is provided.

By considering the forces acting on an infinitesimal cube of volume dxdydz the equations of motion can be derived. Neglecting body forces, Newton's second law for the cube becomes

$$\frac{\partial \sigma_{ij}}{\partial x_j} = \rho \frac{\partial^2 u_i}{\partial t^2} \tag{13}$$

where ρ is the mass density. Combining Eqs. (1), (4) and (13) we obtain the equation of motion for a linear elastic solid

$$c_{ijkl} \frac{\partial^2 u_k}{(\partial x_j \partial x_l)} = \rho \frac{\partial^2 u_i}{\partial^2 t}. \tag{14}$$

Finding the natural resonant frequencies of a finite elastic solid is a long-standing problem in applied physics. The classical approach to such a problem would be solve Eq. (14) analytically for a specific set of boundary conditions. Exact analytical solutions to Eq.

(14) have not been found except for very specific high symmetry cases. As early as 1880 Lamé and Lamb found that analytical solutions to the forward problem were possible for elastically isotropic spheres. Solving **Eq.** (14) for crystalline solids, of more general shape, has proved considerably more difficult and significant progress was not made until the advent of the digital computer in the 1960's. Numerical methods, using the Lagrangian *(L)* of a 3-d solid as the starting point, have proven to be the successful approach [3]. The vector nature of **Eq.** (14) provides the main obstacle in solving the free-vibration problem for elastic solids. It was suggested that it may be advantageous to formulate the problem with a variational principle approach, based on scalar quantities such as the potential and kinetic energies [1][2][26]. With this notion in mind consider the general form of L for a 3-d solid

$$L = \int_V (T - U) dV \tag{15}$$

where T and U are the kinetic and potential energy densities respectively, given by

$$T = \frac{1}{2} \sum_i \rho \omega^2 u_i^2, \tag{16}$$

and

$$U = \frac{1}{2} \sum_{i,j,k,l} c_{ijkl} \frac{\partial u_i}{\partial x_j} \frac{\partial u_k}{\partial x_l}. \tag{17}$$

This applies to an arbitrarily shaped solid with volume V, enclosed in a surface S and with

linear elastic moduli c_{ijkl} and density ρ. A harmonic time-dependence was assumed for the displacements i.e. $u(t) = u_0 e^{i\omega t}$. The summation on indices i, j, k, and l run from 1 to 3, corresponding to the three spatial directions.

To find the minimum in the Lagrangian the variation in L (δL) is calculated by allowing the displacements u to vary arbitrarily in V and on S ($u_i \rightarrow u_i + \delta u_i$),

$$L + \delta L = \int_V \left[\frac{1}{2} \sum_i \rho \omega^2 (u_i + \delta u_i)^2 - \sum_{i,j,k,l} c_{ijkl} \frac{\partial (u_i + \delta u_i)}{\partial x_j} \frac{(\partial u_k + \delta u_k)}{\partial x_l} \right] dV. \quad (18)$$

Keeping terms to first order in δu_i and after integrating by parts [1][24], we find

$$\delta L = \int_V \left(\sum_i \left[\rho \omega^2 u_i + \sum_{j,k,l} c_{ijkl} \frac{\partial^2 u_k}{\partial x_j \partial x_l} \right] \delta u_i \right) dV - \int_S \left(\sum_i \left[\sum_{j,k,l} \vec{n}_j c_{ikjl} \frac{\partial u_k}{\partial x_l} \right] \delta u_i \right) dS. \quad (19)$$

The stationary points of L, where $\delta L = 0$, for arbitrary δu_i can only occur if the terms in square brackets of Eq. (19) are independently zero. A quick examination of the first square-bracketed term reveals the elastic wave equation. The second square-bracketed term yields an expression denoting stress-free boundary conditions,

$$\sum_{j,k,l} \vec{n}_j c_{iklj} \frac{\partial u_k}{\partial x_l} = \sum_j \vec{n}_j \sigma_{ij} = 0, \quad (20)$$

where σ_{ij} is recognized as the ij th component of the stress tensor from Eq. (4).

The key point here is that it has been shown that those displacements u_i for which

the Lagrangian is a minimum, are exactly those displacements which are a solution to the elastic wave equation with stress free boundary conditions, i.e. the set of u_i which correspond to ω being one of a discrete set of normal mode frequencies of free vibration of the solid [1].

This allows for the following general scheme, referred to as the Ritz method. The displacements are expanded in some suitable complete set of basis functions [1][2][3][4],

$$u_i = \sum_{\lambda} a_{i\lambda} \Psi_{\lambda}. \tag{21}$$

P. S. Spoor provides an excellent review of the considerations involved in deciding on a suitable set of basis functions [26]. The set which were found to be applicable to the largest variety of sample shapes was proposed by Vissher *et al.* [27] and is based on simple powers of cartesian coordinates,

$$\Psi_{\lambda} = x^l y^m z^n. \tag{22}$$

Eqs. (21) and (22) are inserted into **Eq.** (15) and the derivatives of the Lagrangian with respect to the expansion coefficients are set equal to zero, to determine the extremum. As demonstrated above, by finding those displacements which make the Lagrangian stationary, we are, in effect, solving the free-vibration problem. This ultimately leads to a generalized eigenvalue problem [1][2][4][26] in which the potential and kinetic energies are represented by quite large matrices: the eigenvalues and eigenvectors are determined numerically and represent the resonant frequencies and displacements respectively.

The inverse problem uses a standard non-linear least-squares algorithm (Levenburg-Marquardt algorithm). The elastic constants are adjusted in an iterative

process [25] until the difference between the calculated and measured frequencies is minimized. A measure of the quality of the fit can be described in terms of a standard function of the form

$$\chi = \sum \frac{w_n (f_n - g_n)^2}{g_n^2} \tag{23}$$

where w_n is a weighting factor for the normalized difference between the calculated frequencies f_n and the measured frequencies g_n. A good value for the root-mean square (rms %) difference for the first 50 modes is generally accepted to be $\leq$ 0.4 %. The stability of this minimization process is of key importance to the accurate determination of the elastic constants using RUS. Aspects of this will be discussed further in the following chapter.

REFERENCES

[1] A. Migliori and J. L. Sarrao, *Resonant Ultrasound Spectroscopy* (J. Wiley and Sons, New York: 1997).

[2] A. Migliori, J. L. Sarrao, W. M. Visscher, T. M. Bell, L. Ming, Z. Fisk, and R. G. Leisure, Physica B **183**, 1 (1993).

[3] I. Ohno, J. Phys. Earth **24**, 355 (1976).

[4] R. G. Leisure and F. A. Willis, J. Phys. Condens. Matter **9**, 6001 (1997).

[5] K. Foster, R. G. Leisure and A. V. Skripov, J. Phys.: Condens. Matter **11**, 799 (1999).

[6] K. Foster, R. G. Leisure, J. E. Hightower and A. V. Skripov, accepted to J. Phys.: Condens. Matter, (July 2001).

[7] A. V. Skripov, S. V. Rychkova, M Yu Belyaev and A. P. Stepanov, J. Phys.: Condens. Matter **2**, 7195 (1990).

[8] K. Foster, R. G. Leisure and A. V. Skripov, accepted to Phys. Rev. B, (August 2001).

[9] R. G. Leisure, K. Foster, J. E. Hightower, A. Ode and A. V. Skripov, accepted to J. Alloys Compd., (May 2001).

[10] K. Foster, J. E. Hightower, R. G. Leisure and A. V. Skripov, Phil. Mag. B **80**, 1667 (2000).

[11] K. Foster, R. G. Leisure, J. E. Hightower and A. V. Skripov, submitted to Phys. Rev. B. (August 2001).

[12] K. Foster, R. G. Leisure and J. B. Shaklee, J. Y. Kim and K. F. Kelton, Phys. Rev. B **59** (17), 11 132 (1999).

[13] A. M. Viano, R. M. Stroud, P. C. Gibbons, A. McDowell, M. S. Conradi and K. F. Kelton, Phys. Rev. B **51**, 12 026 (1995).

[14] K. Foster, R. G. Leisure and J. B. Shaklee, J. Y. Kim and K. F. Kelton, Phys. Rev. B **61** (1), 241 (2000).

[15] K. Foster, S. L. Fairburn, R. G. Leisure, S. Kim, D. Balzar, G. Alers and H. Ledbetter, J. Acoust. Soc. Am. **105** (5), 2662 (1999).

[16] H. M. Ledbetter, *Materials at Low Temperatures*, ed. by R. P. Reed and A. F. Clark (Metals Park, Ohio: American Society for Metals), p.1.

[17] A. Migliori, W. M. Vissher, S. Wong, S. E. Brown, I. Tanaka, H. Kojami and P. B. Allen, Phys. Rev. Lett **64**, 2458 (1990).

[18] A. S. Nowick and B. S. Berry, *Anelastic Relaxation in Solids* (Academic Press, New York: 1972).

[19] F. I. Fedorov, *Theory of Elastic Waves in Crystals* (Plenum, New York: 1968).

[20] H. B. Huntington, *The Elastic Constants of Crystals* (Academic Press, New York: 1958).

[21] J. R. Pellam and J. K. Galt, J . Chem. Phys. **14**, 608 (1946).

[22] R. T. Beyer and S. V. Letcher, *Physical Ultrasonics* (Academic Press, New York: 1969).

[23] H. H. Demerest, J. Acoust. Soc. Am. **49**, 768 (1971).

[24] E. Schreiber, O. L. Anderson, N. Soga, N. Warren, C. Scholtz, Science **168**, 1579 (1970).

[25] F. A Willis, Ph.D. dissertation, Colorado State University, unpublished (1999).

[26] P. S. Spoor, Ph.D. dissertation, Pennsylvania State University, unpublished (1997).

[27] W. M. Visscher, A. Migliori, T. M. Bell and R. A. Reinert, J. Acoust. Soc. Am. **90** (4), 2154 (1991).

Chapter 2

Experimental Details: Resonant Ultrasound Spectroscopy

- **2.1 Introduction**
- **2.2 Sample Preparation**
- **2.3 Electronics**
- **2.4 Analysis of Resonant Lineshapes**
- **2.5 Low-temperature Systems**
- **References**

2.1 Introduction

The basic experimental and theoretical aspects of RUS were discussed in the preceding chapter. A significant fraction of the RUS experiments which are reported in this work has been made on small highly-attenuating samples. This immediately created extra difficulties, including low signal amplitudes, broad (low Q) resonant lineshapes which tend to overlap with nearby modes, and the more basic physical problems associated with preparing and working with small samples. A major problem encountered continually throughout the research involved the feed-through of ultrasonic vibrations across the air gap and / or through acoustic pathways about the RUS jig itself. Not surprisingly the feed-through across the air gap was significantly more pronounced for smaller samples. The background signals transmitted through the jig only became problematic at temperatures below $\approx$ 80 K, presumably due to the decrease in the

ultrasonic loss of the materials comprising the jig itself (aluminum and G10 composite polyester) as the temperature is lowered. The net result of the feed-through is to distort the resonant (Lorentzian) lineshapes making accurate determination of center frequency (f_0) and quality factor difficult. This only proved a problem for materials with high ultrasonic loss.

Most of the RUS experiments reported in this work have used temperature as an independent variable. The details of the design of the cryogenic systems used for the RUS measurements will be discussed. The following sections of chapter 2 will describe the procedures used at Colorado State to make high-quality temperature dependent RUS measurements.

2.2 Sample Preparation

The single most important requirement for making accurate modulus measurements with RUS is the high quality of the rectangular parallelepiped (RP) sample. If opposite faces are not parallel, adjacent sides are not perpendicular, corners and edges are of poor quality, or if surface imperfections exist, the resonant frequencies of the sample will be significantly affected. This leads to poor agreement between the measured and computed frequencies with root-mean-square (rms) values > 0.5 %. In such circumstances the derived values of the elastic moduli are generally considered to be unreliable [1].

Typically the starting point was a small button ingot of material. The ingot was cut with a low-speed diamond saw into a rough RP shape. The sample faces were then

polished by hand into an accurate RP. An optical flat and shim setup was developed [1] for this purpose, the basic geometry of which is shown in figure 2.1. The sample was placed in a small gap between four shims and one face was polished flat and parallel to the surface of the shims. The shims and sample were attached to the optical flat with mounting wax. It was critical to ensure that the shims were absolutely flush against the surface of the optical flat. The shims were then removed and replaced by a set of reduced thickness. The sample was rotated through 180° and positioned so that the polished side was now flush against the optical flat. The second side was then polished so that there were now two opposite smooth parallel sides. To polish a third side which should be perpendicular to the two polished sides, the sample was rotated through 90°. The key requirement here was that the two flat polished sides were held flush by two adjacent shims, *not* that the opposite side was necessarily flush with the optical flat. The fourth side was polished parallel to the third side by placing the third side flush to the optical flat *and* ensuring that the two parallel polished sides were flush with two adjacent shims. This procedure was repeated until all six sides were polished and an accurate RP produced.

Some attempt was made to quantify the tolerances required for successful RPs using a video microscope. However, in some senses the quality of the RUS fit itself was considered as good a measure as any. Certainly not all accurate RPs will produce a good fit due to inhomogeneities within the material (e.g. voids, cracks, texture, mixed-phases) but it is hard to imagine a set of circumstances which could contrive to produce a good RUS fit for a sample of poor geometry. Successful samples certainly contained no corner-angles which were more than a few tenths of a degree from 90°.

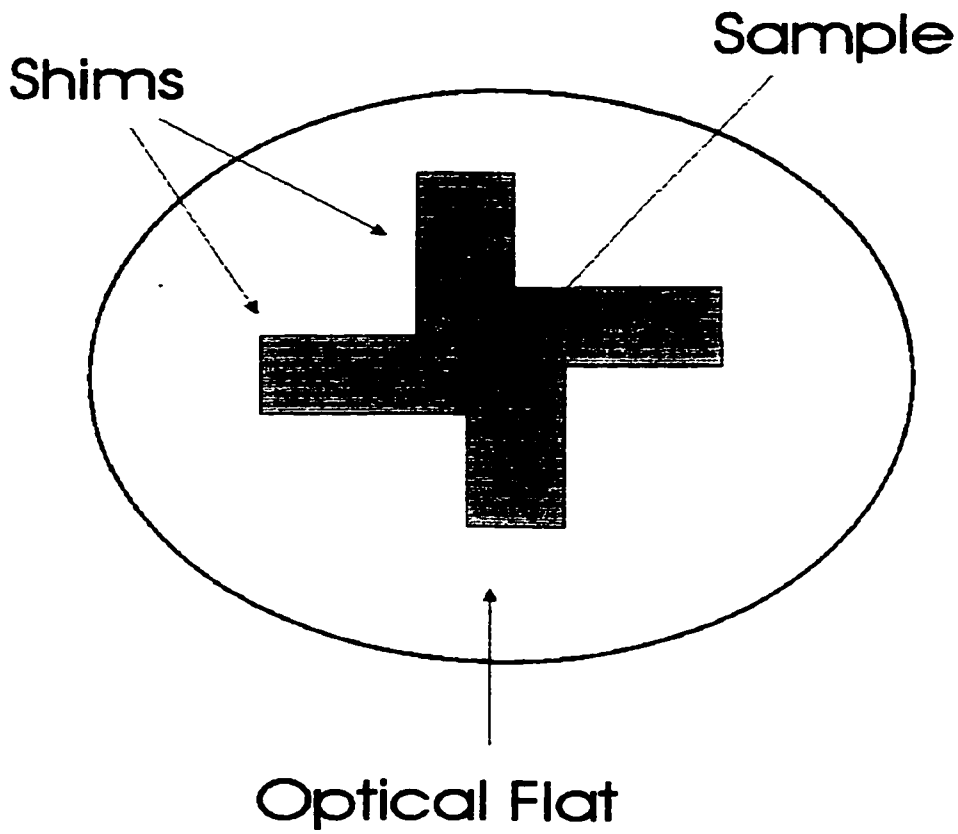

Figure 2.1: Top view of the experimental setup used to polish accurate rectangular parallelepipeds.

The success of the polishing procedure was limited by the quality of the shims themselves and by the polishing scheme chosen for a particular material. Six shim sets of graduated thicknesses between 1.2 - 2.2 mm were precision made to tolerances of 1 / 10 000th of an inch. Samples were hand-polished using various diamond pastes, polishing solutions, polishing clothes and fine-grit sand papers. Particular polishing schemes were chosen on consideration of the physical properties of the subject material; specifically the material hardness.

Occasionally samples which had been carefully polished and which 'appeared' as though they should produce good results were found to produce poor RUS fits and / or anomalously high ultrasonic loss. On further polishing voids or cracks previously within the volume of the sample would be revealed on the surface. In some cases more polishing would remove these flaws and produce a good quality sample. This demonstrates nicely one of the more practical uses of RUS; that of non-destructive testing. This proved a significant problem with the metal-hydride samples studied. Metals and intermetallics have a propensity to crack when loaded with hydrogen due to the lattice expansion which usually occurs as a result of the hydrogenation [2]. As may be expected it was found that this effect was greater for samples loaded to higher hydrogen concentrations. The high background value for the ultrasonic loss measured in these kinds of samples was presumably due to the frictional losses associated with the motion of the cracks.

2.3 Electronics and Computer Algorithms

A commercial spectrometer (Dynamic Resonance Systems, Inc.) was used

throughout the RUS experiments reported in this thesis. The system incorporates state of the art low-noise detection electronics and a digitally synthesized heterodyne swept-sine signal analyzer. The amplitude of the radio frequency (RF) output could be adjusted in eight discrete steps between 0 and 20 V. Care was taken to avoid non-linear effects by using the lowest amplitude drive voltage required to clearly observe the resonances of interest. In all the cryogenic systems a twisted pair was used in the drive circuit, while a small coaxial cable was used in the detection circuit. A 1/1 transformer consisting of roughly 50 turns of copper wire on a ferrite core (balun) was also used in the drive circuit to separate the ground of the probe from that of the spectrometer. This helped reduce (to workable levels) background voltages arising from grounding loops which were a problem in the low-temperature systems. The spectrometer also allowed the user to insert a time delay between data points, allowing a 'ringing' sample to settle. This was a necessary feature for measurements on high Q materials.

The computer algorithms used to calculate the resonant frequencies and to perform the minimization to derive the elastic moduli were provided with the spectrometer and were developed by others [3][4][5]. Typically 40 - 50 resonances were used to compute the elastic constants. The free parameters of the fit were the elastic constants and the sample dimensions. The dimensions of the sample were only allowed to vary after a good fit had already been achieved. The dimensions were adjusted in such a way that the volume (and hence density) of the sample was maintained. The dimensions could be measured in lab to an accuracy of $\approx$ 2 microns and were not permitted to adjust by more than this during the fitting procedure.

The fitting-program requires initial 'guesses' for the elastic constants to compute an initial set of frequencies. Usually a literature survey would be performed to look for related work on the material of interest. If no such work could be found, weighted averages of the elastic constants of the constituent elements were sometimes used. Usually a series of different input 'guesses' would be tested to check the consistency of the minimization process. The root-mean-square difference between the computed and measured frequencies was taken as the single most important indicator of the quality of the fit. The % error in the fitting parameters were also calculated and for a reliable fit no elastic constant was expected to have an error of more than ± 2 %.

2.4 Analysis of Resonant Lineshapes

As was mentioned briefly in chapter 1 an RUS sample acts as a driven damped oscillator. When the frequency of oscillation of the driving transducer f approaches a natural frequency of the sample f_0 then the mode of frequency f_0 will be strongly excited. Assuming that there are no other modes in the near vicinity of f_0, all other modes will only be weakly excited but may still make small contributions to the measured signal at f_0. As discussed in section 2.1 there are also contributions to the signal from acoustic coupling across the air gap or through the mechanical RUS jig. A measured signal ultimately consists of the resonant response plus a background term. To accurately determine the center frequencies and Qs the background effects need to be considered. This section will describe how the RUS resonances were fit to a Lorentzian lineshape and a background signal.

Consider the response of a damped simple 1-d harmonic oscillator to an applied sinusoidal driving force of angular frequency ω. The applied force can be written as $Fe^{-i(\omega t+\theta)}$ where θ is a phase shift between the driving and detected signals. In the case of RUS this phase shift is a result of the detection electronics, cabling and transducers etc. The equation of motion of a 1-d damped driven oscillator of mass m is written simply as

$$Fe^{-i(\omega t+\theta)} - kx - 2b\frac{dx}{dt} = m\frac{d^2x}{dt^2} \tag{1}$$

where k represents the 'spring constant' and the parameter b characterizes the viscous damping. The steady state solution of **Eq.** (1) is of the simple form,

$$x(t) = x_0 e^{-i\omega t}. \tag{2}$$

There is, of course, also a transient term which results in an exponential decay of the initial amplitude x_0 with some characteristic time constant τ. The resonant frequency of the oscillator is given by $\omega_0 = \sqrt{k/m}$ and it can be shown that $Q = \omega_0 m/2b$. By substituting **Eq.** (2) into **Eq.** (1) and using these relations an expression for the amplitude is obtained,

$$x_0 = \left[\frac{F}{m}\right]\frac{e^{-i\theta}}{(\omega_0^2 - \omega^2) - i(\omega_0\omega/Q)}. \tag{3}$$

Eq. (3) is a Lorentzian-response function written in complex notation. This can separated

into real and imaginary terms,

$$x_0 = \left[\frac{F}{m}\right]\left(\frac{1}{(\omega_0^2-\omega^2)^2+(\omega\omega_0/Q)^2}\right)^* \left[(\omega_0^2-\omega^2)\cos\theta+(\omega\omega_0/Q)\sin\theta\right]+i\left[(\omega\omega_0/Q)\cos\theta-(\omega_0^2-\omega^2)\sin\theta\right] \quad (4)$$

which is of the form,

$$x_0 = u - iv \quad (5)$$

where the minus sign is arbitrary. Combining **Eqs.** (2) and (5) an expression for the displacement is obtained

$$x(t) = [u\cos(\omega t) - v\sin(\omega t)] - i[v\cos(\omega t) + u\sin(\omega t)] \quad (6)$$

It is clear from **Eq.** (6) that the real part of the signal has components vibrating at $\sin(\omega t)$ and $\cos(\omega t)$. These are sometimes referred to as the quadrature and in-phase components respectively. The spectrometer used for the RUS experiments at Colorado State outputs both the u and v of **Eq.** (6). By defining

$$a = \left[\frac{F}{m}\right]\left[\frac{Q}{f_0^2}\right]\frac{1}{(2\pi)^2} \quad (7)$$

and comparing **Eqs.** (4) and (6) we obtain for the detected RUS signals, u_{rus} and v_{rus}

$$u_{rus} = a\left[\frac{f_0^2}{Q}\right]\frac{[(f_0^2-f^2)\cos\theta+(f_0 f/Q)\sin\theta]}{(f_0^2-f^2)^2+(f_0 f/Q)^2} \quad (8)$$

$$v_{rus} = a\left[\frac{f_0^2}{Q}\right]\frac{[(f_0^2 - f^2)\sin\theta - (f_0 f / Q)\cos\theta]}{(f_0^2 - f^2)^2 + (f_0 f / Q)^2}. \quad (9)$$

Lorentzian lineshape plus a background:

Following the work by Mehl [6], who analyzed background effects on standing-wave resonance measurements, the background signal was expanded as a function of frequency [7]. Only a constant and a term linear in frequency were used. The background was also considered to have in-phase and quadrature components. Thus, the background was written as

$$background = b_1 + ib_2 + (c_1 + ic_2)\left(\frac{f - f_0}{f_0}\right). \quad (10)$$

Combining Eq.(10) with Eqs. (8) and (9), expressions for the in-phase and quadrature components of the resonant response with a background are obtained,

$$u_{rus+back} = a\left[\frac{f_0^2}{Q}\right]\frac{[(f_0^2 - f^2)\cos\theta + (f_0 f / Q)\sin\theta]}{(f_0^2 - f^2)^2 + (f_0 f / Q)^2} + b_1 + \frac{c_1(f - f_0)}{f_0} \quad (11)$$

$$v_{rus+back} = a\left[\frac{f_0^2}{Q}\right]\frac{[(f_0^2 - f^2)\sin\theta - (f_0 f / Q)\cos\theta]}{(f_0^2 - f^2)^2 + (f_0 f / Q)^2} + b_2 + \frac{c_2(f - f_0)}{f_0} \quad (12)$$

The experimentally recorded resonant lineshapes were fit to Eqs. (11) and (12). The fit

parameters are the center frequency f_0, quality factor Q, phase angle θ, peak amplitude a and the 4 parameters describing the nature of the background. Figures 2.2 (a) and (b) show fits (at 250 K and 140 K respectively) to **Eqs.** (11) and (12) of the in-phase and quadrature components of a resonance of the C15 Laves phase compound, $TaV_2D_{0.17}$. The in-phase and quadrature components were fit simultaneously to the *same* values of f_0, Q, a and θ. The Q of this particular mode changed by an order of magnitude over this temperature range: note that the frequency range in figure 2.2 (a) is roughly 30 times that of figure 2.2 (b). The fits were performed using Microcal Origin software which uses a standard (Levenburg-Marquardt) non-linear least-squares algorithm. This fitting procedure, though rather time consuming but has vastly improved the quality of the attenuation data.

2.5 Low-temperature Systems

This work reports RUS measurements made over a temperature range of 300 mK to 350 K. A ^{3}He cryostat (Janis Corporation) was used to make a small number of measurements down to 300 mK. A more recently acquired 'static bath' ^{4}He cryostat (Oxford Instruments) was used to make RUS measurements down to 2.8 K. Finally, a simple gas flow (^{4}He, N_2) cryostat incorporating a home-built probe was used for measurements at higher temperatures (> 120 K). The operation of the ^{3}He system was certainly the most complex but has been described elsewhere [4] and will not be discussed further here.

Figure 2.3 shows a simple schematic of the Oxford ^{4}He static bath cryostat. The

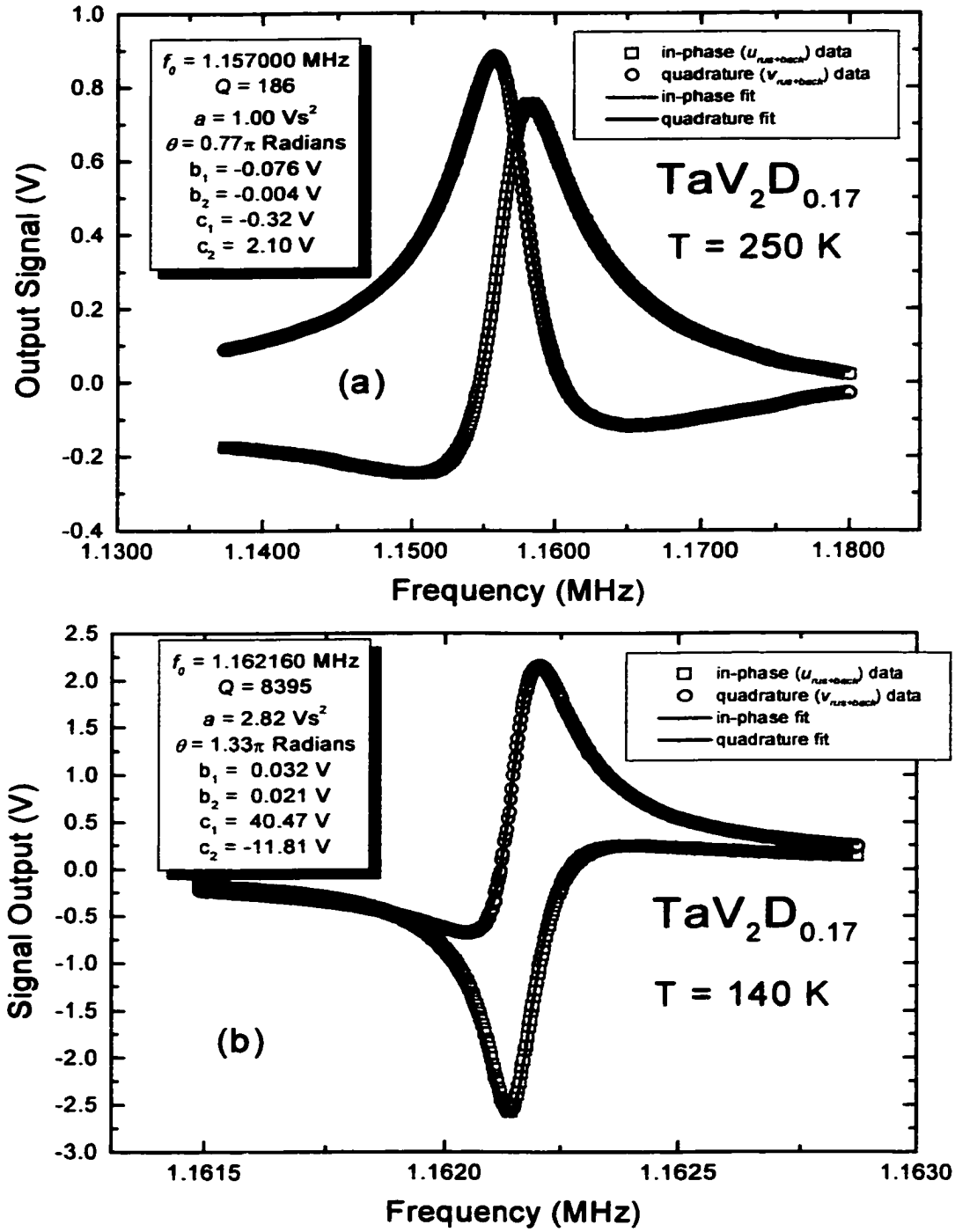

Figure 2.2: A resonant eigenmode of $TaV_2D_{0.17}$ at (a) 250 K and (b) 140 K. The solid lines represent theoretical fits to **Eqs.** (11) and (12). The parameters derived from the fits are listed in the figures.

ability to reduce the gas pressure about the sample was a key design consideration as it was expected that this would greatly reduce the transmission of sound waves across the transducer air gap. As was mentioned in section 2.4, feed-through of this type can significantly distort the resonant lineshapes. Figures 2.4 (a) and (b) show sections of room-temperature RUS spectra of a C15 Laves-phase alloy $ZrCr_2$ and an intermetallic alloy $TiCr_{1.8}$ respectively. The spectra are shown before and after reducing the gas-pressure to $\approx$ 4 mbar about the sample. It is clearly seen that the background signal has been drastically reduced by the decrease in gas pressure, while the frequency of the resonant modes remain unaffected. Combined with the fitting procedures described in section 2.4 this design modification has greatly improved the quality of the ultrasonic loss measurements. (It should be mentioned that by considering the mean-free path-length (λ), a pressure of 4 mbar of ^{4}He gas is sufficient to provide good thermal contact between the walls of the sample chamber and the sample itself.)

Figure 2.5 is a photograph of the RUS jig used with this system. A calibrated Si-diode temperature sensor (Lakeshore Cryotronics, Inc.) was thermally anchored $\approx$ 1 cm from the sample. This sensor is accurate to $\pm$ 20 mK for temperatures < 10 K and to $\pm$ 50 mK for temperatures 10 K < T < 475 K. A rhodium-iron sensor supplied with the system was used to measure the temperature of the gas-exchange area. The accuracy of this sensor is $\pm$ 0.01 K from 1 - 400 K. A standard 4-lead configuration was used with both sensors. The system also included a 20 ohm heater in the heat-exchange space. A commercial temperature controller (Conductus Inc.) was used to control and monitor the temperature sensors and to power the heater.

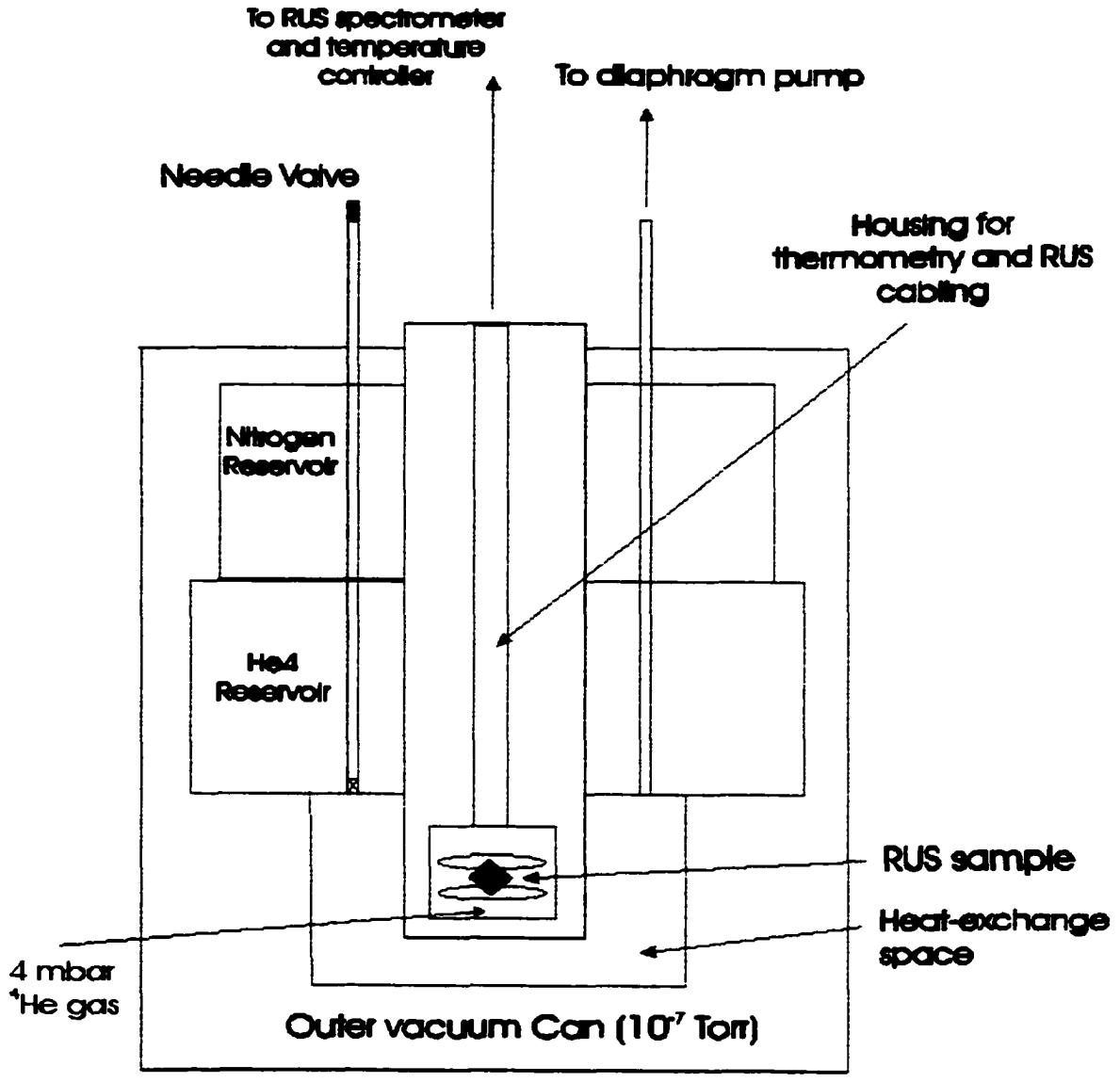

Figure 2.3: A simple schematic of the Oxford Instruments 'Optistat Bath' static variable temperature cryostat. (Diagram not to scale.)

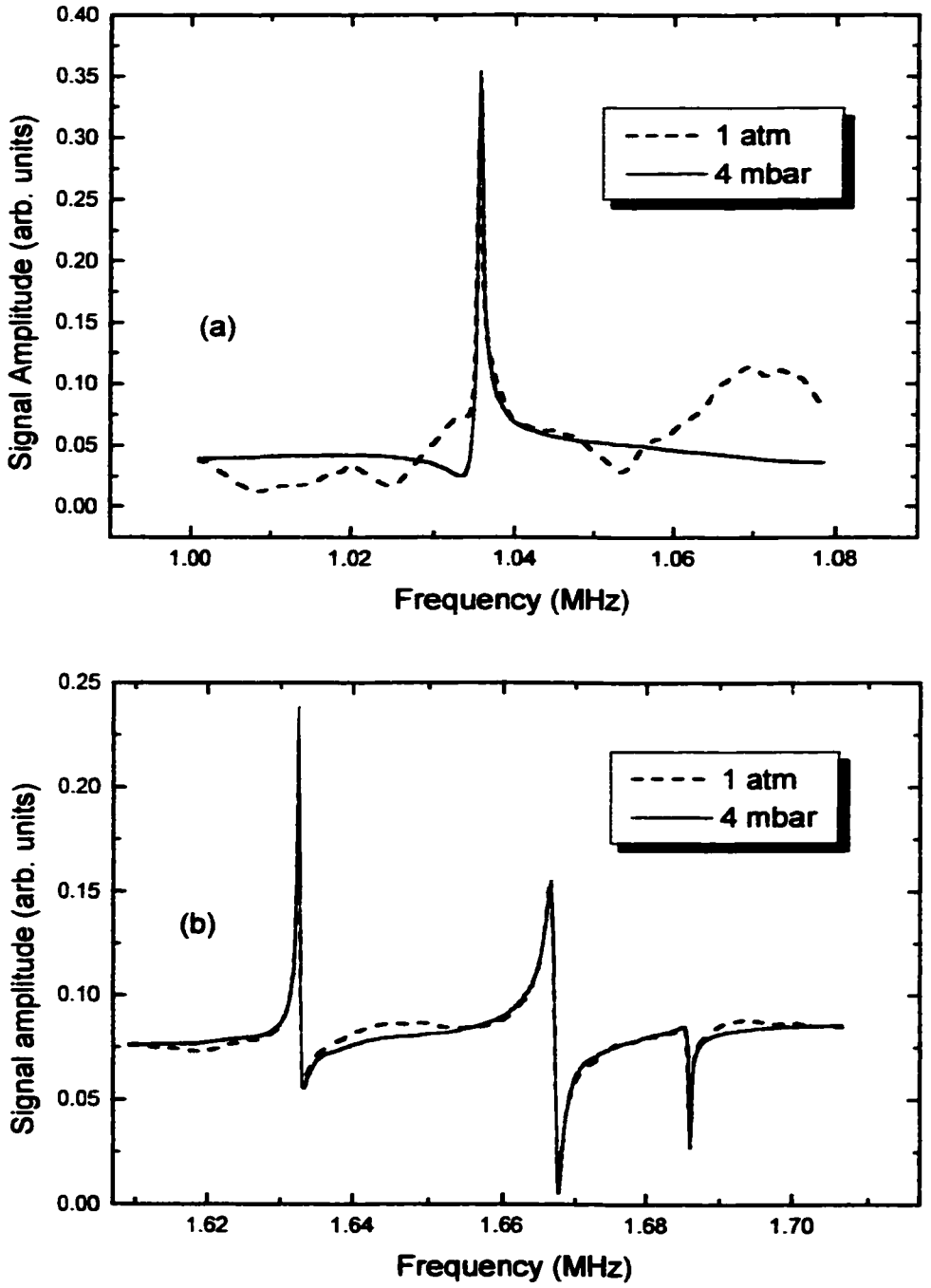

Figure 2.4: Pressure dependence of a section of the RUS spectrum for (a) C15 Laves-phase intermetallic alloy $ZrCr_2$ (b) Intermetallic alloy $TiCr_{1.8}$.

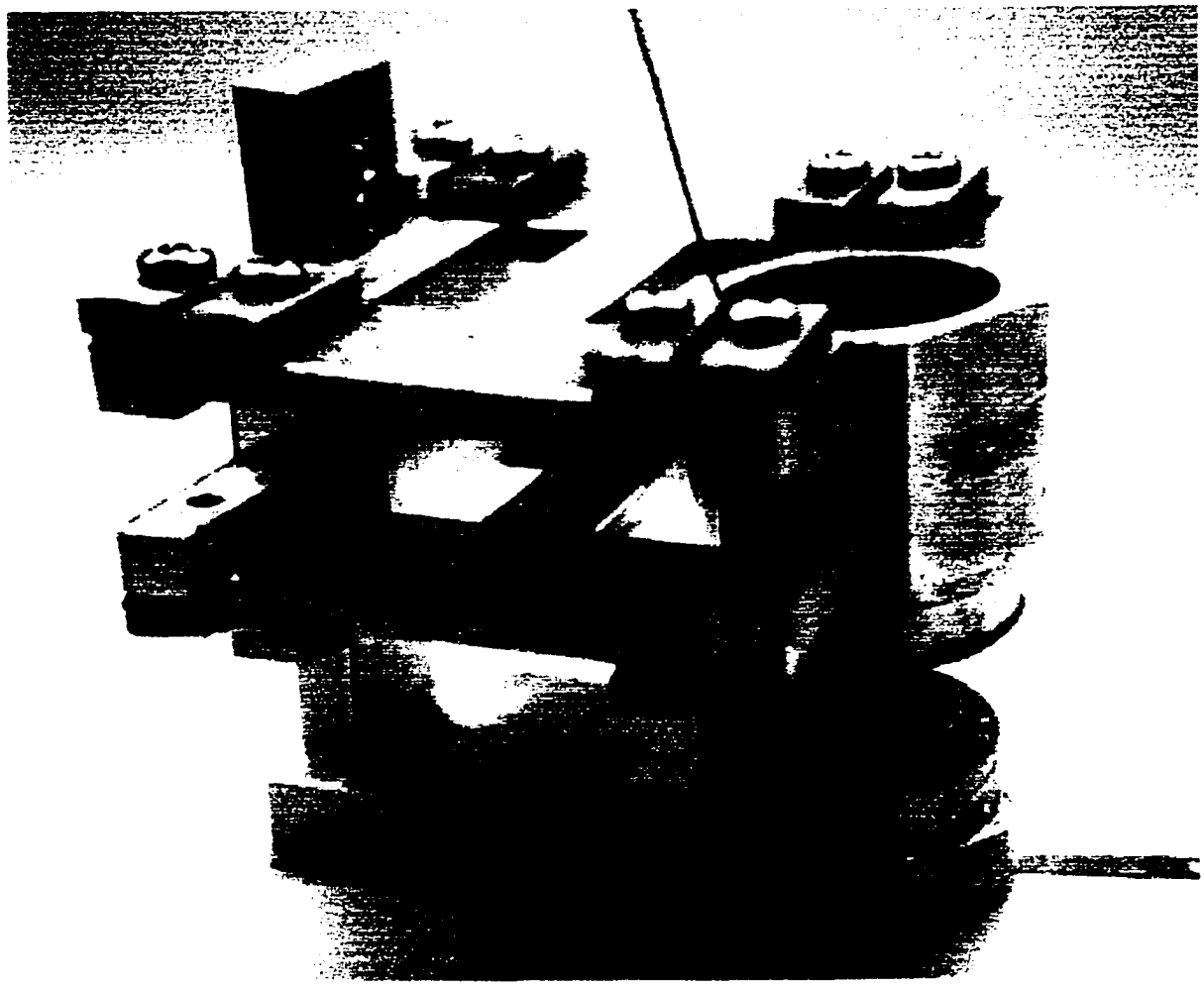

Figure 2.5: Photograph of the RUS jig used in the Oxford ^{4}He cryostat. (Courtesy of J. E. Hightower.) The sample can just be seen mounted corner to corner between two transducer-drumhead arrangements.

To perform a ^{4}He experiment down to 3 K the following steps were taken. The outer vacuum can (OVC) was initially pumped down to 10^{-7} Torr. The system was found to out-gas readily between each low-temperature run requiring the system to be pumped down prior to each experiment. Before filling the system with liquid cryogens both the sample space and the cryogen reservoir were flushed thoroughly with ^{4}He gas and the pressure of the sample space reduced to $\approx$ 4 mbar. To minimize the consumption of liquid ^{4}He, the system was pre-cooled to ~77 K with liquid nitrogen and left to equilibrate for roughly 12 hours. Liquid ^{4}He was then transferred into the helium reservoir. This would take on the order of 1 hour. The rate of transfer was controlled to achieve a balance between time and cost: the rate of transfer must be slow enough so that the evaporated ^{4}He gas has time to effectively cool the reservoir walls. Typical transfer rates were on the order of 10 liters / hour, with a total of 15 liters required to fill the reservoir.

During the ^{4}He transfer the needle valve was opened one half a turn to reduce the risk of any remaining air /water vapor freezing and blocking the valve. Controlling the temperature of the sample space heat exchanger (and hence the sample) between 3 K and 300 K was achieved by balancing the flow of liquid ^{4}He with the heater output power. The control software of the Conductus temperature controller utilizes a three term function to minimize the difference between the control sensor temperature and the desired setpoint temperature. The standard coefficients of the control function are the so-called PID (Proportional band (P), Integral action time (I), Differential action time (D)) coefficients. Correct selection of the PID coefficients for a cryogenic system usually involves an 'educated' trial and error process. As an added complication the coefficients

usually depend strongly on temperature. Below temperatures of ≈ 120 K where the system was found to respond rapidly to changes in heater power, control to within ± 0.1 K was readily achieved. At these temperatures the 'autotune' feature of the Conductus temperature controller was able to automatically determine the required PID coefficients. Control of the system became more difficult at higher temperatures where the system was slower to respond to the heater output. Above 150 K the system was usually left to drift slowly towards room temperature as it became unreasonably time consuming to control. The rate of warming was controlled easily with the heater and needle valve settings. In a typical experiment the system would warm at roughly 0.25 K / minute.

To achieve control down to 2.8 K the system was cooled at roughly 2 K / min to 20 K. This required a ^{4}He flow rate of ≈ 0.4 cm^3 / s (roughly ½ turn on needle valve) with a pressure of ≈ 300 mbar in the heat exchange area. The flow rate was extremely sensitive to the needle valve setting. As the system cooled below 30 K a constant output power would be provided to the heater to stabilize the temperature of the system between 20 K and 30 K. At this point the needle valve was then opened further in tiny fractions of a turn to cool the system steadily to 2.8 K. A small diaphragm pump was used to pump on the ^{4}He in the heat-exchange volume. By using larger pumps lower temperatures would be achievable.

The transducers used with the ^{4}He system depended on the temperature range of the particular experiment. As can be seen from figure 2.5 the transducers are mounted in the center of gold-plated kapton-foil disks, in a drumhead arrangement. The drive and detected signals are transmitted through thin foil fly-leads which are also observable in the

photo. The thickness of the kapton foil and gold plating was 20 μm and 10 μm respectively. It was found that foils of such low thickness reduced the background signal due to the feed-through of sound about the jig itself. Above 120 K PZT (lead-zirconate-titanate) compressional-mode transducers were used as they are relatively cheap and have very low-Q (< 50) resonances [1]. However below 120 K measurements using PZTs were of poor quality with low signal amplitudes and additional background signals appearing. Lithium niobate compressional-mode transducers were used successfully down to 2.8 K in the ^{4}He cryostat (and to 0.3 K in the ^{3}He system) though at temperatures > 120 K signal amplitudes were smaller than those obtained with the PZTs. The lithium niobate transducers introduced an added complication as they exhibit a bending mode resonance at a few hundred kHz, the frequency scale of interest for the RUS experiments. Following the work of Migliori *et. al* [1] cylindrical diamonds of the same diameter (1.5 mm) were epoxied to the back of the transducers. The high sound velocity of diamond raises the resonant frequency of the transducer-diamond system to values well above the frequency range of interest.

Figure 2.6 shows a photo of a home-built RUS probe used with a simple gas-flow cryostat. This probe was used extensively for RUS measurements down to 20 K prior to the acquisition of the Oxford ^{4}He cryostat at Colorado State. The probe uses an RUS jig of identical design to that shown in figure 2.5. A standard silicon diode thermometer was used in a typical 4 lead arrangement. A 50 ohm heater and the Conductus temperature controller were used for temperature control. Measurements were made with the sample in a flow of cryogen, at atmospheric pressure. The system had a low thermal mass

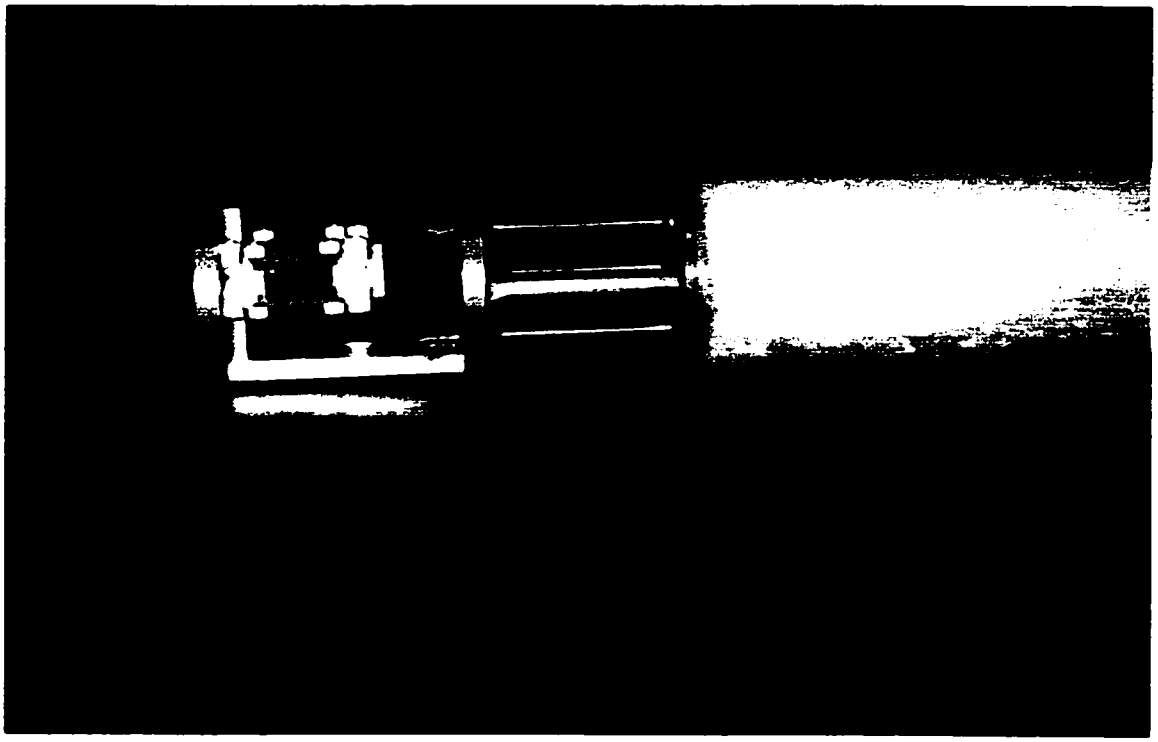

Figure 2.6: Photo of the home-built RUS probe for use with the gas-flow cryostat. A RP sample of Olin corporation Cu can be seen mounted corner to corner in the drumhead-transducer assembly.

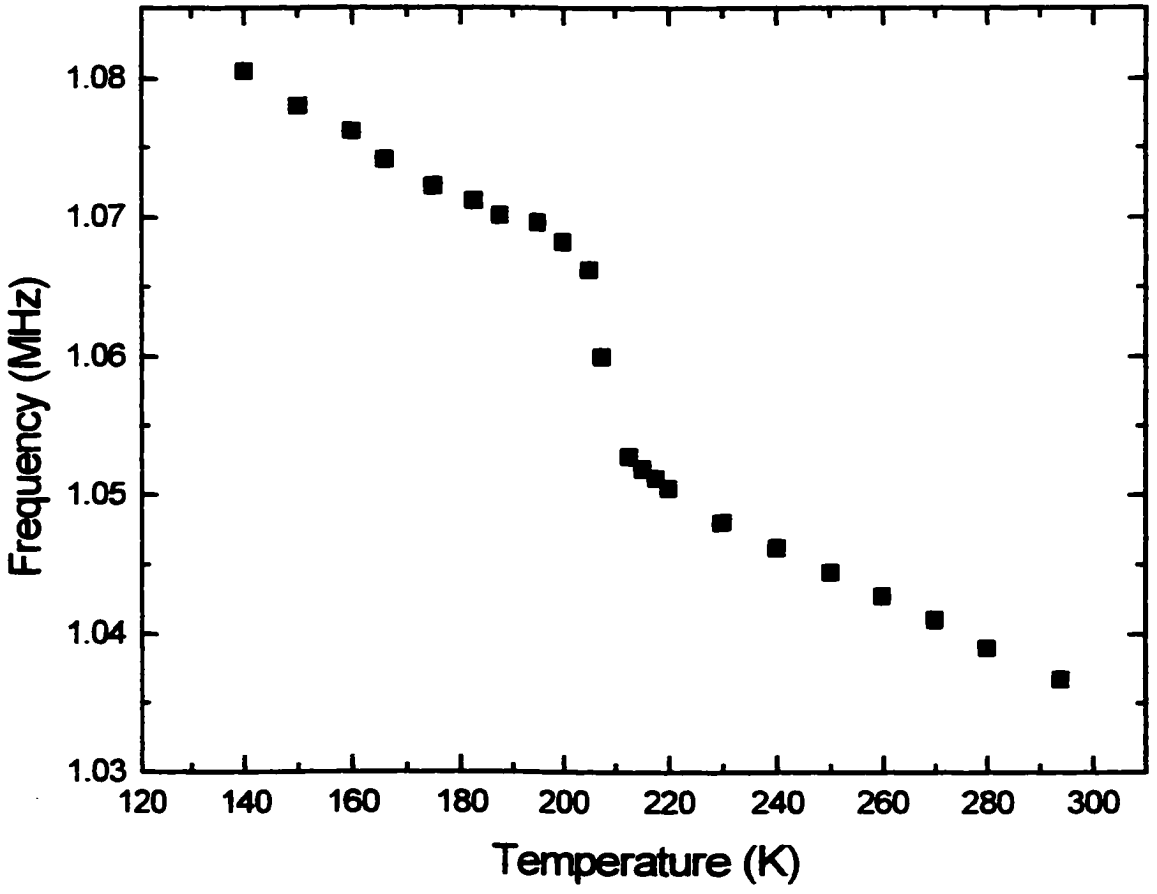

Figure 2.7: The frequency of a resonant eigen-mode versus temperature for Olin Corporation Cu - 5 % Zn polycrystalline brass alloy. The 'step' observed in the data was found to be erroneous, presumably an artifact of the experimental design.

allowing for rapid and accurate temperature control. The temperature stability at a set-point was within ± 0.01 K. The probe was built entirely from scratch due to an anomalous behavior exhibited by the former probe. An extraneous bump in the frequency data was observed systematically in the older version of the probe at roughly 200 K, for all samples tested. An example of this effect is shown in figure 2.7. The magnitude of the effect was greatest for the lower frequency modes and exhibited some hysteretic behavior. The problem proved extremely persistent and the origin of the anomaly was ultimately never understood. However, the effect is thankfully absent in all data taken on the re-built probe.

REFERENCES

[1] A. Migliori A and J. L. Sarrao, *Resonant Ultrasound Spectroscopy* (J. Wiley and Sons, New York: 1997).

[2] H. Piesl, in *Hydrogen in Metals I*, ed. by G. Alefeld and J. Völkl, J. Topics Appl. Phys., Vol **28** (Springer, Berlin Heidelberg, 1978), Ch. 3.

[3] A. Migliori, J. L. Sarrao, W. M. Visscher, T. M. Bell, L. Ming, Z. Fisk and R. G. Leisure, Physica B **182**, 1 (1993).

[4] F. A. Willis, Ph.D. dissertation, Colorado State University, unpublished (1999).

[5] W. M. Visscher, A. Migliori, T. M. Bell and R. A. Reinert, J. Acoust. Soc. Am. **90** (4), 2154 (1991).

[6] J. B. Mehl, J. Acoust. Soc. Am. **64** (5), 1523 (1978).

[7] R. G. Leisure, private correspondence, July 2000.

Chapter 3

A Resonant Ultrasound Spectroscopy Study of the C15 Laves-phase Compound TaV_2H_x

- **3.1 Introduction: Metal-hydrogen Systems**
- **3.2 Ultrasonic Attenuation and Dispersion in the C15 Laves-phase Compound TaV_2H_x**
- **3.3 Ultrasonic Evidence for Strong Isotope Effects on the Local Motion of H(D) in $TaV_2H(D)_x$**
- **3.4 Strong Hydrogen-related Electronic Effects on the Elastic Shear Modulus of $TaV_2H(D)_x$**
- **3.5 Concluding Remarks**
- **References**

3.1 Introduction: Metal-hydrogen Systems

The cubic C15 Laves-phase compound $TaV_2H(D)_x$ absorbs hydrogen to a maximum concentration of $x = 1.7$. The ultrasonic attenuation and elastic constants of $TaV_2H(D)_x$ have been measured over a temperature range of 0.3 - 345 K. Sections 3.2 and 3.3 will discuss the attenuation results and derive parameters of the hydrogen motion, including activation energies, attempt frequencies and relaxation strengths. Section 3.3 will highlight strong isotope effects observed for the H(D) motion in $TaV_2D_{0.17}$ and $TaV_2H_{0.18}$ at low temperatures. Section 3.4 will report findings of anomalous elastic behavior displayed by the $TaV_2H(D)_x$ system. The elastic constant results are interpreted in terms of a hydrogen-related electronic band-structure effect. Before describing the

details of these experiments, the following sub-sections shall provide a general background into the technological and theoretical importance of metal-hydrogen systems, including a discussion of the specific information that can be derived from ultrasonic measurements.

3.1.1 Metal-hydrogen Systems: Technological Importance

It has long been known that many pure metals absorb H to some degree. Many transition metals readily absorb considerable amounts of H and indeed palladium hydride has perhaps been one of the most extensively studied metal-hydride (MH) systems. More recently there has been an increasing interest in the hydrogen storage properties of more novel materials, including a wide variety of intermetallic alloys and carbon based nano-structured compounds.

Surely the first application of a MH system was the Davy lamp, developed after Sir Humphrey Davy's observation in 1817 that palladium and platinum wire [1] undergo a strong exothermic reaction under exposure to hydrogen gas. This device was used commonly by coal-miners. Possibly the most important application of MH materials to date has been in the field of rechargeable Ni / MH batteries [2][3], which are used extensively today to power laptop computers, cellular phones and other low-weight electronic devices. Ni-based batteries with a MH negative electrode are slowly replacing those which formally used Cd as the negative electrode. The switch was motivated by the high toxicity and relatively high cost of Cd. The Ni / MH batteries were first discovered in the 1970s [4] but were not introduced into the market place until much more recently.

The MHs currently used for battery applications are intermetallic alloys of AB_5 composition. It was discovered in the late 1960s that $LaNi_5$ can readily and reversibly absorb six H atoms per formula unit [4]. Further improvements to the properties of $LaNi_5$, particularly in terms of lifetime and cycling characteristics, have been made by substituting small amounts of Co for Ni. The AB_2 Laves-phases alloys demonstrate better weight-capacity characteristics than the AB_5 compounds and it is expected that these alloys will form the next generation of Ni / MH batteries [2].

Within the last year a number of automobile manufacturers have begun marketing the so-called 'hybrid' motor vehicles. These vehicles use a small gasoline combustion engine in conjunction with an electric motor. These vehicles use rechargeable Ni / MH batteries to power the electric motor. The batteries are conveniently charged when the gasoline engine is being used to power the vehicle. Furthermore, with growing international restrictions on the toxic and greenhouse-gas emissions from motor vehicles, the notion of a hydrogen economy is generating an ever increasing interest. In particular, fuel cells, which use hydrogen as a fuel (some fuel cells use hydrocarbons as the fuel, e.g. natural gas, regular gasoline, methanol) have been developed to generate electric power, particularly for a new generation of electric-motor vehicles. Very basically, a fuel cell consists of two 'electrodes' sandwiched around an electrolyte. The hydrogen gas, encouraged by a catalyst, is dissociated into electrons and protons at the anode. The protons travel through the electrolyte to the cathode. The electrons take an alternate route, creating a current which can be utilized. The electrons are reunited with the protons in an oxygen atmosphere to produce water. Presently almost every major

automobile manufacturer is working towards developing fuel-cell technology. It is expected that the first fuel-cell vehicles will be available on the general market within three years. It seems certain that by whatever means hydrogen is used as a fuel, metal-hydrides must surely play a key role in the technology, particularly for hydrogen storage purposes.

As a final example, a number of rare-earth metal hydrides have been found to undergo a metal to insulator transition with the addition of small amounts of hydrogen [5][6]. The phase change is reversible so there is some potential for developing devices from these materials with rapidly switchable electrical and optical properties. This example illustrates how the addition of hydrogen can have very strong effects on the electronic properties of the host material.

3.1.2 Metal-hydrogen Systems: Theoretical Importance

There is also, of course, fascinating science involved with metal-hydrogen systems, spanning a large breadth of topics, including, thermodynamics and phase-stability of MHs, diffusion of H about the host lattice, quantum-mechanical aspects of diffusion, electronic and magnetic properties, lattice defects / strains, vacancy formation, vibrational modes of metal-hydrides etc. Excellent and detailed reviews of the experimental and theoretical aspects of these subjects can be found elsewhere [7][8][9][10][11]. In this thesis ultrasonic experiments investigating the motion of hydrogen about the host lattice are reported. Therefore, the following section will therefore discuss the information that can be gained about the diffusion of hydrogen within a material using ultrasonic techniques.

3.1.3 The anelastic solid and relaxation attenuation

In an elastic solid there is a simple linear relationship between the applied stress and resultant strain, given by Hooke's law, $\sigma = C\varepsilon$. It would be expected from this relation that a solid reacts instantaneously to an applied stress, so that the stress and strain are always in phase. In any real-world system there is usually some time-delay between the application of the stress and the full response of the media. For example, this time-delay may occur as a result of the re-orientation or hopping of a light interstitial or defect under the influence of the strain. It has been shown [12] that Hooke's law can be modified for these effects by considering a simple exponential relaxation with a characteristic single relaxation time (τ). This results in an equation of the form

$$\sigma + \tau \frac{d\sigma}{dt} = c_R \varepsilon + \tau c_U \frac{d\varepsilon}{dt} \tag{1}$$

where c_U and c_R are referred to as the unrelaxed and relaxed elastic constants respectively. By considering an applied stress, given by

$$\sigma(t,\omega) = \sigma(\omega)e^{i\omega t} \tag{2}$$

with an expected resultant strain

$$\varepsilon(t,\omega) = \varepsilon(\omega)e^{i\omega t} \tag{3}$$

it is shown [13] easily that **Eq.** (1) can be written in terms of a frequency-dependent complex elastic constant, $c^*(\omega)$, given by

$$c^*(\omega) = c_U + \frac{c_R - c_U}{1+\omega^2\tau^2} + i(c_U - c_R)\frac{\omega\tau}{1+\omega^2\tau^2}. \quad (4)$$

From examination of **Eq.** (4) it can be seen that where $\omega >> \tau^{-1}$, $c^*(\omega)$ reduces to the unrelaxed modulus c_U: in this situation the material does not have time to respond to the applied driving term. Conversely, when $\omega << \tau^{-1}$, $c^*(\omega)$ reduces to the relaxed elastic constant c_R and the system can fully respond to the modulations in the strain.

The properties of the generic 1-d damped driven oscillator (of mass *m*) can be considered conveniently by introducing the notion of a complex force constant, $k^* = k_1 + ik_2$. In systems where $k_2 = 0$ the power absorbed per cycle is zero and the Q of the system is infinite. If $k_2/k_1 << 1$ the system will exhibit a resonant response centered about the natural resonant frequency of the system given by $\omega_0 = \sqrt{k_1/m}$. The point of interest here is that the loss in such a system is given by the ratio of the imaginary to the real component of the force constant, $Q^{-1} = k_2/k_1$. In an identical way, by considering **Eq.** (4), the ultrasonic loss $1/Q$ due to relaxation for an anelastic solid is given by,

$$\frac{1}{Q} = \frac{\Delta c}{c}\frac{\omega\tau_R}{1+\omega^2\tau_R^2} \quad (5)$$

where $(\Delta c/c)$ is usually referred to as the relaxation strength, $\omega/2\pi$ is the ultrasonic

frequency and τ_R is the characteristic relaxation time. **Eq.** (5) is often referred to as a Debye-time relaxation function. The quantity Δc is the difference between the unrelaxed and relaxed elastic moduli; $\Delta c = c_U - c_R$. The second term of **Eq.** (4) is much smaller than that of the first and has been neglected. Furthermore, the distinction between c_U and c_R has been ignored in the denominator of **Eq.** (5). For most systems the difference between c_U and c_R is just a few percent.

An explicit expression for the relaxation strength can be calculated for simple systems [14] such as a two-level system (TLS). A wide range of physical phenomena has been described by such a model. An interstitial atom such as hydrogen, which may occupy either of two nearby interstitial sites can be described as a TLS. A simple diagram of a TLS is shown in figure 3.1. The system consists of two adjacent potential wells of energies $+A$ and $-A$ of positional eigenstates ϕ_1 and ϕ_2. The state of a H atom in the TLS will simply be some linear combination of these two eigenstates. The value of A denotes the asymmetry of the sites. The tunneling matrix element Δ_0 arises due to the overlap of the wavefunction of the two wells and represents the interaction between the two states. It can be shown that the energies of the system $E_{1,2} = \pm E$ are given by,

$$E = (\Delta_0^2 + A^2)^{1/2}. \tag{6}$$

For a TLS the form of the relaxation strength is derived [14] from basic thermodynamic arguments. Starting with the fundamental definition of the elastic constant as the second

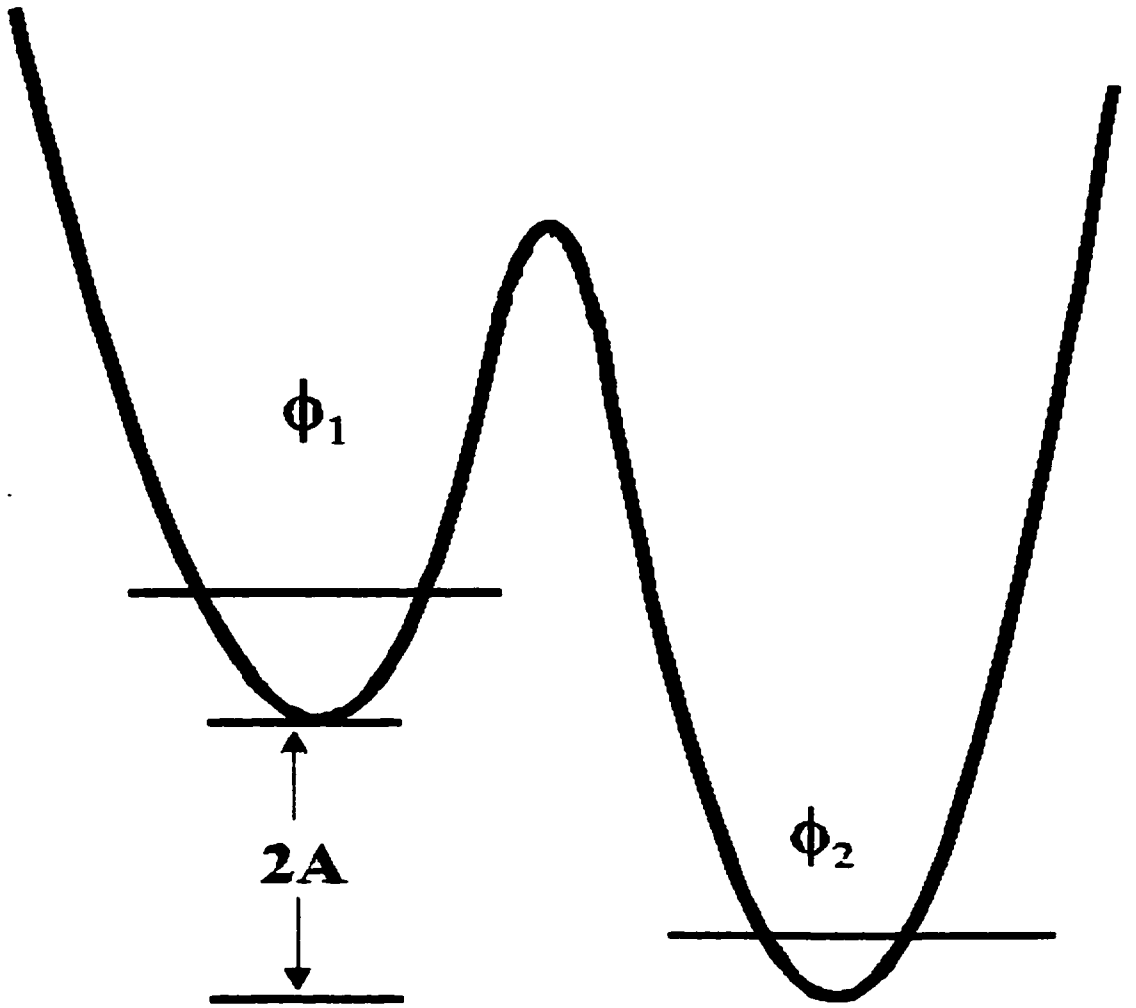

Fig 3.1: Simple schematic of the two-level system often used to model H motion in metal-hydrides. The figure illustrates a double-well potential which may correspond to two adjacent interstitial sites. The energy difference of the two levels is denoted by *2A*, the asymmetry energy. The energy levels of the two wells are denoted by the solid lines. In the absence of a tunneling matrix element, Δ_0, the energy splitting, ΔE, is simply equal to the asymmetry energy. The energy levels will be shifted for non-zero matrix elements.

derivative of the free energy,

$$c(\varepsilon) = \frac{\partial^2 F(\varepsilon)}{\partial \varepsilon^2} \tag{7}$$

and taking $F(\varepsilon) = F_0(\varepsilon) + F_{TLS}(\varepsilon)$, where $F_0(\varepsilon)$ represents all the strain-dependent interactions *except* those from the two-level system, $F_{TLS}(\varepsilon)$. $F_{TLS}(\varepsilon)$ can be calculated from basic statistical mechanics

$$F_{TLS}(\varepsilon) = -nk_B T \ln[Z(\varepsilon)] \tag{8}$$

where n is the density of the two-level system, k_B is Boltmann's constant, T is the temperature and $Z(\varepsilon)$ is the partition function of the TLS. $Z(\varepsilon)$ is obtained by summing over the two levels of the system

$$Z(\varepsilon) = \exp\left[\frac{-E}{k_B T}\right] + \exp\left[\frac{E}{k_B T}\right] = 2\cosh\left[\frac{E}{k_B T}\right]. \tag{9}$$

Combining **Eqs.** (6), (7), (8) and (9) and setting $D = \partial A / \partial \varepsilon$ we obtain

$$c = c_0 - \frac{nD^2\Delta_0^2}{E^3}\tanh\left[\frac{E}{k_B T}\right] - \frac{nD^2}{k_B T}\left[\frac{A}{E}\right]^2 \operatorname{sech}^2\left[\frac{E}{k_B T}\right]. \tag{10}$$

It has been shown [15] that the second term of **Eq.** (10) is related to resonant transitions between the two levels. Generally the frequency of the ultrasound is much

lower than that of the resonant process so this usually only makes small contributions to the attenuation. However, this term can have more significant effects on the real part of the elastic constant. This effect is clearly quantum-mechanical in origin and does not occur when the tunneling matrix element is zero. The third term in **Eq.** (10) is related to the relaxation of the two-level system in response to the applied strain. **Eq.** (10) has been calculated for the equilibrium, or zero frequency regime. For very high frequencies ($\omega\tau >> 1$) the system does not have time to adjust to the strain and there can be no effect due to relaxation. The difference between these two limits gives the Δc of **Eq.** (5). Therefore, for a TLS we obtain the following explicit expression for the relaxation strength

$$\frac{\Delta c}{c} = \frac{nD^2}{k_B T c}\left[\frac{A}{E}\right]^2 \operatorname{sech}^2\left[\frac{E}{k_B T}\right]. \qquad (11)$$

This formalism applies to both the classical and quantum regimes and may be used when the tunneling matrix element Δ_0 is negligible. For this situation $A / E \rightarrow 1$ and the equation simplifies.

In the case of a metal-hydrogen system, n is taken to be the volume concentration of H atoms participating in the relaxation. For D to be nonzero, the two nearby potential wells must respond differently to the applied strain. In other words they are inequivalent. Except at very low temperatures it is usually the case that $k_B T >> \Delta E$ and the $\operatorname{sech}^2 [\Delta E / k_B T]$ term of **Eq.** (11) approaches unity. This assumption will be made in the analysis of

the experimental data throughout chapters 3 and 4.

From **Eq.** (4) it is observed that the theory of relaxation also predicts a frequency-dependent shift in the real part of the elastic modulus, related to the transition from the relaxed to the unrelaxed elastic moduli as the temperature decreases. The change in the elastic moduli δc due to relaxation [13] is given by

$$\delta c = \Delta c \frac{(\omega\tau_R)^2}{1+\omega^2\tau_R^2}, \tag{12}$$

which subsequently results in a shift δf in the measured mechanical resonant frequencies, f

$$\delta f = \left(\frac{\Delta c}{c}\right)\left(\frac{f}{2}\right)\frac{(\omega\tau_R)^2}{1+\omega^2\tau_R^2}. \tag{13}$$

The present work interprets the experimental results within this framework; that of hydrogen atoms siting on one of two adjacent interstitial sites which can be described as a two-level system. The temperature dependence of the ultrasonic loss and mechanical frequencies can be used to derive information about the temperature dependence of the relaxation time, τ_R, of the hydrogen. This is done by fitting the ultrasonic loss and frequency data to **Eqs.** (5) and (13) respectively. The form of the relaxation time required can provide information into the nature of the interstitial sites on which the H is sitting and on the rates at which the hydrogen is hopping. In some cases this can then be used to derive a microscopic picture of the hydrogen diffusion. A typical expression for the

relaxation time that is applicable to a variety of physical phenomena is a single exponential term (Arrhenius expression) of the form

$$\tau_R = \tau_{R_0} \exp(E_a / k_B T) \tag{14}$$

where E_a is an activation energy and $\tau_{R_0}^{-1}$ is an attempt frequency. In most cases more complicated expressions for τ_R are required. For a metal-hydrogen system the activation energy may be the energy required for a H atom to classically hop over a barrier between adjacent wells. Alternatively, this may be the energy required to excite an atom into a higher energy state from which the atom can then (quantum mechanically) tunnel through to the next well.

3.2 Ultrasonic Attenuation and Dispersion Due to Hydrogen Motion in the C15 Laves-phase Compound TaV_2H_x

3.2.1 Introduction

3.2.1.1 Hydrogen Diffusion in Intermetallics

As mentioned in section 3.1.1 metal-hydrogen materials are important for a number of technological reasons, primarily related to energy storage and battery applications. A high diffusion coefficient of hydrogen in the metal is important for most applications. In addition, the diffusion of a light interstitial such as hydrogen poses

challenging theoretical problems [7][16]. While early work focused on elemental metals [17], more recently there has been an increasing interest in intermetallic compounds [18] due to their ability to absorb considerable quantities of hydrogen. The local environment of hydrogen in intermetallic compounds is often more complex than in elemental metals due to the large number and variety of interstitial sites in these compounds. This can lead to a series of pathways for the hydrogen motion with the result that the microscopic motion responsible for diffusion is more complicated than in simpler materials. An improved understanding of hydrogen diffusion mechanisms in intermetallic compounds is desirable for both practical and fundamental reasons.

3.2.1.2 Hydrogen Diffusion in the Laves-phase Intermetallics

One extensive class of intermetallic compounds is the Laves-phase. There is a large number (>1000) of binary Laves-phase materials [19] with the AB_2 stoichiometry, forming with three symmetries; the C15 cubic, the C14 hexagonal and the C36 structure. All three crystal symmetries have a large number of tetrahedral interstitial sites. Many of these compounds are known to absorb considerable amounts of hydrogen and have been studied extensively with a variety of experimental techniques [20][21][22][23][24][25][26][27][28][29][30]. The present discussion will focus on the C15 structure. The atomic structure of the C15 Laves-phase is shown in figure 3.2. There are three different types of tetrahedrally coordinated interstitial site (g, e and b), differentiated by the species of the four surrounding atoms. Each g site is surrounded by 2 A and 2 B atoms; each e site by 1 A and 3 B atoms; and each b site by 4 B atoms. It is

usually the case that hydrogen occupies the g site in C15 materials [31][32]. The g sites are arranged in networks of hexagons with the g-g distance within hexagons being less than the g-g distance between hexagons. Each g site is associated with one and only one hexagon. The arrangement of the g type interstitial sites in a C15 Laves-phase material is presented in figure 3.3.

A fascinating picture is emerging of hydrogen motion in the C15 materials. There appears to be a fast localized motion corresponding to hopping within a hexagon of g sites, and a slower motion corresponding to jumps between hexagons [33][34][35][36][37][38]. Quasielastic neutron scattering results have shown that for the C15 compounds, the frequency separation between the two mechanisms appears to be the greatest for TaV_2H_x [39]. The lower frequency motion is slower, and the higher frequency motion is faster than in other Laves hydrides. TaV_2 absorbs relatively large amounts of hydrogen, forming stable homogeneous solid solutions of TaV_2H_x ($x \leq 1.7$) [40]. It has been shown that for all H concentrations the single-phase C15 host-lattice structure is maintained down to 4 K. Neutron diffraction results have indicated that hydrogen occupies only the g type (Ta_2V_2) interstitial sites [41][42]. Both nuclear magnetic resonance (NMR) and quasielastic neutron scattering measurements indicate two frequency scales of hydrogen motion in this material [35][39]. On the frequency scale of the NMR measurements (10^7-10^9 Hz) the spin-lattice relaxation rate data for the hydrogen, $(T_1^{-1})_H$, show two overlapping peaks as a function of temperature. The high-temperature peak was fitted to a single Arrhenius expression and associated with longer-range hexagon to hexagon hopping. The lower temperature peak exhibited non-Arrhenius

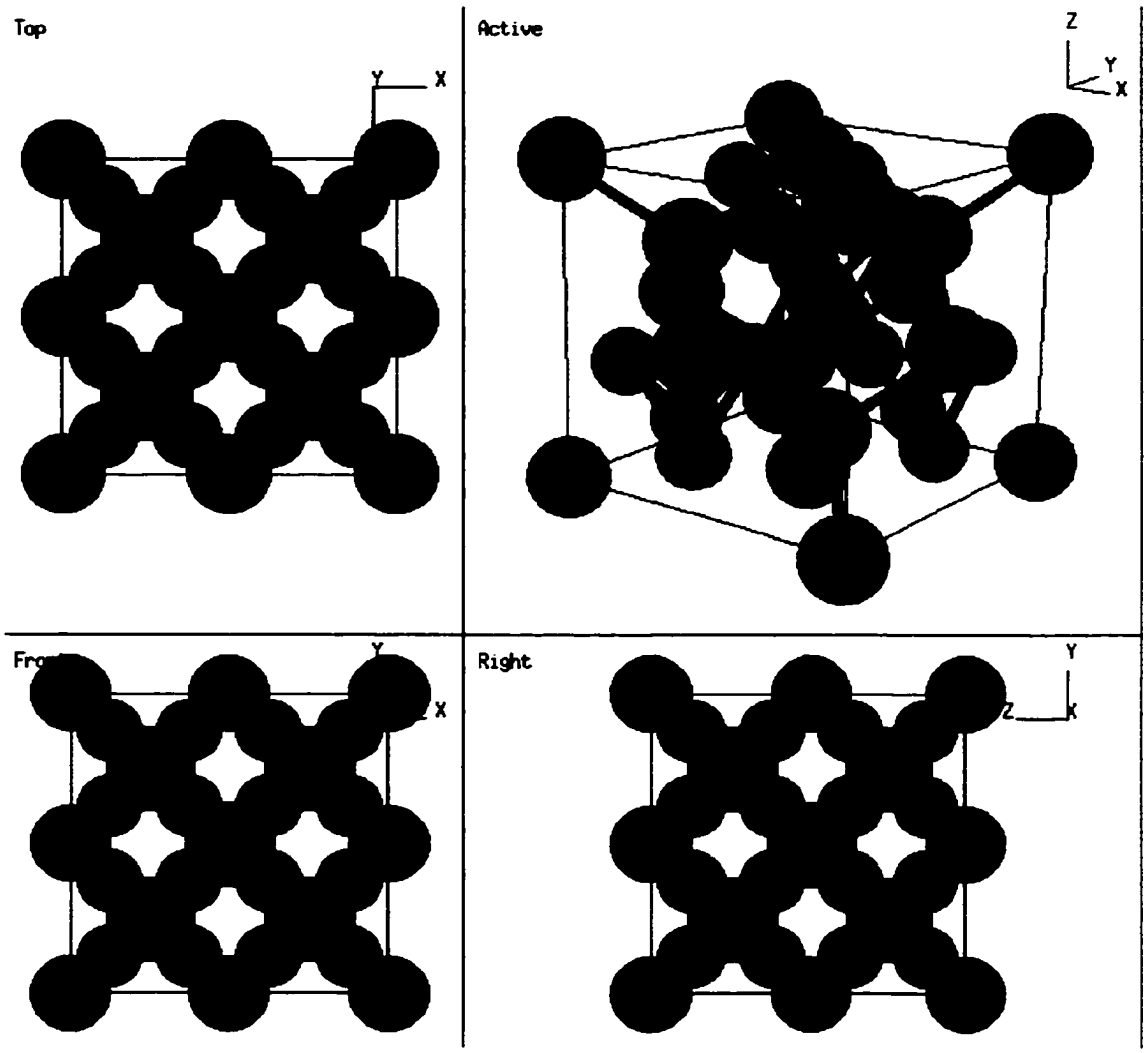

Figure 3.2: The fcc C15 binary AB_2 Laves-phase structure. The green circles represent the 'A' atom, and the red circles represent the 'B' atom. (Pictures taken from a crystal-structures web-site at URL http://cst-www.nrl.navy.mil/lattice/mainpage.html.)

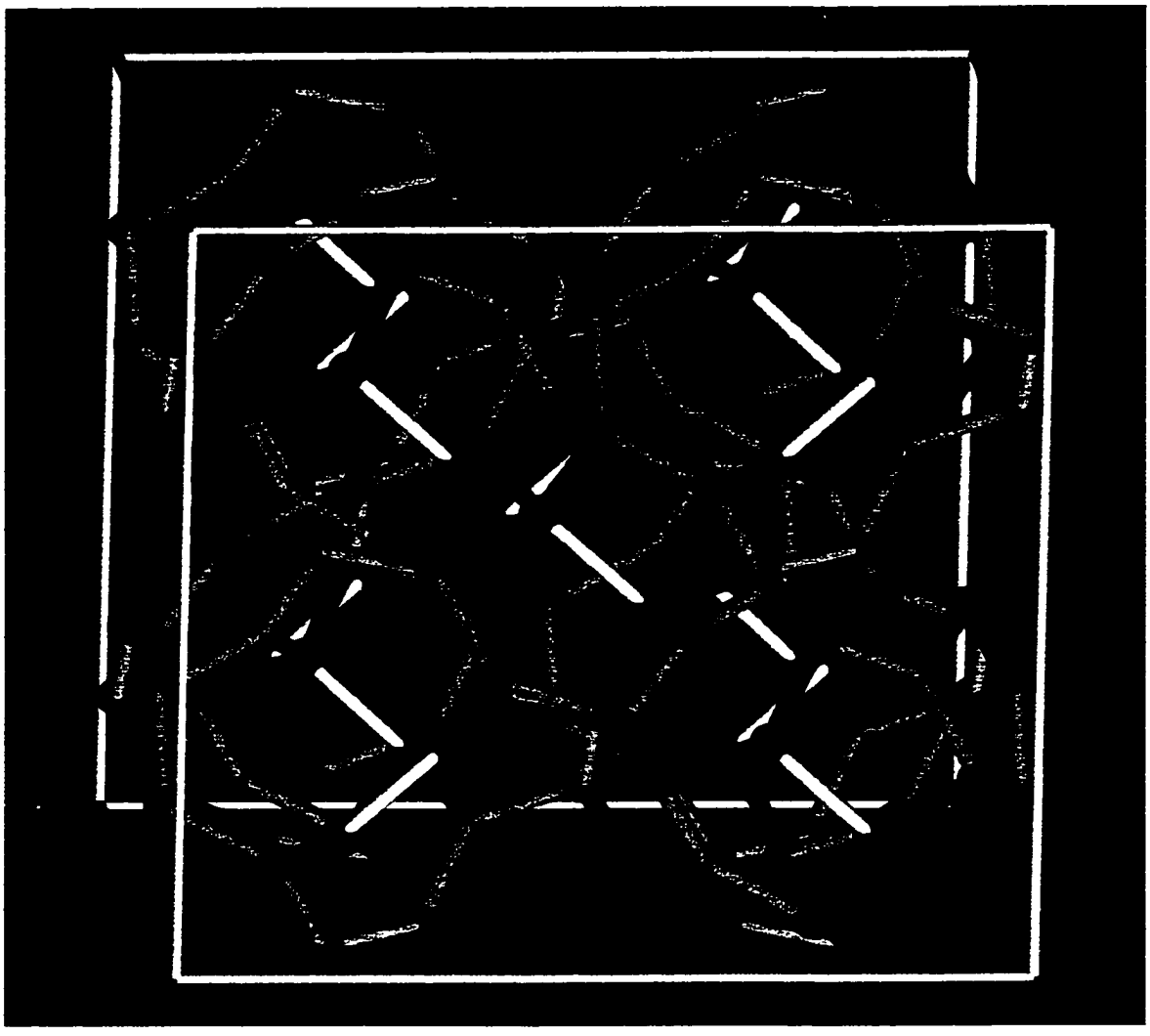

Figure 3.3: The geometry of the g-type and e-type interstitial sites within the AB_2 C15 Laves-phase structure. The g and e sites form a series of interlinked hexagons and pentagons surrounding the 'A' atom. The g-sites are represented by red spheres and the e sites by green spheres. (Picture courtesy of G. Majer, Max Planck Institute for Metal Physics, Stuttgart, Germany.)

behavior. This faster motion was attributed to a localized hydrogen hopping within hexagons formed by the g type interstitial sites and was not frozen out on the frequency scale of the NMR experiment down to 30 K. The local motion demonstrated several unusual features including strong isotope and hydrogen concentration effects.

There is much that is not understood about the hydrogen dynamics in these materials. Thus, it seemed desirable to apply other experimental techniques to this problem, such as ultrasound. Mechanical spectroscopy complements NMR and neutron measurements by exploring a different frequency (and hence temperature) regime. The hopping of hydrogen between nearby interstitial sites has been studied in many systems by means of mechanical spectroscopy (i.e. internal friction, ultrasonic attenuation, etc.). The requirements on the local site symmetry in order for anelastic relaxation to occur are described by the selection rules for anelasticity [12]. Although mechanical spectroscopy has been used to study hydrogen trapped near defects in crystals [43][44], as well as hydrogen in amorphous metals [45][46] and quasicrystals [47], the present discussion will focus on hydrogen in solid solution in crystalline metals. For the latter situation two cases can be distinguished. In the Snoek effect, the symmetry of the local sites is such that nearby sites respond differently to an applied stress. The tetrahedral (T) sites in elemental bcc metals are such sites. However, while these sites give rise to a Snoek effect for heavier interstitials such as C, the effect is not [48] observed for H. Apparently this is because the strain field associated with H is cubic in bcc metals despite the tetragonal symmetry of the interstitial sites. In the Zener effect the site symmetry is such that anelastic relaxation is not expected for an isolated hydrogen; however hydrogen-hydrogen

interactions can lower the site symmetry and lead to anelastic relaxation. This is the situation for the octahedral (O) site in elemental fcc metals [49][50][51] and the T site in elemental hexagonal metals [52][53]. Depending as it does on H-H interactions, the magnitude of the Zener effect [54][55] depends on the hydrogen concentration as $x^2(1-x^2)$ if the occupancy of the sites is not far from random. A simple linear dependence on x is expected for the Snoek effect. In contrast to the large body of work on H relaxation in crystalline elemental metals, there has been relatively little work on crystalline intermetallic compounds [56][57][58]. As mentioned above, hydrogen occupies only the g sites in TaV_2H_x. The symmetry of these g sites is lower than that of the cubic C15 lattice and thus the selection rules permit a non-zero relaxation strength involving jumps of isolated hydrogen atoms between neighboring g sites.

The purpose of this study was to examine the applicability of mechanical spectroscopy to investigate hydrogen motion in an intermetallic compound from attenuation and dispersion results.

3.2.2 Experimental Details

The Laves-phase materials used for the RUS experiments were fabricated at the Institute of Metals Physics, Urals Branch of the Academy of Sciences, Ekaterinburg, Russia. Polycrystalline ingots of TaV_2 were prepared by arc melting appropriate mixtures of the high-purity constituent elements in an argon atmosphere followed by various annealing procedures [37]. The TaV_2 material was then loaded to varying concentrations of H to form TaV_2H_x as has been described elsewhere [37]. It should be highlighted that

x-ray diffraction studies have shown that at room temperature all samples were single-phase solid solutions of hydrogen in TaV_2 with the expected cubic C15-type host-metal structure. For the studied range of hydrogen concentrations, TaV_2H_x samples do not show any phase transitions down to low temperatures.

Resonant Ultrasound Spectroscopy (RUS) was used to measure the ultrasonic attenuation and elastic constants in the TaV_2H_x system for a series of H concentrations (0.00, 0.06, 0.10, 0.18, 0.34 and 0.53). Accurate RP samples were prepared as described in section 2.2. Sample edge dimensions and masses were on the order of 1 - 2 mm and 20 - 50 mg respectively. The ultrasonic attenuation was found in the usual way by measuring the quality factor Q of a number of lower frequency modes.

Measurements of resonant frequency and attenuation were made over a temperature range of 15 - 345 K. The experiments below room temperature were made using the Oxford ^{4}He 'static flow' cryostat described in section 2.5. Measurements were made with samples in a static low-vacuum atmosphere of ^{4}He gas ($\approx$ 4 mbar). Experiments above room temperature were made in air at atmospheric pressure using a commercial oven and temperature controller. The temperature resolution of the experiments was roughly $\pm$ 0.1 K.

3.2.3 Results and Discussion

Figure 3.4 shows ultrasonic loss results for a single mode of TaV_2H_x for each H concentration studied from 15 - 345 K. Each mode presented in figure 3.4 was within the frequency range of 0.8 - 1.2 MHz. For all $x > 0$ a clear attenuation peak was observed

centered at approximately 220 - 250 K. Significantly, the attenuation in the hydrogen free material exhibits an almost temperature independent background with no prominent loss peak. It is immediately clear that the magnitude of the effect increases with increasing H concentration.

The observed attenuation peaks are interpreted as a Debye-type relaxation involving H hopping between adjacent interstitial sites. The ultrasonic loss $1/Q$ due to relaxation is given by **Eq.** (5). Assuming that the hydrogen environment can be modeled as a TLS, the form of the relaxation strength is given by **Eq.** (11). Using the NMR results as a guide an attempt was first made to fit the data to the simple Arrhenius expression for τ_R given by **Eq.** (14). It is assumed that the relaxation time τ_R is approximately the mean dwell time of hydrogen at an interstitial site. Figure 3.5 shows attenuation data for $TaV_2H_{0.34}$ at frequencies of 0.675, 0.823 and 1.198 MHz over a temperature range of 100 - 345 K. Figure 3.6 shows similar data for the $TaV_2H_{0.53}$ compound at frequencies of 0.643, 0.871 and 1.639 MHz. It can be seen that for these two compositions the fits of the experimental data to **Eqs.** (5), (11) and (14) are excellent. Importantly, the attenuation data for all modes of each H composition are fit to the same values of attempt frequencies and activation energies. These values indicate that the attenuation peaks are due to the same mechanism responsible for the high temperature peaks in the NMR experiments [35], which were interpreted as hexagon to hexagon hopping. The peaks in the NMR experiments were observed at significantly higher temperatures as those experiments were conducted at much higher frequencies (19.3 - 90 MHz) than the

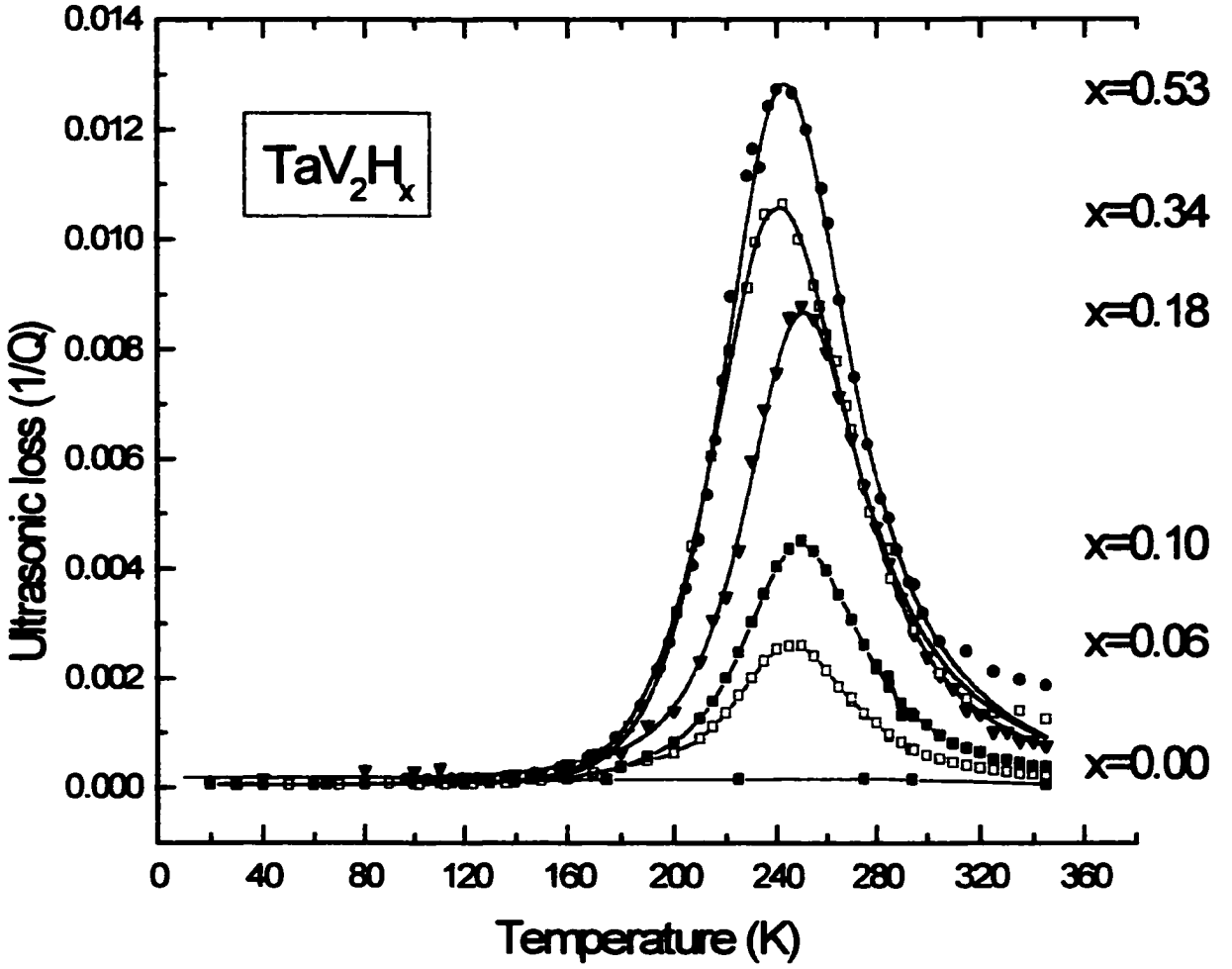

Figure 3.4: Temperature dependence of the ultrasonic loss in TaV_2H_x. Results are shown for all concentrations studied $x = 0.00$, 0.06, 0.10, 0.18, 0.34 and 0.53. The solid lines represent theoretical fits to the data using the parameters given in tables 3.1 and 3.2. Mode frequencies range from 0.8 - 1.2 MHz.

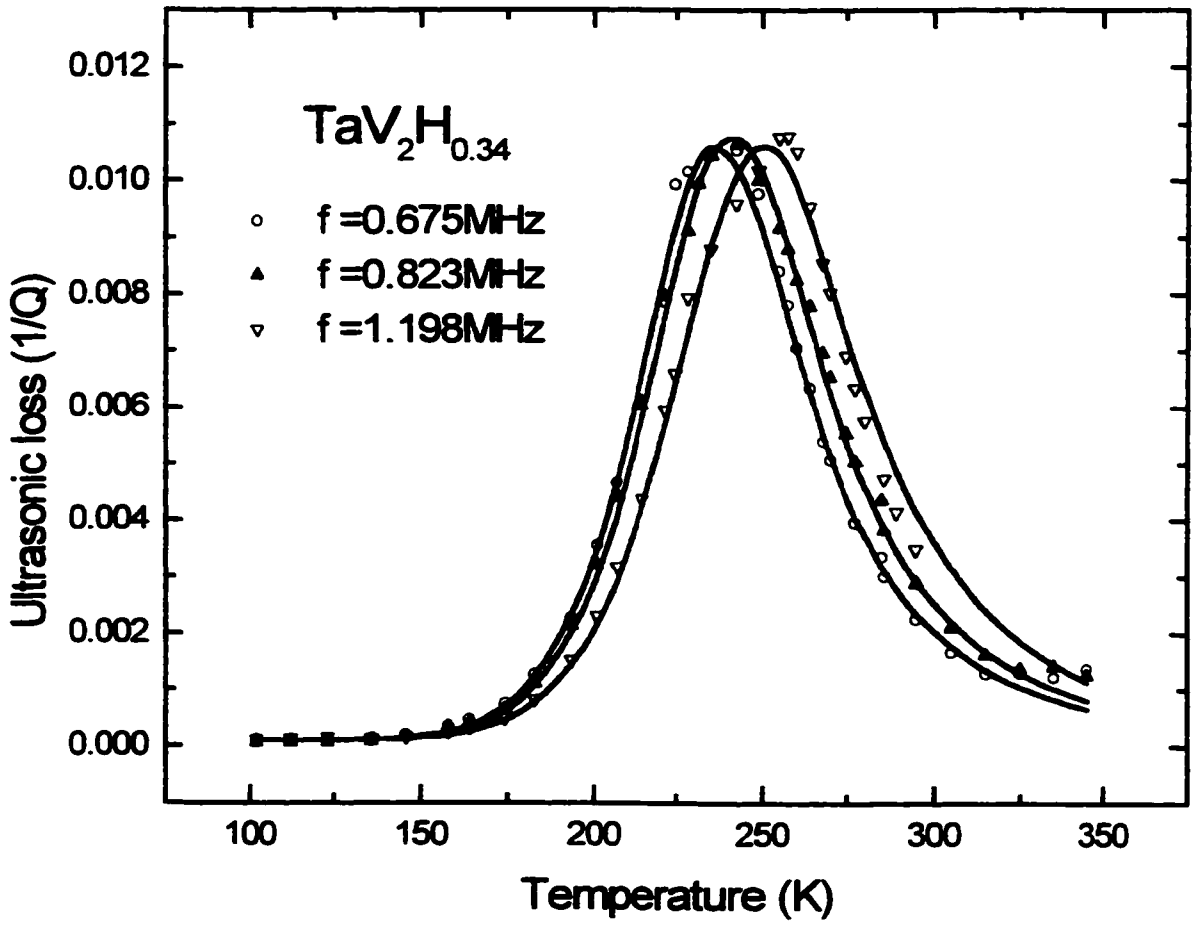

Figure 3.5: Temperature dependence of the ultrasonic loss in $TaV_2H_{0.34}$. The solid lines represent theoretical fits to the data using Eqs. (5), (11) and (14) with parameters given in table 3.1.

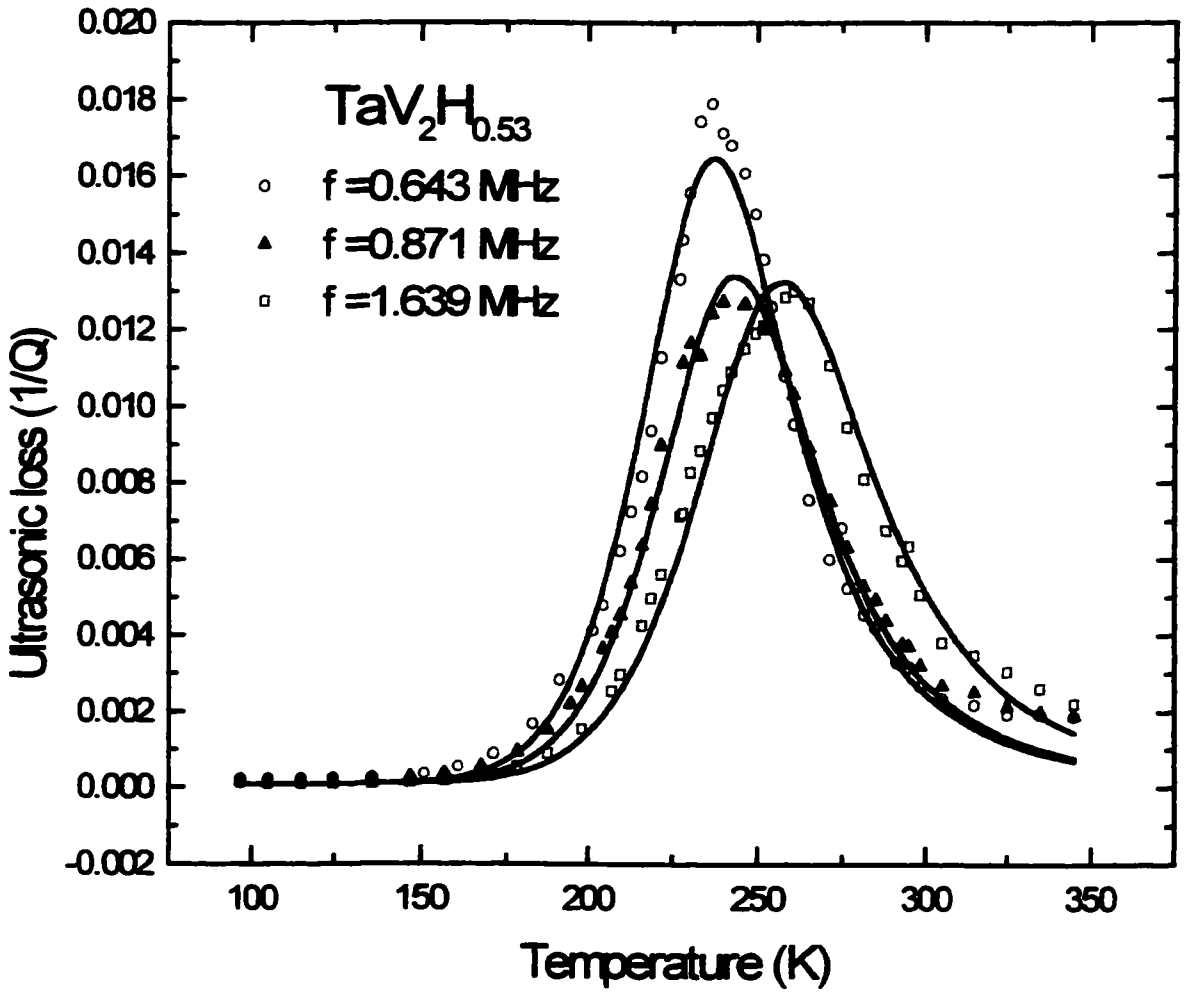

Figure 3.6: Temperature dependence of the ultrasonic loss in $TaV_2H_{0.53}$. The solid lines represent theoretical fits to the data using Eqs. (5), (11) and (14) with parameters given in table 3.1.

ultrasonic measurements. The parameters derived from the fits are listed in table 3.1 with the NMR results of Skripov *et. al.* [35] for comparison. There is excellent agreement between the activation energies derived by both techniques although there is greater deviation in the attempt frequencies.

Table 3.1: Parameters of hydrogen diffusion for C15 TaV_2H_x (x = 0.34 and 0.53). E_a and τ_{Ro} are the parameters derived from fitting to a single Arrhenius process. The fits are shown by the solid curves in figures 3.5 and 3.6. Estimated uncertainties are ± 0.01 eV in activation energies E_a, and ± 30 % in pre-exponential factors τ_{Ro}. Also included are parameters of hydrogen diffusion for C15 TaV_2H_x (x = 0.22 and 0.56) derived from NMR results by Skripov *et. al* [35].

Sample	Activation Energy E_a (eV)	Attempt time τ_{Ro} (s)
$TaV_2H_{0.34}$ (RUS)	0.22	5.7 E-12
$TaV_2H_{0.53}$ (RUS)	0.23	3.9 E-12
$TaV_2H_{0.22}$ (NMR)	0.23	2.5 E-12
$TaV_2H_{0.56}$ (NMR)	0.24	1.1 E-12

We attempted to fit the attenuation results for the lower H concentrations (x = 0.06, 0.10 and 0.18) to the same model. Figure 3.7(a) shows attenuation results for $TaV_2H_{0.06}$ at frequencies of 0.741, 1.431 and 1.931 MHz over a temperature range of 25 - 345 K. The solid lines in this figure are fits to the data using the form of the relaxation time given by **Eq.** (14). A clear 'undercut' on the low-temperature side of the attenuation peaks was observed and the shift to higher temperatures for higher frequency modes could not be accounted for as satisfactorily. This small but systematic undercut was also found

in fits to all analyzed modes of $TaV_2H_{0.10}$ and $TaV_2H_{0.18}$. Pulsed-field-gradient (PFG)-NMR experiments [59][60] on a number of Laves-phase materials showed marked deviations from simple Arrhenius behavior below 200 K for the diffusivity D^*. The data could be described across the entire temperature range of study (130 - 430 K) by considering D^* as a sum of two Arrhenius terms. Motivated by this analysis, we assumed that the relaxation rate in TaV_2H_x is due to the sum of two rates,

$$\tau_R^{-1} = \tau_1^{-1} + \tau_2^{-1} \tag{15}$$

where

$$\tau_i = \tau_{oi}\exp(E_i / k_B T) \tag{16}$$

with $i = 1, 2$. The experimental data for TaV_2H_x for $x = 0.06$, 0.10 and 0.18 were fit using **Eqs.** (5), (11), (15) and (16). The experimental data and the results of these fits for $x =$ 0.06, 0.10 and 0.18 are shown in figures 3.7(b), 3.8(a) and (b) respectively. Again 3 - 4 modes for each concentration were fit simultaneously to the same parameters and good agreement between the theoretical fits and the experimental data was found. The parameters derived from these fits are presented in table 3.2.

Using the relaxation strengths, relaxation times and activation energies derived from the attenuation results (tables 3.1 and 3.2) the observed temperature dependence of the resonant frequencies was successfully accounted for by **Eq.** (13) for all H concentrations, where f was taken to be the room-temperature frequency. Figures 3.9(a) and (b) are plots of the frequencies of mechanical eigenmodes versus temperature for $TaV_2H_{0.10}$ and $TaV_2H_{0.53}$ respectively. Included in these figures are the corresponding

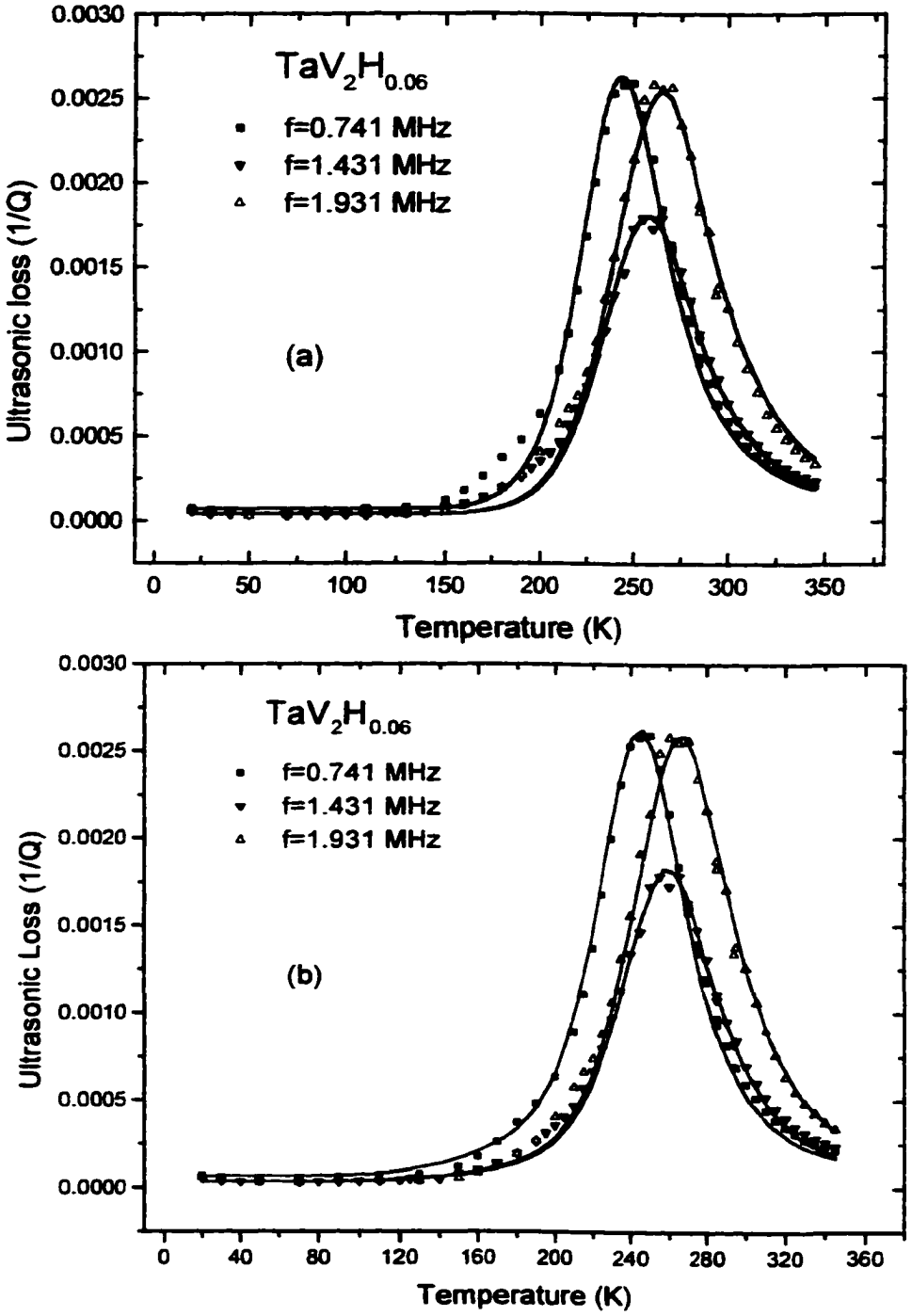

Figure 3.7: Temperature dependence of the ultrasonic loss in $TaV_2H_{0.06}$. (a) The solid lines represent theoretical fits to the data using Eqs. (5), (11) and (14). A significant 'undercut' on the low-temperature side of the peaks can be observed. (b) The solid lines represent theoretical fits to the data using Eqs. (5), (11), (15) and (16).

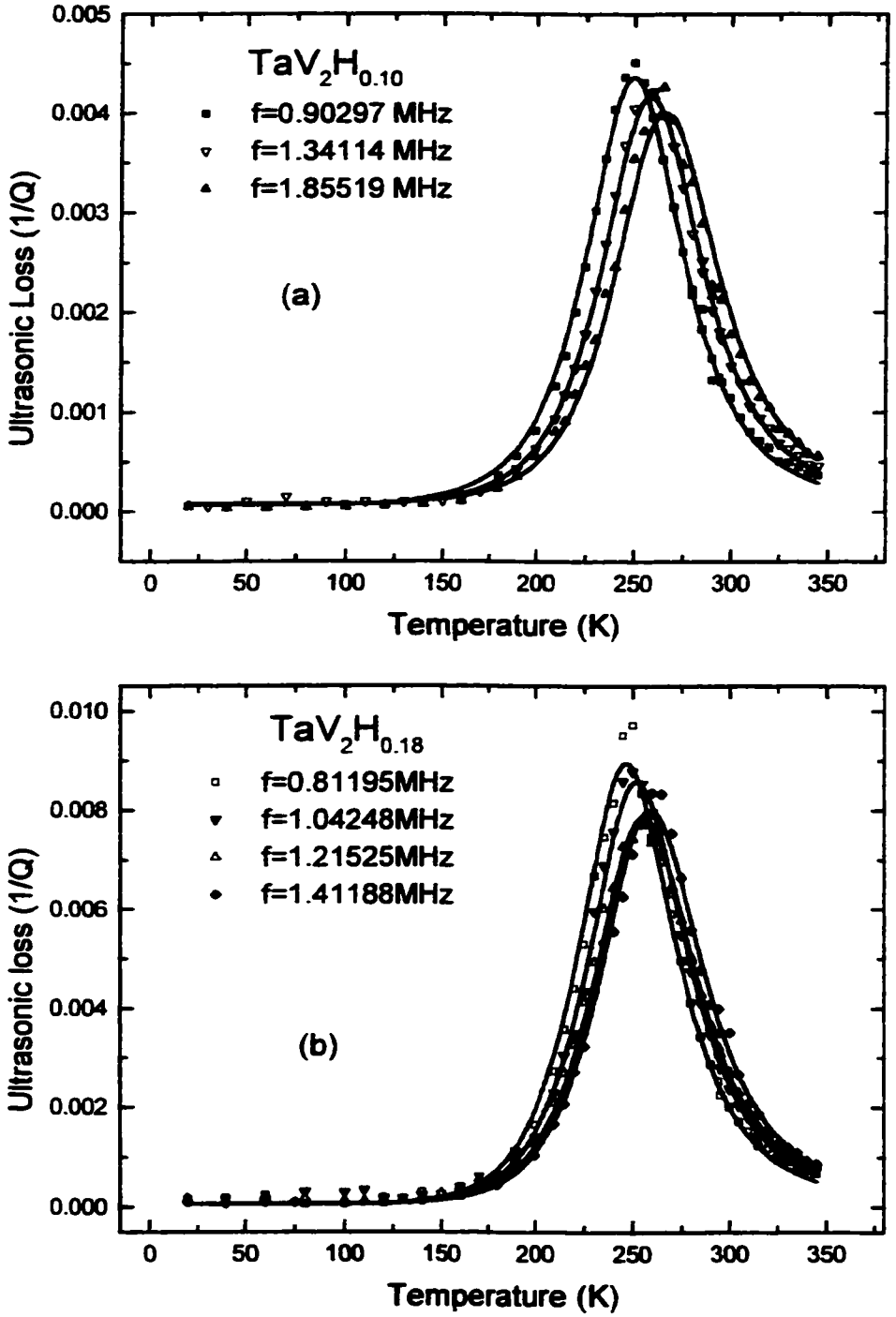

Figure 3.8: Temperature dependence of the ultrasonic loss in: (a) $TaV_2H_{0.10}$ and (b) $TaV_2H_{0.18}$. The solid lines represent theoretical fits to the data using **Eqs.** (5), (11), (15) and (16) with parameters given in table 3.2.

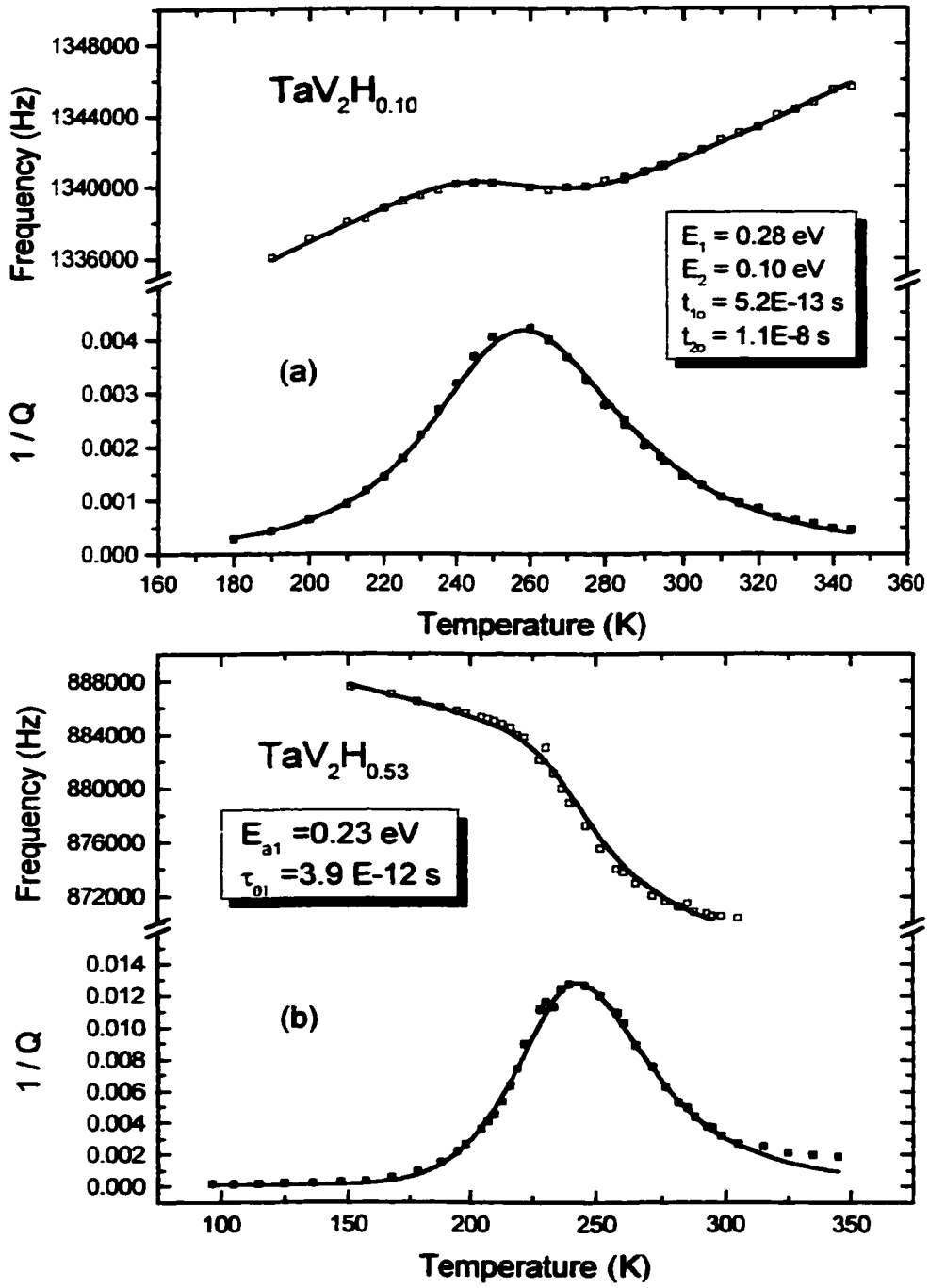

Figure 3.9: Temperature dependence of the resonant frequency and attenuation of a mechanical eigenmode in (a) $TaV_2H_{0.10}$ and (b) $TaV_2H_{0.53}$. The solid lines represent theoretical fits to the data with parameters given in tables 3.1 and 3.2. A background term linear in temperature was included in both frequency fits.

Table 3.2: Parameters of hydrogen diffusion for C15 TaV_2H_x (x = 0.06, 0.10 and 0.18). The sum of two Arrhenius rates with the parameters E_{a1}, E_{a2}, τ_{01} and τ_{02} was used to describe the ultrasonic attenuation data. The fits are indicated by the solid curves in figures 3.7(b), 3.8(a) and (b). Estimated uncertainties are ± 0.01 eV and ± 0.02 eV in activation energies E_{a1} and E_{a2} respectively, and ± 30 % in pre-exponential factors τ_{01} and τ_{02}.

Sample	E_{a1} (eV)	E_{a2} (eV)	τ_{01} (s)	τ_{02} (s)
$TaV_2H_{0.06}$	0.27	0.08	6.2 E-13	5.0 E-9
$TaV_2H_{0.10}$	0.28	0.10	5.2 E-13	11.0 E-9
$TaV_2H_{0.18}$	0.27	0.12	9.6 E-13	6.0 E-9

attenuation results for the same eigenmode on the same temperature scale for direct comparison. Steps in the frequencies are seen. The solid lines in figures 3.9 are theoretical fits to the frequency data using the *same* parameters used to fit the attenuation data. It is seen that the quality of the theoretical fits to both the attenuation and frequency data using the same relaxation parameters is high. In all cases a background term linear in temperature was included in the fits to the frequency data. It can be seen from examination of figures 3.9(a) and (b) that the background temperature dependence of the resonant frequency of $TaV_2H_{0.10}$ is reversed as compared to that of the higher concentration materials. This reversal has been attributed to an electronic band structure effect [61][62] and is discussed in section 3.4.

We now turn to a discussion of the parameters of tables 3.1 and 3.2. To facilitate the discussion the rates given by these parameters are plotted in figure 3.10. As the figure shows, for the lowest concentration, x = 0.06, there is a clear break in the plot at a

temperature of about 225 K. The point at which the break occurs decreases in temperature with increasing concentration. The two Arrhenius terms for the lower concentrations begin to merge with the single Arrhenius term for the higher concentrations, at least for the temperature range over which there was a measurable attenuation. This suggests that the relaxation rates for the higher concentrations may also be due to a two-Arrhenius process, but these may not be distinguishable from a single-Arrhenius process for the temperature range covered. Figure 3.10 looks remarkably like the results of Renz *et al.* [59] for PFG-NMR diffusion measurements of H in the C15 Laves-phase material $ZrCr_2H_x$. The break occurs at roughly the same temperature and the concentration dependence is very similar. We follow the interpretation of Renz *et al.* [59] associating one process with phonon-assisted tunneling through an excited state and the other with phonon-assisted tunneling between the ground states. The attempt frequencies for the higher activation energy process are $\tau_{01}^{-1} \approx 1 - 2 \times 10^{12}\ s^{-1}$ which are much lower than the typical hydrogen vibration frequencies of $\nu_H \approx 3 - 4 \times 10^{13}\ s^{-1}$; however these attempt frequencies are closer to the Debye frequency which was estimated [61][62] as $\nu_D \approx 6 \times 10^{12}\ s^{-1}$ for TaV_2. The theory of quantum diffusion indicates that τ_{01}^{-1} should be of the order of the Debye frequency [7][63]. Figure 3.10 indicates that process 2, attributed to tunneling between the ground states, becomes weaker as the concentration x increases. The phonon-assisted tunneling between ground states is expected to be very sensitive to the tunneling matrix element. It may be that the expansion of the lattice associated with the higher H concentrations leads to an increased tunneling distance suppressing process 2

at the higher concentrations.

A significant feature of the present results is that a single relaxation rate fits the results (even though this rate may have contributions from two processes), a distribution is not required. This implies that the hexagon to hexagon H hopping in TaV_2 involves a specific jump process.

Eq. (11) shows that the relaxation strength is given by $nD^2/[k_BcT]$. The temperature dependence is taken into account explicitly in fitting the data. Thus, the fits determine $nD^2/[k_Bc]$. For each concentration, vibrational modes were selected which depended almost entirely (> 99 %) on the aggregate shear modulus (G). (In the present case G depends rather strongly on the hydrogen concentration as will be reported in section 3.4.) Using measured values of G for each concentration the quantity nD^2/k_B was determined. Figure 3.11 shows this quantity plotted *vs.* n where we assume that n is the hydrogen concentration. The linear dependence shown is exactly what is expected for single interstitial hydrogen atoms, i.e. the Snoek effect. This appears to be an extremely clear demonstration of the Snoek effect for hydrogen in crystalline metals and indeed is one of the first studies which has clearly highlighted a linear relationship between the H concentration and the relaxation strength in this way. The slope of the plot of figure 3.11 gives $D = 0.17$ eV. This value is close to that estimated for anelastic relaxation for hydrogen in scandium and yttrium [53][64].

As was discussed earlier, both NMR and neutron measurements indicated the presence of a second, more localized H motion in the TaV_2H_x system which persisted

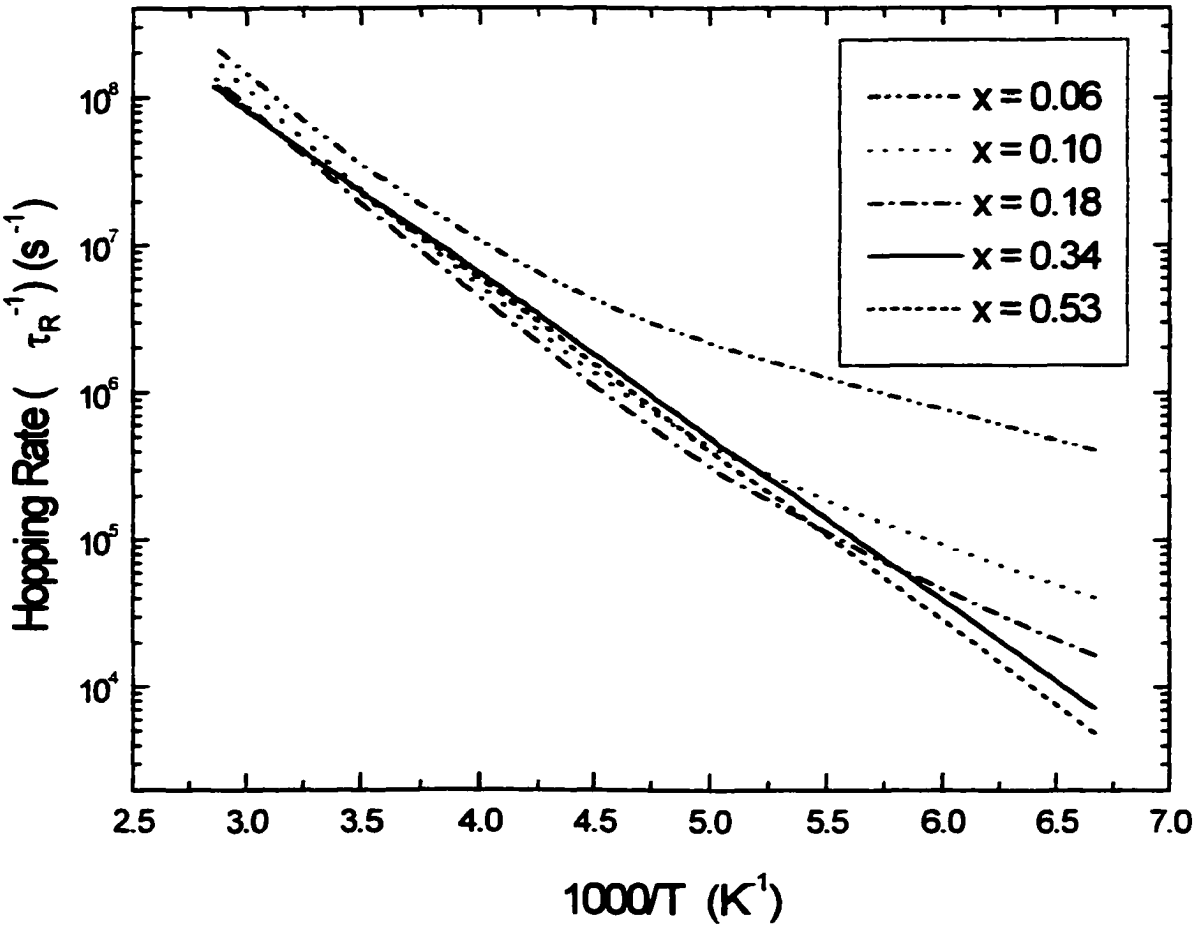

Figure 3.10: Relaxation rates calculated from the parameters given in tables 3.1 and 3.2.

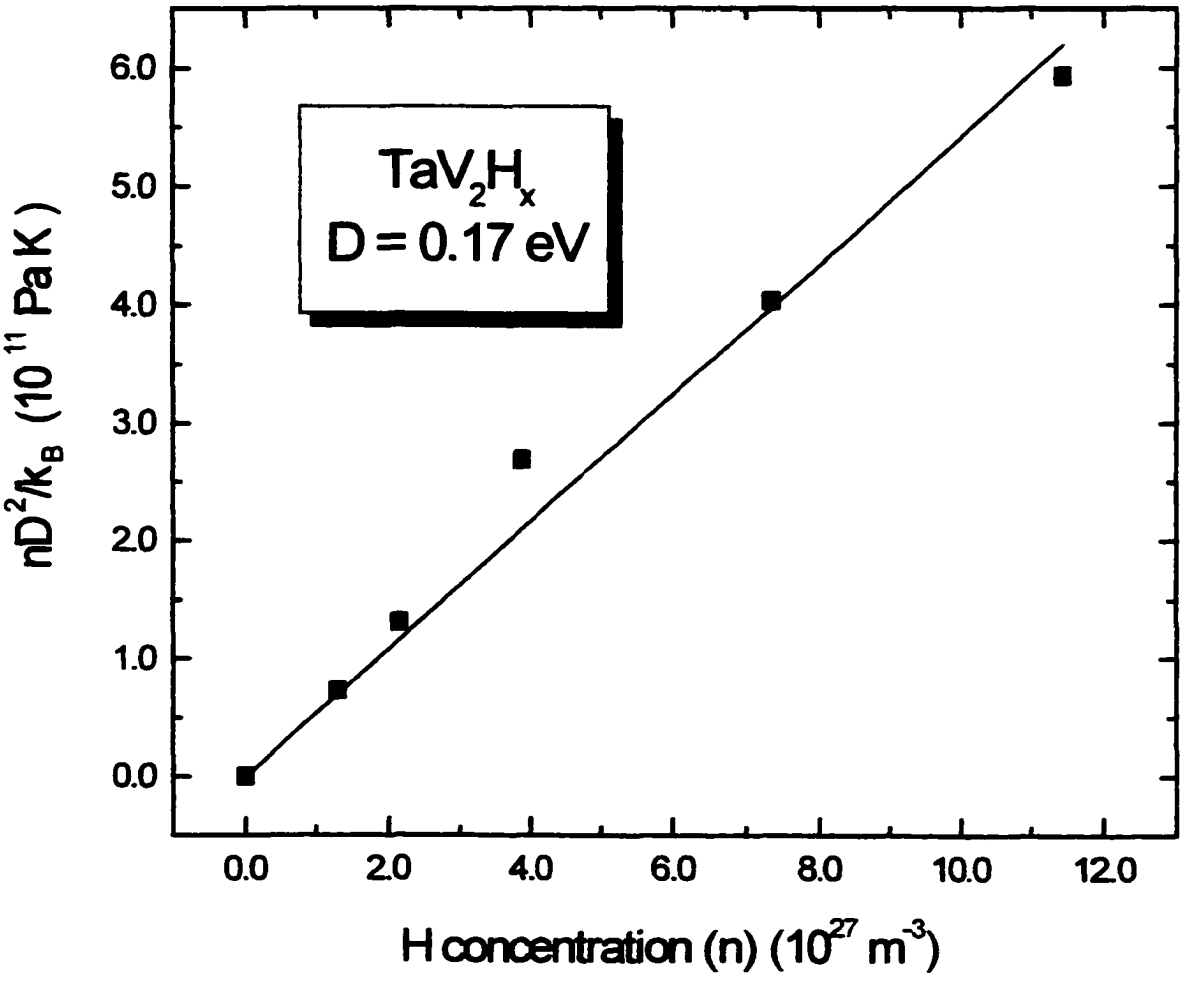

Figure 3.11: Relaxation strength versus the volume hydrogen concentration (n) for TaV_2H_x determined from ultrasonic measurements. The slope of the straight line was used to derive the variation of the energy level splitting with respect to the ultrasonic strain, D.

down to low temperatures. The neutron results implied that the local motion consists of H hopping about g sites within a hexagon [38][39]. This motion produced the double-peaked dependence in the proton spin-lattice relaxation results [35]. These measurements indicated that only a fraction of the H atoms participates in the local motion, with this fraction increasing with increasing temperature. The dynamics of this motion are considerably more rapid than that of the longer range hexagon to hexagon diffusion. As the local motion is about g sites it is expected, from symmetry considerations, that this motion should also couple to the ultrasonic strain leading to an attenuation peak. No such peak was found for any of the hydrogenated samples studied. Section 3.3 will however report findings of a small attenuation peak observed in $TaV_2D_{0.17}$ which has been associated with the local motion. It is believed the most likely reason for the absence of a peak in the hydrogenated materials is because the hopping rate of the local H motion is occurring at frequencies higher than the ultrasonic frequency even down to 15 K. It is also possible that too few H atoms participate in the local motion for the effect to be seen in the present measurements.

3.2.4 Concluding Remarks

Hydrogen motion in the C15 Laves-phase material TaV_2H_x has been studied by means of resonant ultrasound spectroscopy over the temperature range of 15 - 345 K. Hydrogen concentrations of x = 0.00, 0.06, 0.10, 0.18, 0.34 and 0.53 were studied. Attenuation peaks and frequency shifts (dispersion) associated with the hydrogen motion were observed in all the hydrogen containing materials. These effects were centered

roughly at 240 K for measurement frequencies of about 1 MHz. For each concentration the two effects, attenuation and dispersion, were fit by the same parameters (activation energies, attempt frequencies, and relaxation strengths) for the hydrogen motion. The parameters of the hydrogen motion indicated that hopping between g-site hexagons was observed, the motion responsible for long-range diffusion. The relaxation rates for $x \leq 0.18$ were best described as a sum of two Arrhenius processes which, following earlier work on other Laves-phase materials, were interpreted as phonon-assisted tunneling between ground states and between excited states. For $x = 0.34$ and 0.53 only a single Arrhenius process was needed to fit the results, although the two-Arrhenius mechanism cannot be ruled out from these measurements over the given temperature range. The activation energies and hopping rates derived from the ultrasonic data for $x \geq 0.34$ are in good agreement with NMR spin-lattice relaxation measurements probing the same process at higher temperatures. It should be noted that the two-Arrhenius process for the lower concentrations is not necessarily incompatible with the NMR results because that work was performed at much higher frequencies resulting in maxima in T_1^{-1} above 300 K. The second Arrhenius process, hopping at a rate given by τ_2^{-1}, would have a negligible contribution compared to that of the τ_1^{-1} mechanism at these higher temperatures. It is noteworthy that a single relaxation rate was needed to fit the data; a distribution of rates was not required. The magnitudes of the attenuation and dispersion depended linearly on the hydrogen concentration implying that it is the relaxation of isolated H atoms that is

responsible for the mechanical damping. These results show that a Snoek effect due to hydrogen exists in C15 structures.

3.3 Ultrasonic Evidence for Strong Isotope Effects on the Local Motion of H(D) in $TaV_2H(D)_x$

3.3.1 Introduction

In the C15 Laves-phases the g-g distance for neighboring g sites *within* the same hexagon, r_1, is usually shorter than the g-g distance for g sites on *different* hexagons r_2. The present experimental evidence indicates that the slower, rate-limiting step for long-range diffusion involves H(D) hops between hexagons, while the faster, local motion involves hops within the same hexagon. There is much that is not understood about this local motion. Only a small fraction of H(D) atoms participates in the local motion and this fraction appears to be both isotope and temperature dependent. There are similarities to the situation in the rare-earth metals where there are at least two frequency scales of motion, and where there is NMR evidence for a local motion in which only an isotope-dependent fraction of the H(D) atoms participate [65]. NMR and QENS have been the primary techniques used to study dynamics of H(D) in the Laves-phase materials. However, ultrasonic methods, and mechanical spectroscopy in general, are especially well-suited to studying isotope effects in that the coupling between the ultrasound and the H(D) atoms is not sensitive to isotope mass, cross-section, or spin, so that the measured

isotope effects reflect the motion of the isotopes, independent of the coupling mechanism. Furthermore, mechanical spectroscopy can explore a much lower frequency range than the other techniques. Because the motion is usually temperature dependent, the lower frequencies essentially explore a different temperature range. As a result, it is possible that ultrasonic measurements at relatively low frequencies may reveal two attenuation peaks well-separated in temperature due to the two types of motion.

A series of studies [66] have shown a strong correlation between the parameters of the two jump processes and the two g-g distances r_1 and r_2. In comparison to a number of C15 Laves-phase compounds the ratio r_1/r_2 is least for TaV_2 while the ratio of the fast jump rate to the slow jump rate is greatest in this compound [39]. Measurements of the temperature dependence of the nuclear spin-lattice relaxation rates for ^1H, ^2D, and ^{51}V in $TaV_2H(D)_x$ showed two overlapping maxima due to H(D) motion, with the maximum at lower temperature being attributed to the local motion. While the high-temperature motion exhibited Arrhenius behavior, the lower temperature motion was strongly non-Arrhenius. The measurements of the spin-lattice relaxation of ^{51}V due to quadrupolar interactions with the moving H and D atoms revealed isotope effects [35]. The results indicated that the local motion (and indeed long-range motion) of D was somewhat slower than that of H for a given concentration and temperature. More striking, however, was the fact that the ^{51}V relaxation rate due to D was considerably greater than that due to H. This effect was interpreted as the fraction of D atoms participating in the local motion being about three times that of H, both fractions increasing with temperature.

This section reports ultrasonic attenuation and elastic constant measurements in

$TaV_2H_{0.18}$ and $TaV_2D_{0.17}$ over the temperature range of 3 K - 345 K.

3.3.2 Experimental Details

Polycrystalline ingots of TaV_2 were prepared as described in section 3.2.2. The TaV_2 material was then loaded with H or D to obtain $TaV_2H_{0.18}$ and $TaV_2D_{0.17}$ in a manner described elsewhere [37]. Resonant Ultrasound Spectroscopy (RUS) was used to measure the ultrasonic loss and elastic constants. The room-temperature sample edge dimensions, in mm, of the $TaV_2H_{0.18}$ and $TaV_2D_{0.17}$ samples were 0.2103*0.1681*0.1903 and 0.1215*0.1697*0.1072 with masses of 65.6 mg and 21.6 mg respectively.

3.3.3 Results and Discussion

Figure 3.12 shows the ultrasonic loss *vs.* temperature over the temperature range of 3 - 345 K for $TaV_2H_{0.18}$ and $TaV_2D_{0.17}$. The frequency of the modes is 1.058 MHz and 1.149 MHz for $TaV_2H_{0.18}$ and $TaV_2D_{0.17}$ respectively. These peaks each depend solely on the aggregate shear elastic constant, not on the bulk modulus. Several things are immediately apparent. A large loss peak centered near 250 - 275 K is observed for both compounds. The origin of these peaks is related to the motion of H about the host lattice and was described in detail in the previous section. The two peaks are of nearly equal amplitude indicating that the coupling of the H(D) motion to the ultrasound depends little, if any, on the isotope. The peaks do indicate a small isotope effect for the H(D) hopping rate; the peak for $TaV_2D_{0.17}$ clearly occurs at higher temperatures for approximately the

same measurement frequency. This indicates that the D hexagon-to-hexagon hopping rate is somewhat lower than that for H, a result consistent with the NMR measurements [35].

More importantly, there is a small loss peak at low temperature for D, *but no such peak is observed for H.* By comparison with the NMR results, this low-temperature peak is associated with the rapid, local motion. The results clearly indicate a large isotope effect for the local motion. Figure 3.13 shows in more detail the low-temperature loss peaks in $TaV_2D_{0.17}$ for four measurement frequencies. The peaks shift slightly to higher temperatures for higher measurement frequencies. Neither the high-temperature or low-temperature peak was observed in the H(D) free material which had a low-level, almost temperature independent attenuation. Figure 3.14 shows the aggregate elastic shear modulus, G, for these polycrystalline samples. Although a more detailed account of the TaV_2H_x modulus measurements will be reported in section 3.4, the important point to notice in figure 3.14 is that the temperature dependence of G clearly differs for the two isotopes. The shear modulus of $TaV_2H_{0.18}$ deviates from an approximately linear temperature dependence below about 20 K, but this does not happen for $TaV_2D_{0.17}$. Due to uncertainties in sample dimensions and density, the absolute error in G is about 1%, thus the difference in absolute values of the shear modulus for the two materials is just marginally outside experimental error. The error in the temperature dependence is much smaller and is essentially given by the scatter in the data.

The high-temperature ultrasonic loss peaks are analyzed in an identical manner to those described in section 3.2. Figures 3.15 (a) and (b) show more attenuation data for the high-temperature peaks, for both compounds, along with fits using thermally activated

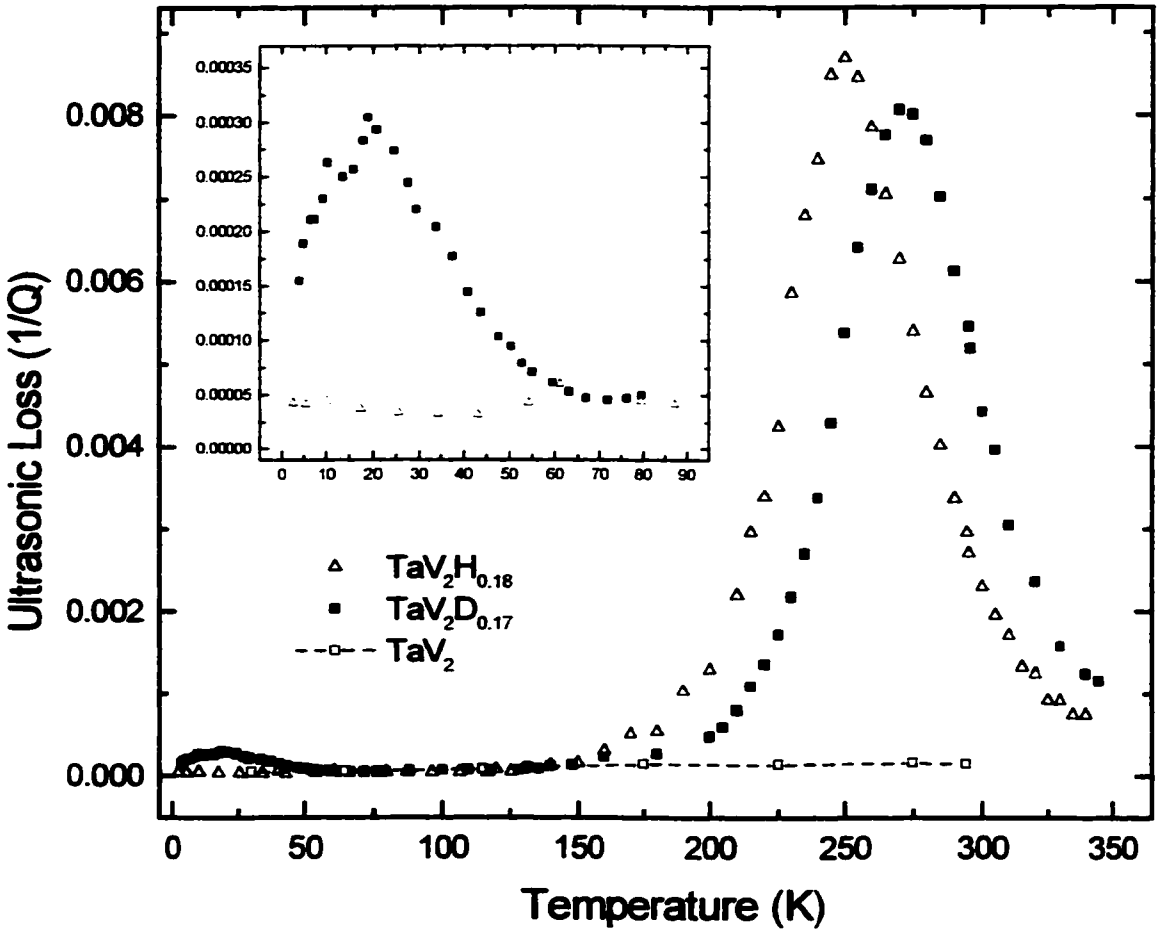

Figure 3.12: Ultrasonic loss *vs.* temperature for $TaV_2H_{0.18}$, $TaV_2D_{0.17}$, and TaV_2 over the range of 3 - 345 K. The ultrasonic frequency was approximately 1 MHz for all modes shown.

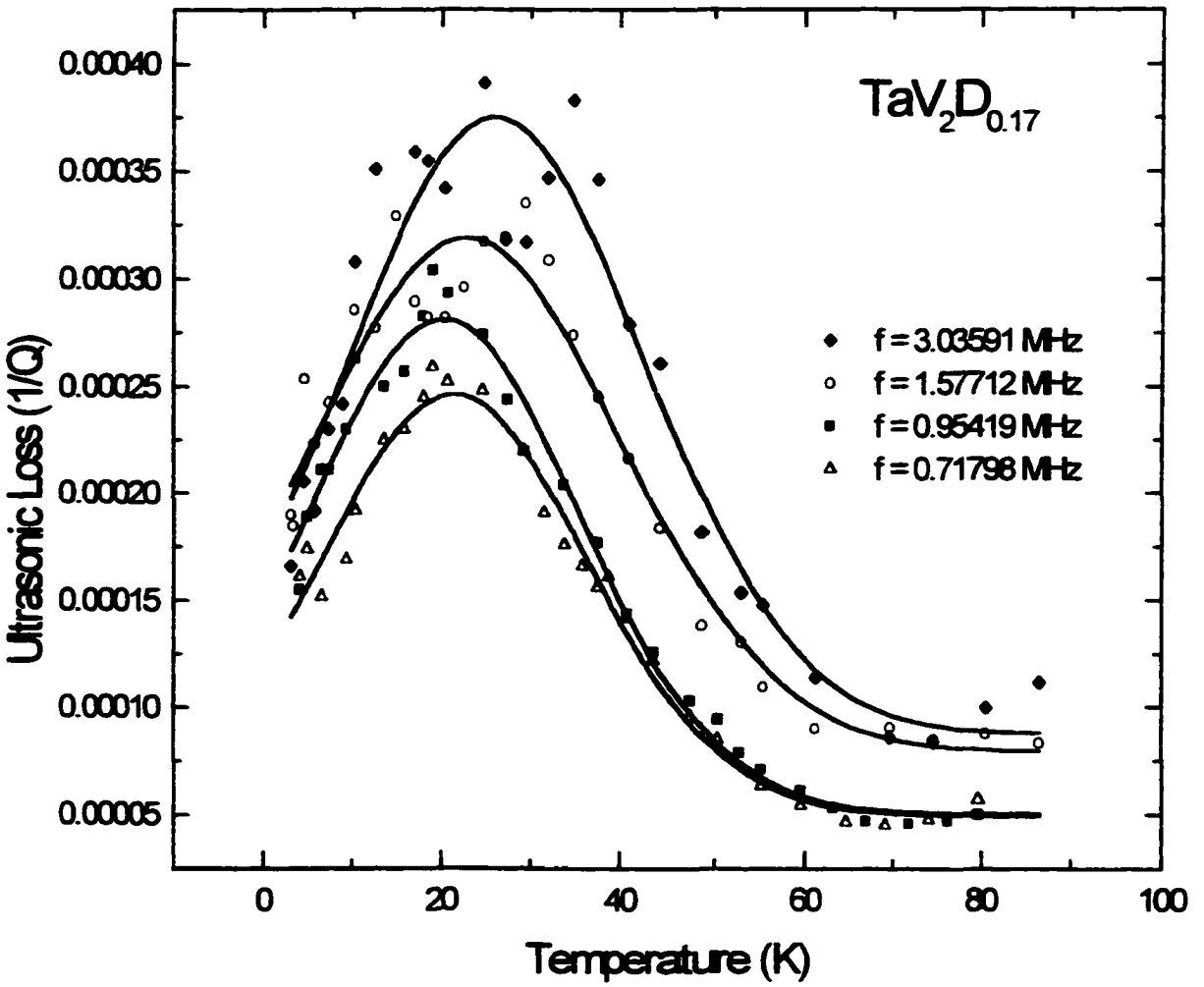

Figure 3.13: Expanded view of the low temperature ultrasonic loss peak in of $TaV_2D_{0.17}$ for four vibrational modes. The solid lines are guides to the eye and do not represent theoretical fits to the data.

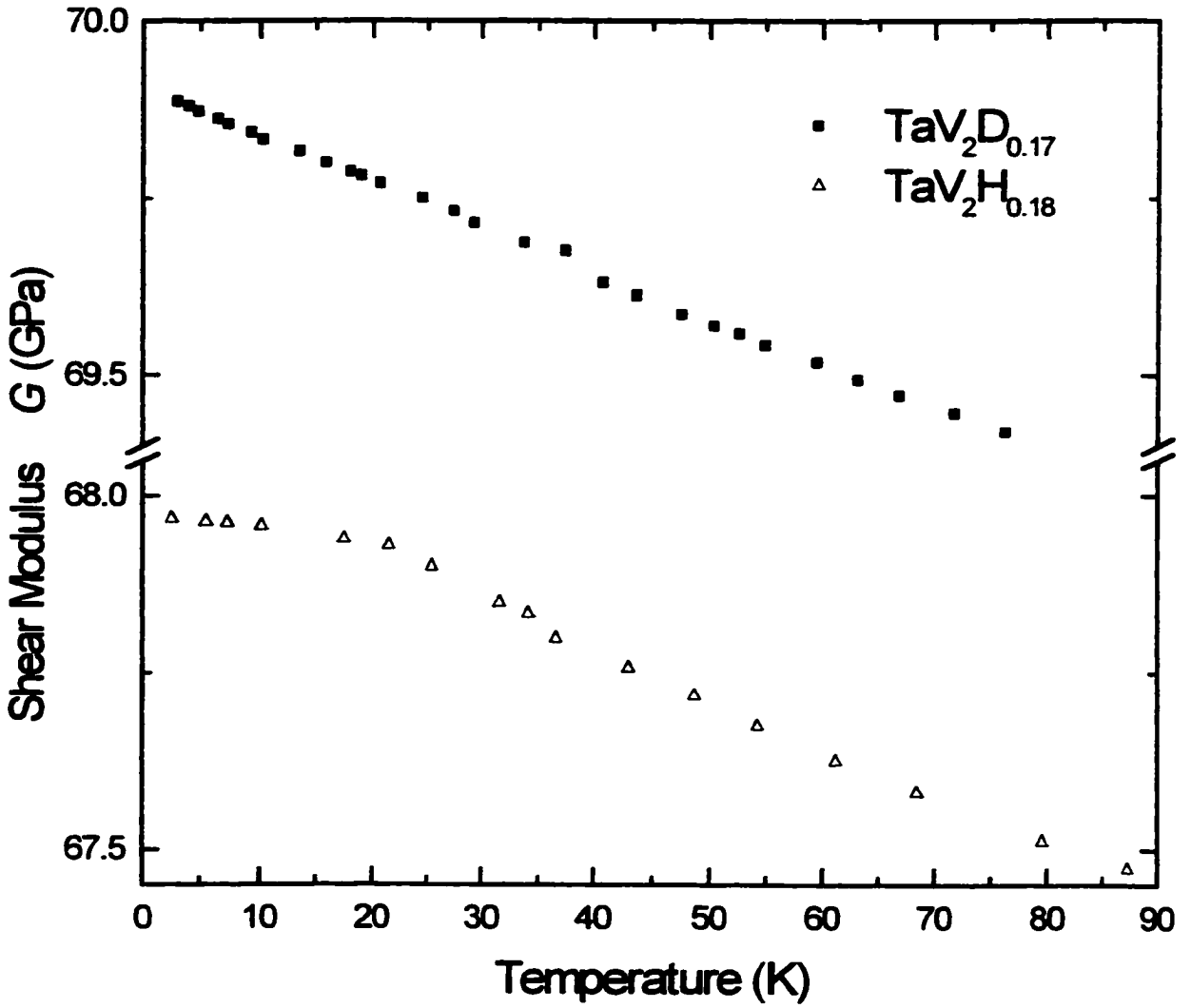

Figure 3.14: Elastic shear modulus (G) for polycrystalline $TaV_2H_{0.18}$ and $TaV_2D_{0.17}$ in a range of 3 - 90 K.

hopping for τ_R. For $TaV_2D_{0.17}$ the data for two different measurement frequencies (1.1490 and 2.2626 MHz) were fit using the simple Arrhenius expression given by **Eq.** (14). The derived values of τ_{R_o} and E_a are 6.0 x 10^{-13} s and 0.29 eV respectively. The solid lines in figure 3.15 (a) are fits using these parameters. The agreement between experiment and theory is clearly rather good. This value for E_a is in reasonable agreement with the NMR results at higher temperatures and concentrations. Skripov *et al.* [35] found an activation energy of 0.26 eV for $TaV_2D_{0.50}$ in the 300 - 400 K range. While the data for $TaV_2H_{0.18}$ could be fit reasonably well with the same approach, it was found that a consistently better fit was found by taking the hopping rate for H as the sum of two Arrhenius rates, given by **Eqs.** (15) and (16). Figure 3.15 (b) shows the fit of the data for $TaV_2H_{0.18}$ for four different measurement frequencies (0.8 - 1.4 MHz). The results of the fit gave (9.6 x 10^{-13} s, 0.27 eV) and (6.0 x 10^{-9} s, 0.12 eV) for (τ_{o1}, E_{a1}) and (τ_{o2}, E_{a2}) respectively. The interpretation of the two processes was described in section 3.2.3. It was discussed that the attempt frequencies of the higher activation energy process ($\tau_0^{-1} \approx 1 - 2 \times 10^{12}$ s^{-1}) are much lower than typical values [67] for the H(D) vibrational frequencies ($\nu_{H,D} \approx 2 - 4 \times 10^{13}$ s^{-1}). However the attempt frequencies were shown to be much closer to the Debye frequency of TaV_2 which was estimated as $\nu_{Debye} = 6 \times 10^{12}$ s^{-1}. This implies [7][63] that there is a quantum component to the H(D) diffusion in TaV_2 and which then accounts in a natural way for the absence of process 2

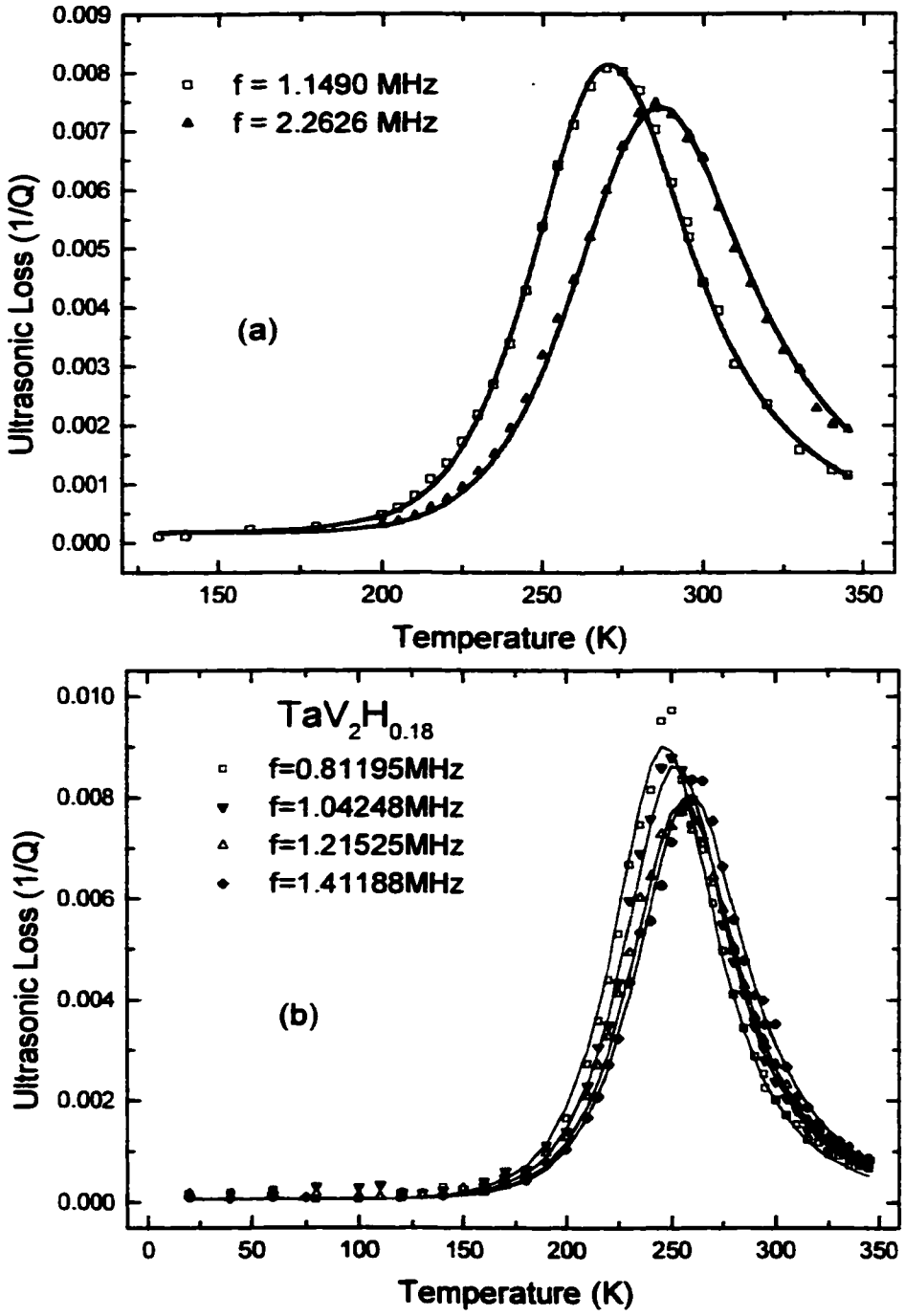

Figure 3.15: Expanded view of the high temperature ultrasonic loss peaks: (a) $TaV_2D_{0.17}$. The solid lines represent theoretical fits to the data using Eqs. (5), (11) and (14) (b) $TaV_2H_{0.18}$. The solid lines represent theoretical fits to the data using Eqs. (5), (11), (15) and (16).

for D. Tunneling between ground states is expected to be especially sensitive to the mass of the tunneling particle; process 2 may be suppressed for D due to the larger mass. The slightly higher value of E_a^D as compared to $E_{al}{}^H$ is in agreement with Skripov *et al.* [35] who found a slightly higher activation energy for D as compared to H for comparable concentrations.

In contrast to the high-temperature peak in $TaV_2D_{0.17}$, which is well-described with an Arrhenius-type process, the low-temperature peak behaves quite differently. An activation energy of ~10 meV would be required to describe the shift of the peaks with the ultrasonic measurement frequency, and also to reconcile the present results with the earlier NMR results. However, an activation energy of this value gives loss peaks which are too narrow, and have the wrong shape, to describe the actual data. Thus, it seems that a simple Arrhenius process will not describe the low temperature peak; this conclusion is in agreement with the NMR results obtained at higher temperatures. The broad, asymmetric loss peaks could, no doubt, be fit with a distribution of activation energies, but there seems little justification for such an approach especially given that the high-temperature peak requires only a single activation energy. In fact, the NMR results are also inconsistent with a broad distribution of frequencies of the localized motion. Skripov *et al.* [35] were able to fit the low-temperature spin-lattice relaxation with an expression $\tau_{L} = \tau_{L_0} \exp(-T / T_0)$ for the hopping time at low temperatures where T_o and τ_{Lo} are fitting parameters. Such an expression has some justification from the theory of quantum diffusion [68]. Using this expression for the relaxation time in Eq. (5), good fits to the low-temperature peaks were achieved, for each *particular* frequency. However, this

expression does not successfully account for the shift of the peaks with measurement frequency. Further complicating the attempt to give a theoretical description of the low temperature peak is the fact that NMR and QENS results indicated that only a fraction of the D atoms participate in the local motion, and that this fraction is temperature dependent. As a result, the temperature dependence of the relaxation strength $\Delta c/c$. is not clear at this point. However, certain observations are possible. Clearly, the low-temperature peak is much weaker than the high temperature peak. To proceed further we assume that the relaxation strength varies as nD^2/T where n is the concentration of participating D atoms. Furthermore, for a crude estimate we assume that D is the same for the high-temperature and low-temperature peaks. This assumption may be reasonable because g sites are apparently involved in both cases. Comparing the peak heights at 250 K and 20 K leads to an estimate of $n_l = 3 \times 10^{-3} n_h$ where n_l and n_h refer to the concentration of D atoms participating in the low and high temperature peaks respectively. Assuming that essentially all the D atoms contribute to the high-temperature peak it is estimated that only 0.3 % of D atoms participate in the local motion at 20 K. Skripov *et al.* [39] estimated the fraction of H atoms participating in the local motion by QENS measurements over the temperature range of 80 - 300 K. Extrapolating their results for $TaV_2H_{0.6}$ down to 20 K gives 3.7 % as the participating concentration of H. However, NMR measurements [35] at much higher temperatures indicated that the fraction of D atoms participating in the local motion is about three times that of H. Thus, the QENS and NMR results at higher temperatures extrapolated to 20 K give an estimate of about 10

% participating D. This is much larger than our estimate of 0.3 %. This disagreement may indicate that the extrapolation is invalid, or that one of the assumptions about $\Delta c/c$ is incorrect. Also, the QENS and NMR measurements were at higher H(D) concentrations than the present measurements.

The most remarkable feature of the present results is the absence of a low-temperature peak for the hydrogen-containing material. There are at least two possibilities for this absence. Firstly, the number of participating H atoms may be too low to result in an observable peak. However, if the factor of three found from NMR measurements holds for the present case a low-temperature peak should be observed. Figure 3.12 indicates that a peak approximately a factor of ten weaker than that found for D would just be observable. Secondly, it may be that the local motion remains at a rate well above the ultrasonic frequency even down to 3 K so that the condition $\omega\tau_R << 1$ holds throughout the temperature range of the measurements. This high value of the local relaxation rate is consistent with the NMR measurements. Some support for this second viewpoint is also found from the modulus measurements. Tunneling motion can lead to a resonant decrease in the sound velocity at low temperatures [15][69]. In brief, H would be expected to have a larger tunneling matrix element than D due to the mass difference. The different temperature dependencies for the shear modulus of $TaV_2H_{0.18}$ and $TaV_2D_{0.17}$ could be due to the onset of the resonant process for H as the temperature is lowered. Thus, rapid tunneling by H could account for both the absence of a low-temperature peak for H (the relaxation rate remains well above the ultrasonic frequency) and the different temperature dependencies for the moduli. The downturn in the modulus at low T depends on both the

tunneling matrix element and any asymmetries which exist among the interstitial sites. The present data are insufficient to determine these parameters.

3.3.4 Conclusions

The unusual motion reported for H(D) in C15 Laves-phase compounds has been investigated in $TaV_2H_{0.18}$ and $TaV_2D_{0.17}$ by means of ultrasonic measurements. An ultrasonic loss peak at 250 - 275 K for measurement frequencies in the range of 1 MHz was observed in both materials and interpreted as H(D) hopping between g-site hexagons, the motion responsible for long-range diffusion. This motion exhibited a small isotope effect with the H hopping rate being somewhat faster than that for D. The activation energies and attempt frequencies were in good agreement with earlier measurements. In contrast to the similarity of the $TaV_2H_{0.18}$ and $TaV_2D_{0.17}$ results at high temperatures, the low-temperature behavior of the two materials differed substantially. A weak loss peak was observed in $TaV_2D_{0.17}$ at low temperatures. This peak was attributed to the local motion within g-site hexagons previously explored by NMR and QENS experiments. The rate for this motion is several orders of magnitude faster than that of the high-temperature peak. No evidence of a low-temperature loss peak was found for $TaV_2H_{0.18}$. This strong isotope effect suggests that the local motion is highly dominated by quantum effects. The most likely reason for the absence of an attenuation peak in $TaV_2H_{0.18}$ is that the local motion is occurring at a rate much higher than that of the ultrasonic frequency (~ 1 MHz) throughout the temperature range explored (down to 3 K). To explore these ideas further, future experiments at lower temperatures and higher H concentrations are planned

at Colorado State.

3.4 Strong Hydrogen-related Electronic Effects on the Elastic Shear Modulus of $TaV_2H(D)_x$

3.4.1 Introduction

The temperature (T) dependence of the elastic constants is directly related to the anharmonic nature of lattice vibrations. The lattice vibrations typically result in a T^4 term at low temperatures and a term linear in temperature at higher temperatures [70]. In metals there is also a contribution from the conduction electrons. For simple metals the electrons contribute a T^2 term at low temperatures [71]. Volume effects, through the thermal expansion of the crystalline lattice also play a significant role. The overall result, for typical materials, is that the elastic moduli approach 0 K with zero slope and decrease monotonically with increasing temperature. This simple picture is not applicable to materials undergoing phase transitions [72][73] or for materials with more complicated electronic structures [74].

The elastic constants of the Laves-phase compounds have been the subject of a large number of theoretical [75][76][77] and experimental [78][79][80][81][82][83][84] investigations. The elastic properties of the Laves-phases have created interest for a variety reasons. Firstly, the Laves-phase alloys form the largest single group in the topologically close-packed (TCP) set of materials. The TCP materials [85] have relatively

low densities and high melting-point temperatures and have shown some potential for use in high-temperature structural applications. The fcc C15 Laves-phases are particularly good candidates for materials applications as they exhibit the best deformation characteristics of the three Laves-phase polytypes. To systematically identify compounds for particular applications, an understanding of their basic elastic properties is required [86][87]. Secondly, a number of Laves-phase alloys (e.g. HfV_2 and ZrV_2) are known to be type II superconductors with superconducting transition temperatures which are reasonably high for intermetallic materials [88][89][90][91][92]. In some cases it was found [88][93] that the superconducting transition was preceded by a structural phase change at higher temperatures (~100 K).

Laves-phase HfV_2 and ZrV_2 show rather unusual elastic properties, with a number of elastic moduli exhibiting anomalous temperature dependencies. Measurements of the longitudinal-wave sound velocities in polycrystalline HfV_2 and ZrV_2 by Takashima and Hayashi [94] found that the velocities decreased on cooling from room temperature down to ~115 K, but then increased with further cooling. Polycrystalline TaV_2, however, showed only a slight increase in the longitudinal velocity on cooling from room temperature to 4.2 K. Balankin *et al.* [95] measured the temperature dependence of $G(T)$ and $E(T)$ in HfV_2 and ZrV_2. Both compounds showed a V-shaped minimum in $G(T)$ centered at temperatures of ~100 K with an anomalous stiffening with increasing temperature above 100 K up to the vicinity of the melting temperature (~1500 K). A large number of experimental and theoretical studies [94][95][96][97][98] have specifically investigated the possible inter-relationship between the anomalous elastic

properties, lattice instability, and superconductivity observed in the C15 Laves-phases.

The elastic properties of TaV_2 have been studied theoretically and an anomalous temperature dependence was predicted above room temperature [84]. The unusual elastic properties of the early-transition-metal C15 Laves-phase materials have been attributed to an electronic band-structure effect [75][88][97][98]. (Somewhat similar band-structure effects have been studied in bcc Nb alloys [99].) The symmetry of the C15 lattice allows for a double-degeneracy of electronic energy levels at the X point of the irreducible Brillouin zone (IBZ). If the Fermi level of the system lies near the double-degeneracy point, strong effects on the elastic constant may result. For the C15 structure, it can be shown [98] that these electronic energy levels couple to the single-crystal elastic constant c_{44}. The effects are rather sensitive to the distance of the Fermi level from the double-degeneracy point. It has been shown [100] that the addition of hydrogen to a metallic material can raise the Fermi level by contributing electrons to the conduction band. $TaV_2H(D)_x$ has x more electrons per formula unit than TaV_2; so a change in the value of the Fermi level may be expected, with possible associated changes in the elastic constants.

A further motivation came from the simple fact that it appeared as though there had been no previous experimental studies of the temperature dependence of the shear modulus of TaV_2. To explore the effects of hydrogen on the elastic properties of TaV_2, RUS was used to measure the elastic moduli of $TaV_2H(D)_x$ for a series of H(D) concentrations. Measurements were made over a temperature range of 3 - 345 K. The quality of the modulus data permitted a detailed quantitative analysis of the results incorporating the electronic band-structure model. The analysis includes a comparison to

electronic density of states measurements from other experiments. Finally, the question of lattice instability and how this relates to the unusual elastic properties of $TaV_2H(D)_x$ will be addressed.

3.4.2 Experimental Details

The preparation of the $TaV_2H(D)_x$ samples was described in section 3.2.2. However, the reader should be reminded that for the studied range of hydrogen concentrations the $TaV_2H(D)_x$ system does not show any phase transitions down to low temperatures. Ultrasonic measurements were made on samples of $TaV_2H(D)_x$ for x(H) = 0.00, 0.06, 0.10, 0.18, 0.34, and 0.53 and x(D) = 0.17. All samples were accurate RPs with edge dimensions on the order of 1 - 2 mm. Resonant Ultrasound Spectroscopy (RUS) was used to measure the adiabatic polycrystalline elastic moduli. In all cases, the frequencies of 40 - 50 resonances were measured with a typical root-mean-square (rms) difference between the measured and computed frequencies of 0.25 - 0.40 %. For materials with isotropic symmetry, only two independent moduli are required to fully define the elasticity of the system. The aggregate elastic moduli C_{11} and C_{44} were derived directly from the measured frequencies. C_{44} is just the usual polycrystalline shear modulus $G(T)$. The temperature-dependent measurements below room-temperature were made using the Oxford ^{4}He cryostat. Above room-temperature, measurements were made at atmospheric pressure using a commercial oven. The temperature resolution of both experiments was ≈ 0.1 K.

Errors in the mass density result in comparable errors in the absolute values of the

elastic moduli derived from the measured resonant frequencies. The room-temperature densities (ρ_M) as determined by direct measurement of the mass and sample dimensions were used. Taking into account both the rms errors in the RUS fit and those estimated for the density measurements, the resulting overall error in the absolute value of G is approximately 1%. The relative error is, of course, much smaller and is essentially indicated by the scatter in the data.

Theoretical densities (ρ_T) were calculated from the experimentally-determined room-temperature lattice parameters [101]. As can be seen from table 3.3, the measured densities are systematically about 4% lower than the theoretical densities for all the $TaV_2H(D)_x$ compounds. It is not surprising that the measured densities may be somewhat lower than those calculated from the x-ray lattice parameters due to the presence of grain boundaries, dislocations and possible microvoids in the polycrystalline materials. The differences between the two sets of densities, while reasonable, could have some effect on the absolute value of the measured elastic moduli.

Table 3.3: Experimental densities ρ_M were directly determined from the measured mass and dimensions; theoretical densities ρ_T were calculated from measured lattice parameters.

x	0.00	0.06	0.10	0.17 (D)	0.18	0.34	0.53
ρ_M	9.815	9.828	9.738	9.750	9.751	9.708	9.711
ρ_T	10.25	10.22	10.21	n/a	10.17	10.11	10.03
% diff	-4.23	-3.86	-4.58	n/a	-4.15	-3.96	-3.19

Because thermal expansion data are not available for these materials the results

have not been corrected for thermal contraction; the room temperature dimensions and density have been used in the analysis. Taking into account the direct dimensional effects as well as the indirect effect through the density, the elastic constants deduced from the measured frequencies vary inversely with the dimensions. Metals such as Ta and Zr have a total thermal contraction [102] between room temperature and 4 K of less than 0.20 %. Assuming that the materials in the present study behave similarly, neglecting thermal contraction effects in the analysis of the data leads to a comparable error: the total change in the elastic constants as the temperature is lowered from room temperature to 4 K would be roughly 0.15 - 0.20 % higher than the values reported below.

3.4.3 Results and Discussion

Figure 3.16 shows the experimentally determined shear modulus of TaV_2H_x, for x = 0.00, 0.06, 0.10, 0.18, 0.34 and 0.53. It is immediately apparent that the magnitude of the shear modulus of TaV_2H_x systematically increases with increasing hydrogen concentration (x). The effect is greatest at low temperatures but persists across the entire temperature range. At 20 K the shear modulus of $TaV_2H_{0.53}$ is 55 % greater than that of TaV_2. Figure 3.17 shows the hydrogen concentration dependence of $G(T)$ at three temperatures; 25 K, 150 K and 300 K. Included for comparison in figure 3.17 are data for $TaV_2D_{0.17}$. The shear modulus of TaV_2H_x increases rapidly and almost linearly with concentration up to $x = 0.18$, after which $G(T)$ continues to increase roughly linearly, but less rapidly, up to $x = 0.53$. Poisson's ratio is shown in figure 3.18 both as a function of temperature for the different concentrations x, and as a function of concentration at two

different temperatures. Poisson's ratio is bounded theoretically between 0 and 0.5 although for most materials ν has a value between 0.25 and 0.40. Poisson's ratio of both HfV_2 and ZrV_2 have been measured with an ultrasonic technique and both were found to have a value of 0.37 ± 0.008, at 300 K [95]. It can be seen that TaV_2 has a similar value of $\nu = 0.375 \pm 0.005$ at 300 K, which increases slowly with decreasing temperature. Typical behavior for most materials is that $\nu(T)$ increases with increasing temperature [103]. Figure 3.18(b) shows the H concentration dependence of ν at two temperatures, 25 K and 100 K. It can be observed that ν initially drops almost linearly with increasing concentration until flattening out at a value of 0.33, for $x \geq 0.34$.

The elastic moduli of $TaV_2H_{0.18}$ and $TaV_2D_{0.17}$ are shown across the entire temperature range of study in figure 3.19. The error bars indicate that the difference in the shear moduli of $TaV_2H_{0.18}$ and $TaV_2D_{0.17}$ is just outside the range of experimental error. There does not appear to be a significant isotope effect in either the magnitude or the temperature dependence of $G(T)$ except at temperatures below roughly 30 K. $G(T)$ of $TaV_2D_{0.17}$ continues to increase almost uniformly down to 3 K, whereas $G(T)$ of $TaV_2H_{0.18}$ begins to flatten out at $\approx$ 30 K, and approaches 3 K with zero slope. It was discussed in section 3.3 that this effect may be associated with the resonant tunneling of H about g-type interstitial sites within the C15 host lattice [104].

Figure 3.20 shows $G(T)$ for TaV_2H_x for $x = 0.00$, 0.06 and 0.10 on an expanded scale. The anomalous temperature dependence of $G(T)$ for TaV_2 can be clearly observed. The modulus decreases with decreasing temperature from 345 K until ~10 K where it begins to flatten out. Below 10 K $G(T)$ is almost temperature independent and

approaches 0.3 K with zero slope. (Measurements for TaV_2 were carried out down to 0.3 K; in general the measurements only extended down to 3 K.) The modulus for $TaV_2H_{0.06}$ shows a similar softening with decreasing temperature but with a somewhat weaker temperature dependence. $TaV_2H_{0.10}$ also shows a softening with decreasing temperature down to ~40 K but then a stiffening as the temperature is decreased further to 15 K. This shallow minimum in the shear modulus of $TaV_2H_{0.10}$ can be seen on the expanded scale insert in figure 20. This minimum will be a key parameter in the analysis presented below.

As figures 3.16 and 3.20 show, the temperature dependence of $G(T)$ for H(D) concentrations $x \geq 0.17$ is reversed from that of the lower concentrations. Furthermore a 'step' in $G(T)$ is clearly visible for all higher concentrations ($x \geq 0.17$) in the temperature range of 225 - 300 K. In basic terms, the data below roughly 225 K represent the unrelaxed elastic modulus while the data above 300 K represent the relaxed elastic modulus. Such steps were observed for all $x > 0.00$, but are too small to be seen in figure 3.16 for $x \leq 0.10$. Large ultrasonic loss peaks were also observed for all $x > 0.00$ in the same temperature range. A full description of the attenuation and dispersion measurements was reported in sections 3.2 and 3.3 but the significant point to remember here, is that the shift in $G(T)$ for all concentrations was described well with **Eq.** (12) and the parameters derived for the H motion from the loss measurements. The purpose now is to examine possible electronic effects on the temperature dependence of $G(T)$, unrelated to the hydrogen motion. Therefore, as the magnitude and temperature dependence of the relaxation effects on $G(T)$ were successfully accounted for, this contribution has been removed from the $G(T)$ data of figure 3.16.

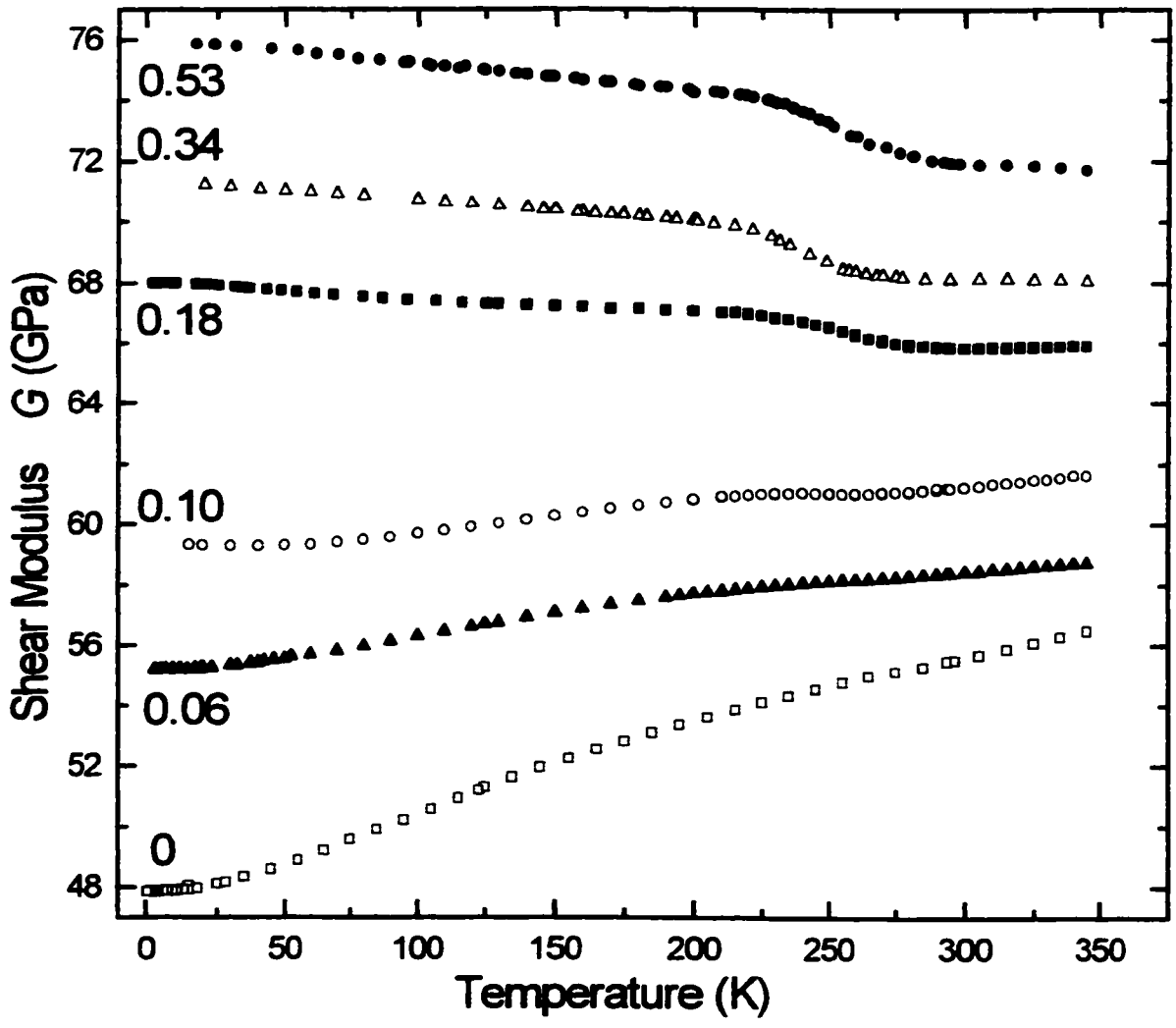

Figure 3.16: Elastic shear modulus of polycrystalline TaV_2H_x *vs.* temperature for x = 0.00, 0.06, 0.10, 0.18, 0.34 and 0.53.

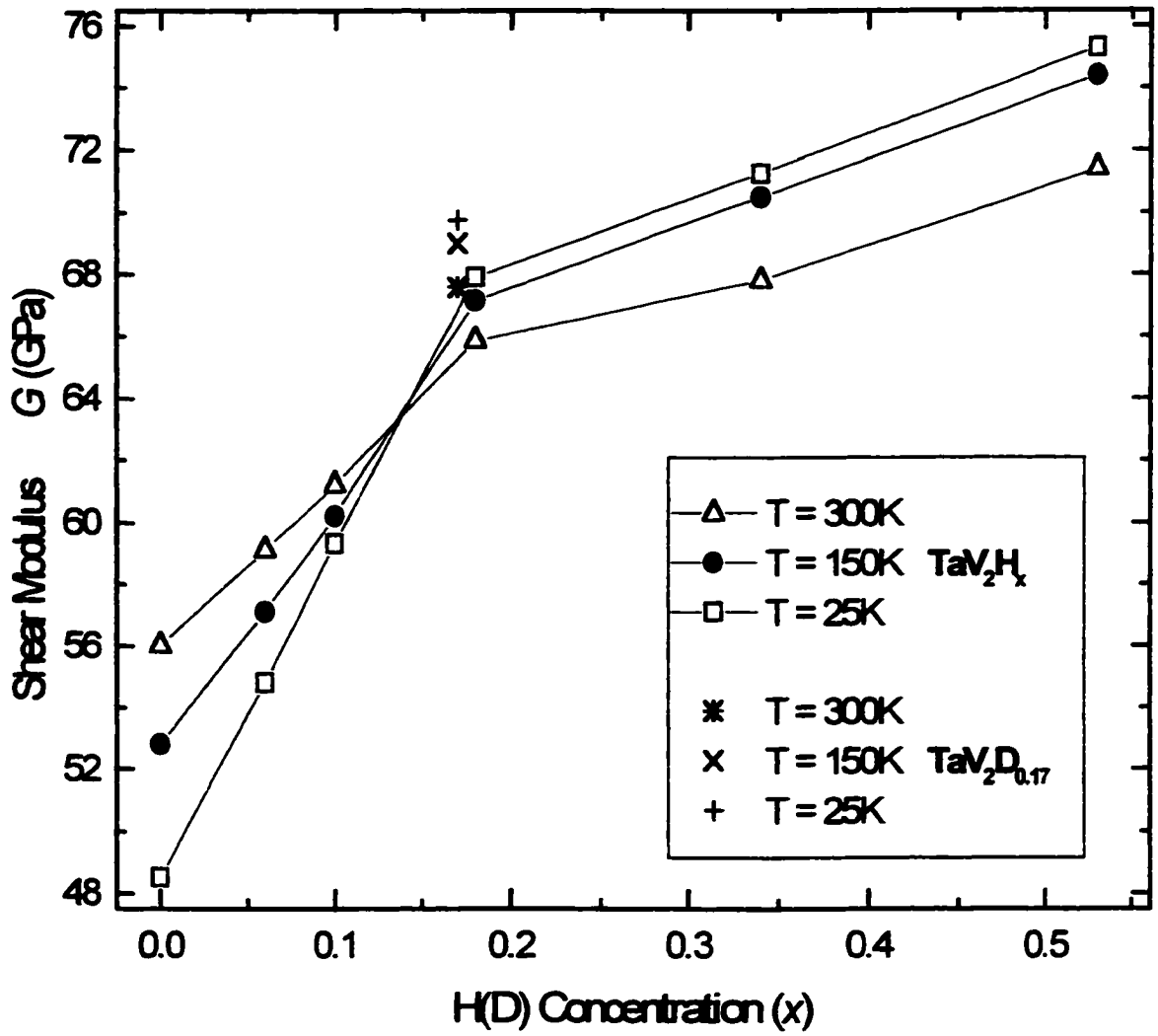

Figure 3.17: Elastic shear modulus of polycrystalline TaV_2H_x *vs.* H concentration (*x*) at 25 K, 150 K and 300 K. Data for $TaV_2D_{0.17}$ are also shown.

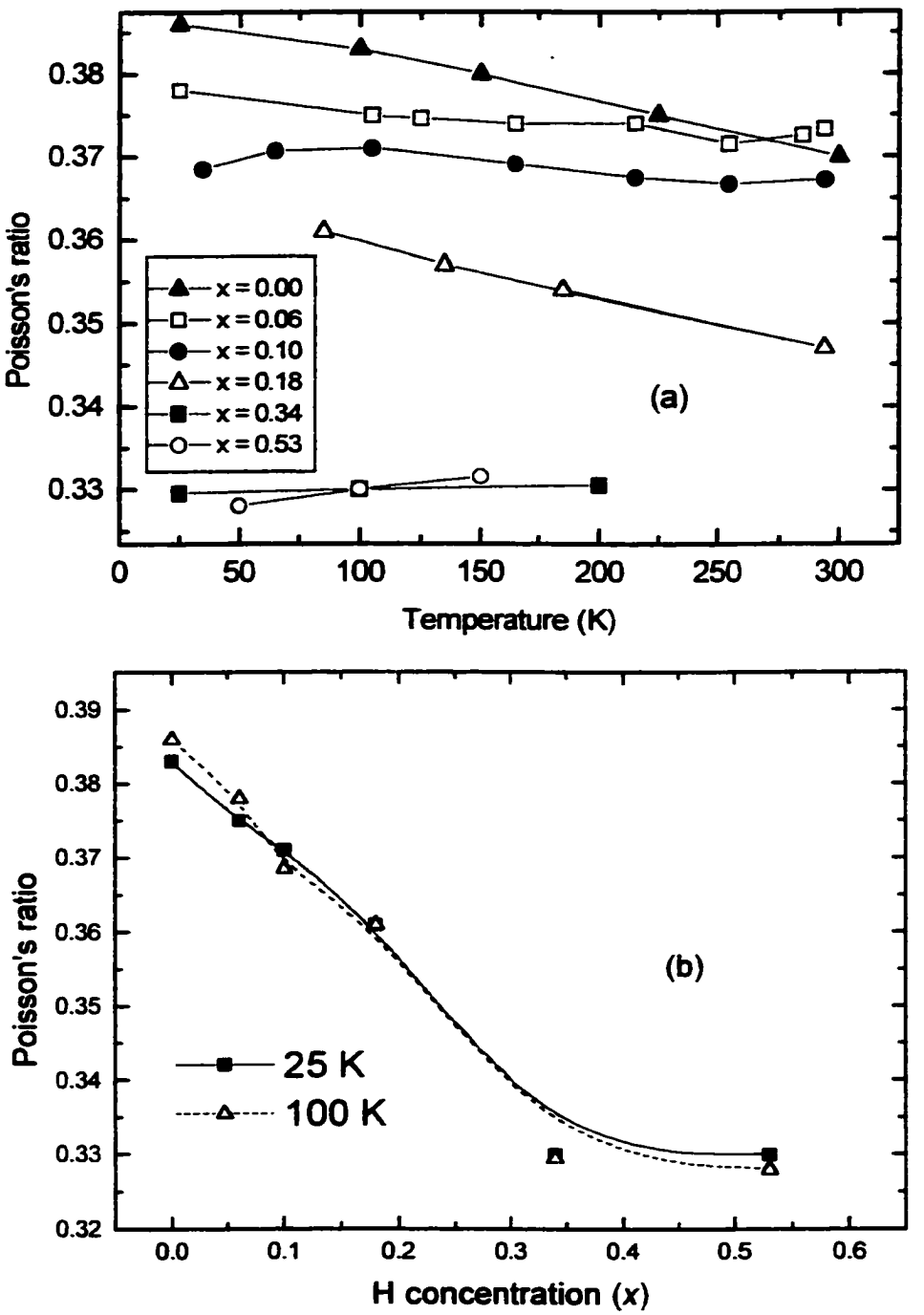

Figure 3.18: Poisson's ratio of TaV_2H_x as a function of (a) temperature and (b) H concentration (x). The solid and dashed lines are guides to the eye.

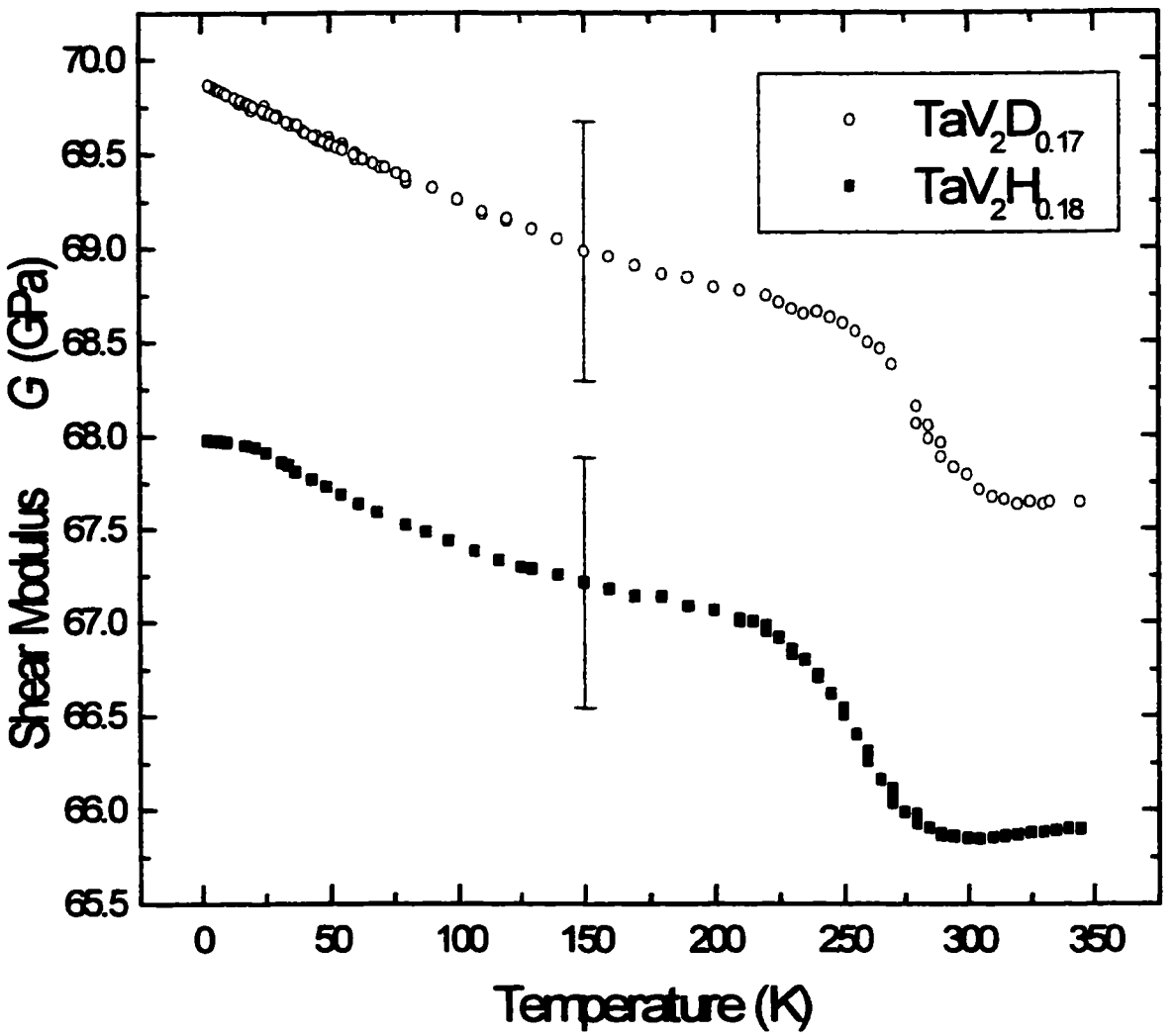

Figure 3.19: Elastic shear modulus of polycrystalline $TaV_2H_{0.18}$ and $TaV_2D_{0.17}$ *vs.* temperature. The 'steps' near 275 K are associated with the motion of hydrogen as discussed in the text.

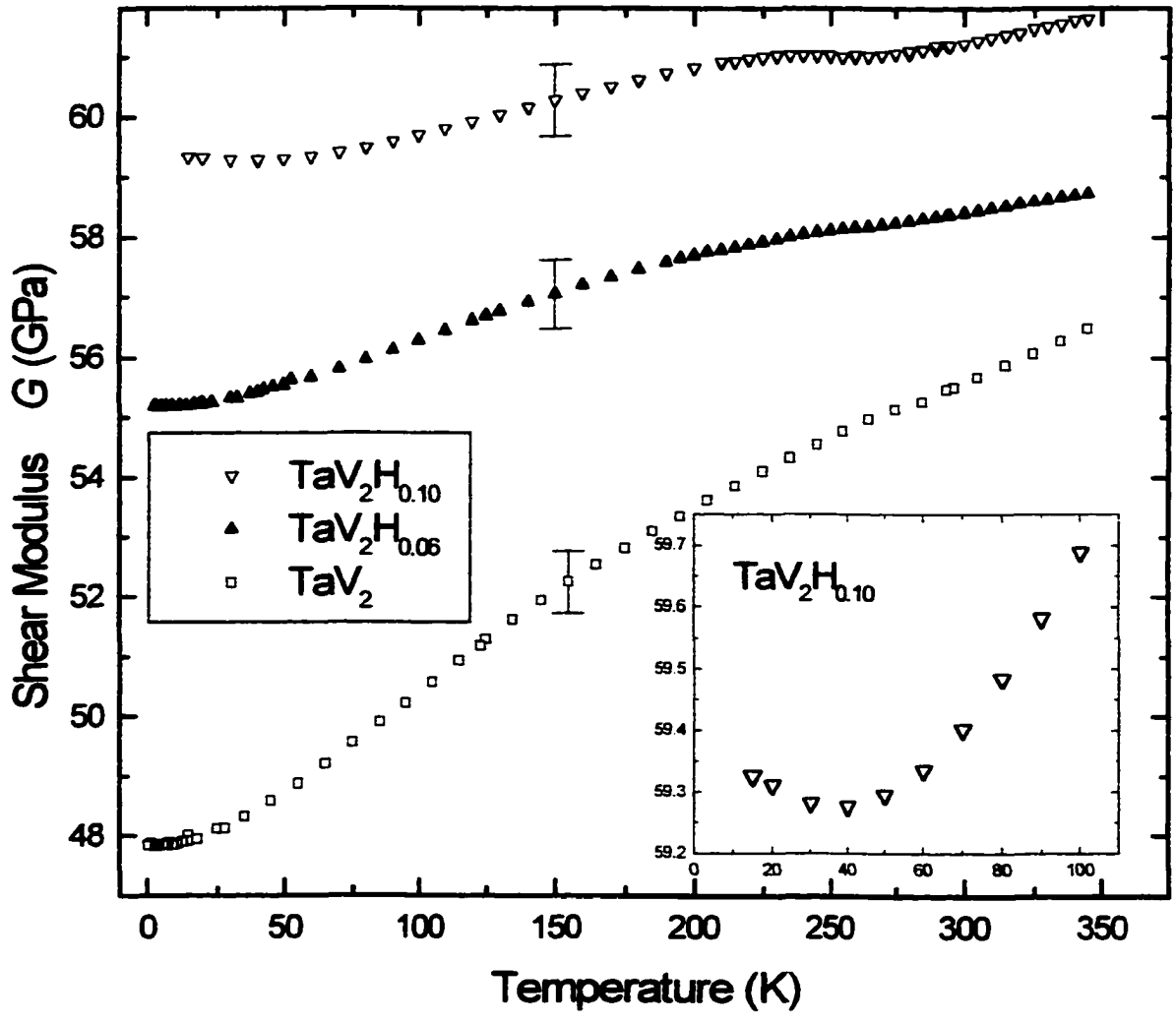

Figure 3.20: An expanded view of the data shown in figure 3.16 for $x = 0.00$, 0.06 and 0.10. The inset shows the minimum in $G(T)$ for $x = 0.10$.

The relaxation-corrected data are presented for $x \geq 0.17$ in figure 3.21(a). The underlying temperature dependence of $G(T)$ is now evident. The relaxation correction for $G(T)$ was not made for the lower concentrations where the effect was small. The relaxation-corrected modulus for $TaV_2H_{0.18}$ shows a weak minimum at roughly 300 K, although it is too shallow to be seen in figure 3.21(a). No such minimum is seen for the x = 0.34 and 0.53 concentrations or indeed for the deuterated sample, although the form of the data in figure 3.21(a) strongly suggests that the moduli are approaching minima at higher temperatures.

The results are interpreted in terms of the unusual electronic structure effects [75][88][97][98] proposed for the C15 materials which were discussed briefly in section 3.4.1. The C15 symmetry allows for doubly-degenerate electronic levels at the X-point of the IBZ with a linear dispersion relation in the vicinity of this point. The degeneracy and linear dispersion have been confirmed by band-structure calculations [75]. From symmetry considerations [98] these levels couple to a strain e_4. A key parameter in the model concerns the position of the Fermi-level with respect to this double-degeneracy point: if the Fermi level is near this point, then these bands contribute strongly to the temperature dependence of the corresponding single crystal elastic constant c_{44}. The arguments are outlined further below. The Helmholtz free energy of a system of N electrons each of energy ξ_{bk} is given by

$$F = N\xi_F - 2\sum_{bk} k_B T \ln\left[1 + \exp\frac{\xi_F - \xi_{bk}}{k_B T}\right] \qquad (17)$$

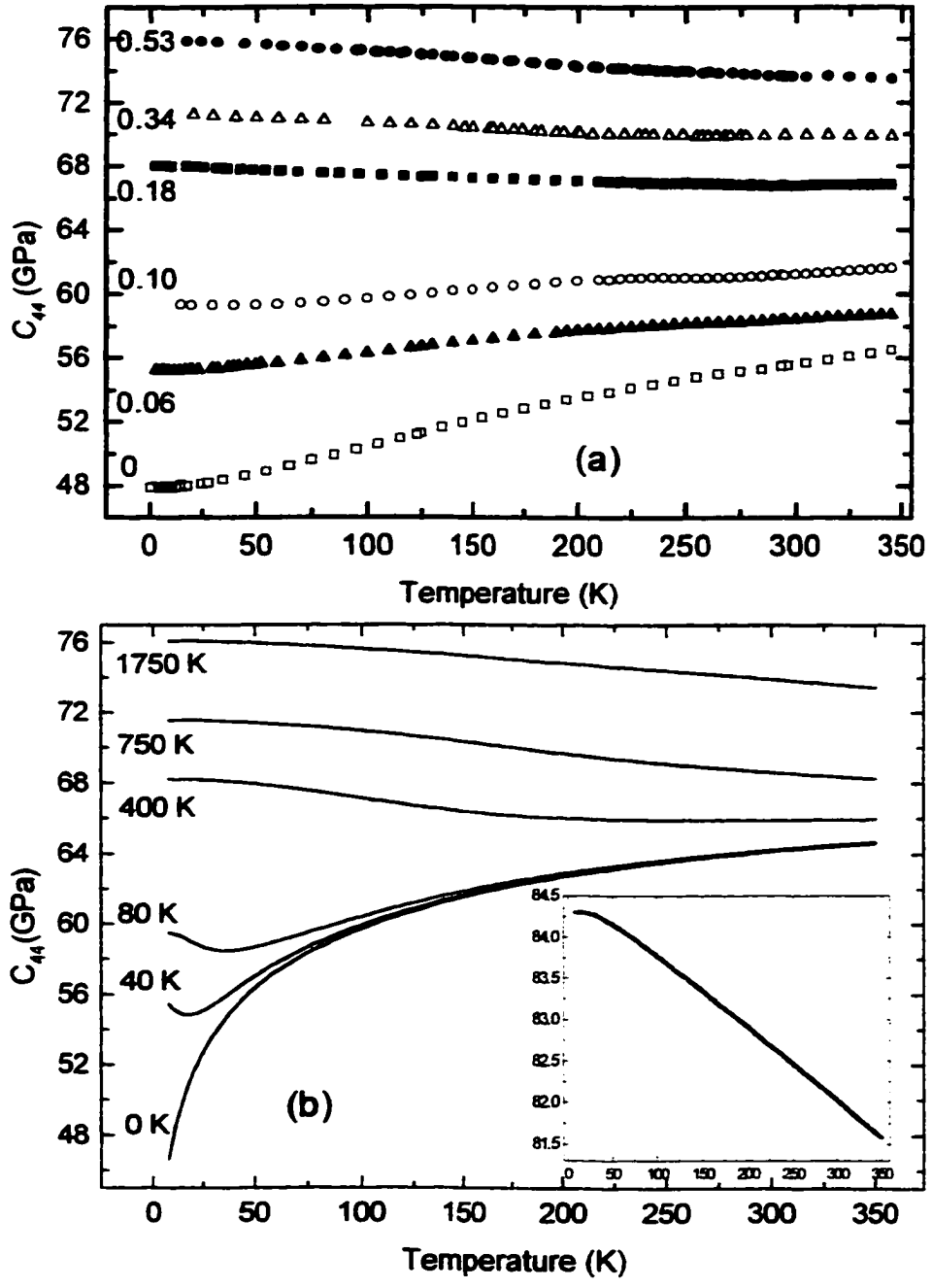

Figure 3.21: Elastic shear modulus of polycrystalline TaV_2H_x *vs.* temperature for x = 0.00, 0.06, 0.10, 0.18, 0.34 and 0.53. (a) Experimental data. The results for $x \geq 0.18$ have been corrected for the effect of the H relaxation on $G(T)$ as discussed in the text. (b) Calculated values of $G(T)$ *vs.* x. The 'background' elastic constant used in the calculation is shown in the inset. The values of the Fermi energies used in the calculation are listed in units of kelvin and were derived from figure 3.22.

where ξ_F is the Fermi energy, the sum is over all energy bands b and all k values, and the factor 2 accounts for spin. We consider only the doubly-degenerate levels in the vicinity of the X-point and express these levels as [98]

$$\xi_{1,2}(k_z) = \pm\sqrt{(sk_z)^2 + (De_4)^2} \tag{18}$$

where ξ_F, $\xi_{1,2}$, and k, the electron wave number, are measured with respect to the doubly-degenerate point, s is a proportionality constant, and D is the deformation potential. Using $c_{44}^e = \frac{\partial^2 F}{\partial e_4^2}$ gives, in the present case, the simple result

$$c_{44}^e = \pm 2D^2 \sum_k \frac{f(k_z)}{sk_z} \tag{19}$$

where $f(k_z)$ is the Fermi-Dirac distribution function. Setting $\varepsilon = sk_z$, expressing the exponentials in terms of hyperbolic functions, and converting the sum to an integral results in [61][62][75][84][98]

$$c_{44}^e \propto -D^2 \int_0^{\Omega} \frac{d\varepsilon}{\varepsilon} \left[\frac{\sinh(\varepsilon / k_B T)}{\cosh(\varepsilon / k_B T) + \cosh(\xi_F / k_B T)} \right] \tag{20}$$

where the qualitative features are not strongly dependent on the range of integration, Ω. The band-structure calculation [75] indicates that Ω = 5000 K represents a reasonable range for the linear dispersion, and this value will be used below. It can be seen from Eq. 19 that those electrons filling the lower energy band provide a negative contribution to c_{44}.

A more detailed comparison of the data to the theoretical model is now discussed. The model and data indicate that the Fermi level for the $x = 0$ case lies very near the double-degeneracy point. To be specific for the calculation, we assume that the Fermi level for this case passes through the double-degeneracy point, i.e. we take $\xi_F = 0$ for $x = 0$. Figure 3.20 shows a clear minimum in $G(T)$ for $x = 0.10$. In terms of the model, this minimum indicates that $\xi_F \approx 80$ K for $x = 0.10$. We now proceed to calculate the shear modulus $G(T)$ using

$$G(T,x) = C_{bg}(T) - K\int_0^{\Omega} \frac{d\varepsilon}{\varepsilon}\left[\frac{\sinh(\varepsilon / k_B T)}{\cosh(\varepsilon / k_B T) + \cosh(\xi_F / k_B T)}\right] \qquad (21)$$

where $C_{bg}(T)$ is a background term representing all the other contributions to the elastic constants such as the ion-core, phonon and other electronic contributions. The constant K is proportional to D^2, but also includes other factors which are difficult to quantify. There is a phase-space volume contribution [98] and a factor to account for the fact that the model is for the single-crystal elastic constant c_{44}. It should be remembered that the measurements are for the aggregate elastic constant $G = C_{44}$ which will have contributions from the other single-crystal elastic constants. K will be found by fitting the data. First, we calculate $G(T)$ as a function of the Fermi energy at 10 K to determine fitting constants. We choose this temperature because the effects of the electronic structure model are largest at low temperatures. Other effects not associated with the model will be relatively less important and more reliable fitting constants may be found. At this temperature we take $C_{bg} = C_o$ To determine the two constants C_o and K we set two conditions: 1, for $x = 0$ we

take $\xi_F = 0$ and $G(10\text{ K}) = 47.8$ GPa; 2, for $x = 0.10$ we take $\xi_F = 80$ K and $G(10\text{ K}) = 59.5$ GPa. These Fermi energies were chosen because $G(T)$ for $x = 0$ increases with temperature throughout the temperature range investigated and $G(T)$ for $x = 0.10$ showed a clear minimum at about 40 K. The values of G are the experimental values at 10 K for these two x values. Putting these two conditions into **Eq.** 21 gives $C_o = 81.7$ GPa and $K = 5.34$ GPa. The result of the calculation of G *vs.* ξ_F with these two constants is shown in figure 3.22. Using figure 3.22 we now determine the Fermi energies for the other four x values by projecting the $G(10\text{ K})$ values for each concentration onto the ξ_F axis. This process is indicated by the dashed lines in figure 3.22.

With C_o, K and the Fermi energies determined, we now use **Eq.** 21 to calculate the full temperature and x dependence of G. To estimate the temperature dependence of the background term we use the convenient Varshni expression [103]

$$C_{bg}(T) = C_o - \frac{s}{\exp\frac{t}{T} - 1} \tag{22}$$

with $s = 0.73$ GPa and $t = 100$ K. These values of s and t were estimated from $G(T = 350\text{ K}, x = 0.53)$. The resulting temperature dependence of C_{bg} is comparable to that found experimentally [61] for $ZrCr_2$, a C15 Laves-phase compound which does not show the unusual temperature dependence of TaV_2. It should be emphasized that the conclusions would not be changed significantly if the temperature dependence of C_{bg} were neglected altogether. The results of the calculation of $G(x, T)$ are shown in figure 3.21(b). The background elastic constant is indicated in the inset of figure 3.21(b). Comparing figure

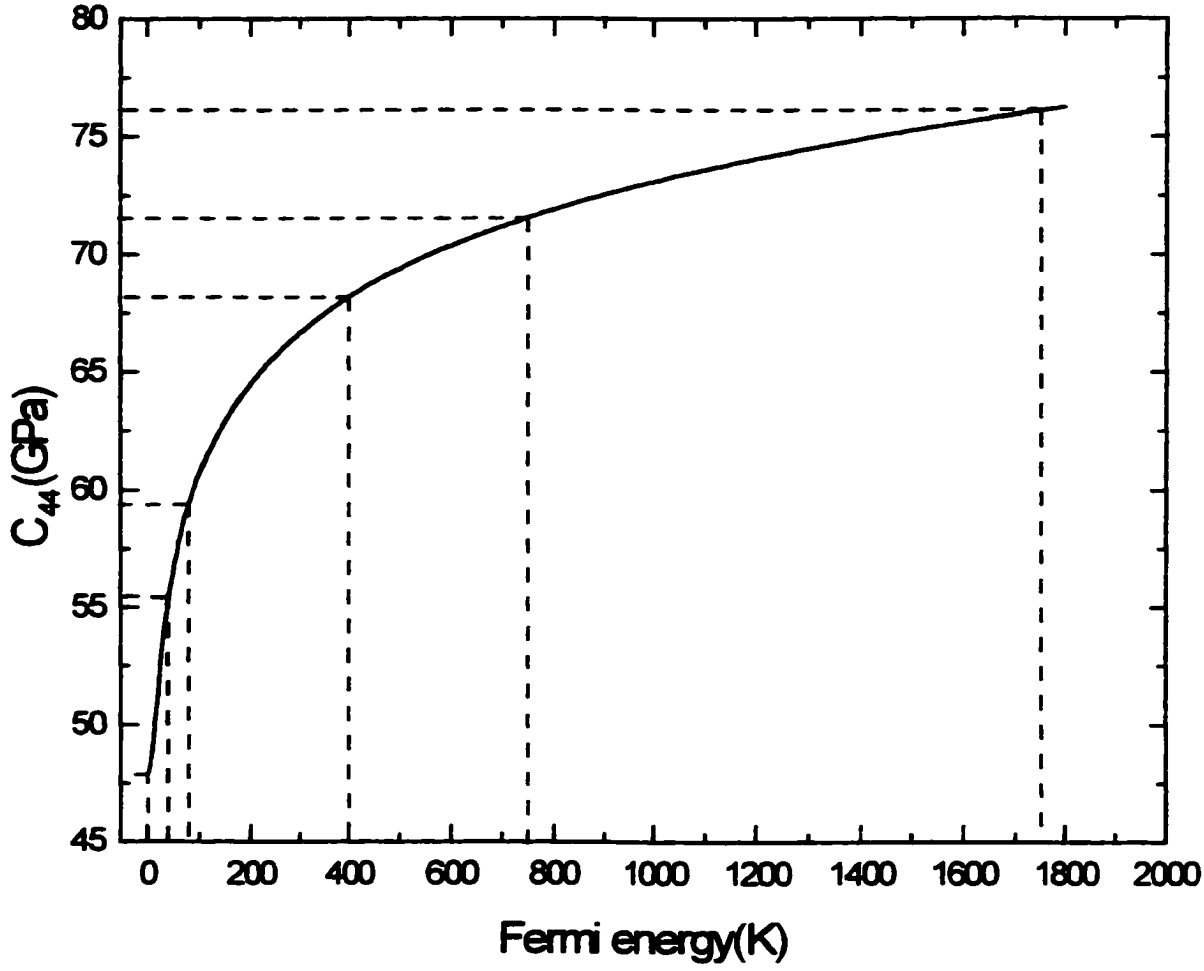

Figure 3.22: Calculated values of the elastic shear modulus *vs.* Fermi energy at 10 K. The constants C_o and K used in the calculation are listed in the text. The curve was constrained to pass through the two points (47.8 GPa, 0 K) and (59.5 GPa, 80 K) as discussed in the text. The dashed lines indicate the projection of the experimental values of the 10 K elastic constants onto the Fermi energy axis to determine ξ_F for $x = 0.06$, 0.18, 0.34 and 0.53. These values of ξ_F were used for the computation of figure 3.21(b).

3.21(a) and (b), it can be seen that this simple model accounts for the major features of the data. There are a number of possible contributions to the elastic constants which are not taken into account in the present analysis and which may contribute to the differences between the measured and computed values of $G(T)$. Because the lattice expands with the addition of hydrogen, the background elastic constant may depend on hydrogen concentration. We have used the same C_{bg} for all x. In terms of the model used, the constant D could be k-dependent. In addition, there may be other electron and phonon contributions which could be x-dependent, and which are not included in the model. There are basically four parameters in the model C_o, K, and the values of the Fermi energies for the two concentrations 0.00 and 0.10. The parameters s and t have only a minor effect.

We now turn to a discussion of the shift of the Fermi level with the addition of hydrogen. The general idea is that each hydrogen atom will contribute a fraction of an electron to the conduction band. These electrons will raise the Fermi level. An important parameter is the density of states at the Fermi level, $N(\xi_F)$. A large $N(\xi_F)$ will mean a small shift and vice-versa. Figure 3.23 gives the shift of ξ_F *vs.* x as determined from figure 3.22 for the six x values of the present work (solid points in the plot). The fact that the plot turns upward as a function of x indicates that $N(\xi_F)$ decreases with increasing x. Fortunately, there is experimental information about $N(\xi_F)$ for TaV_2H_x from nuclear magnetic resonance (NMR) experiments [105]. The NMR results indeed show that $N(\xi_F)$ initially decreases with the addition of hydrogen, levels off above $x = 0.56$ and passes through a minimum at $x = 0.8$

The comparison can be made more quantitative. The shift of the Fermi energy $\Delta\xi_F$

is related to the increase in hydrogen concentration Δx by $N(\xi_F,x)\Delta\xi_F = f\,\Delta x$ where f is the fraction of an electron each added hydrogen atom contributes at the Fermi level. The Fermi energy at x relative to the value at zero hydrogen concentration is then given by

$$\xi_F = \int_0^x \frac{f dx'}{N(\xi_F,x')} \,. \tag{23}$$

The NMR results are available for three x values - 0.00, 0.22 and 0.56 - over the range of the present experiments. Considering just these three points, $N(\xi_F)$ appears to decrease linearly and can be represented by $N(\xi_F,x) = 6.54 - 9.06x$ /(ev TaV_2 unit) where a factor of two has been included for spin. Using this expression for $N(\xi_F)$ in **Eq.** 23 gives $\xi_F = -0.11 f \ln(1 - 1.38x)$ eV. This expression is represented by the solid line in figure 3.23 for $f = 1$. It can be seen that this expression fits the data remarkably well. This implies that each hydrogen atom contributes one electron at the Fermi level. The value $f \approx 1$ is expected for a dilute hydrogen-metal system [100] where hydrogen-hydrogen interactions can be neglected. In the present case, even at $x = 0.53$ only about 4% of g sites are occupied, so the system may be considered dilute. In addition, the ultrasonic attenuation measurements reported in section 3.2.3 showed that the loss peak due to hydrogen motion is linear in the hydrogen concentration (Snoek effect) which is additional support for the relative unimportance of hydrogen-hydrogen interactions. The shifts in the Fermi level implied by the elastic constant results are in such good agreement with the NMR experiments on $N(\xi_F)$ that this provides strong support for the model of electronic-

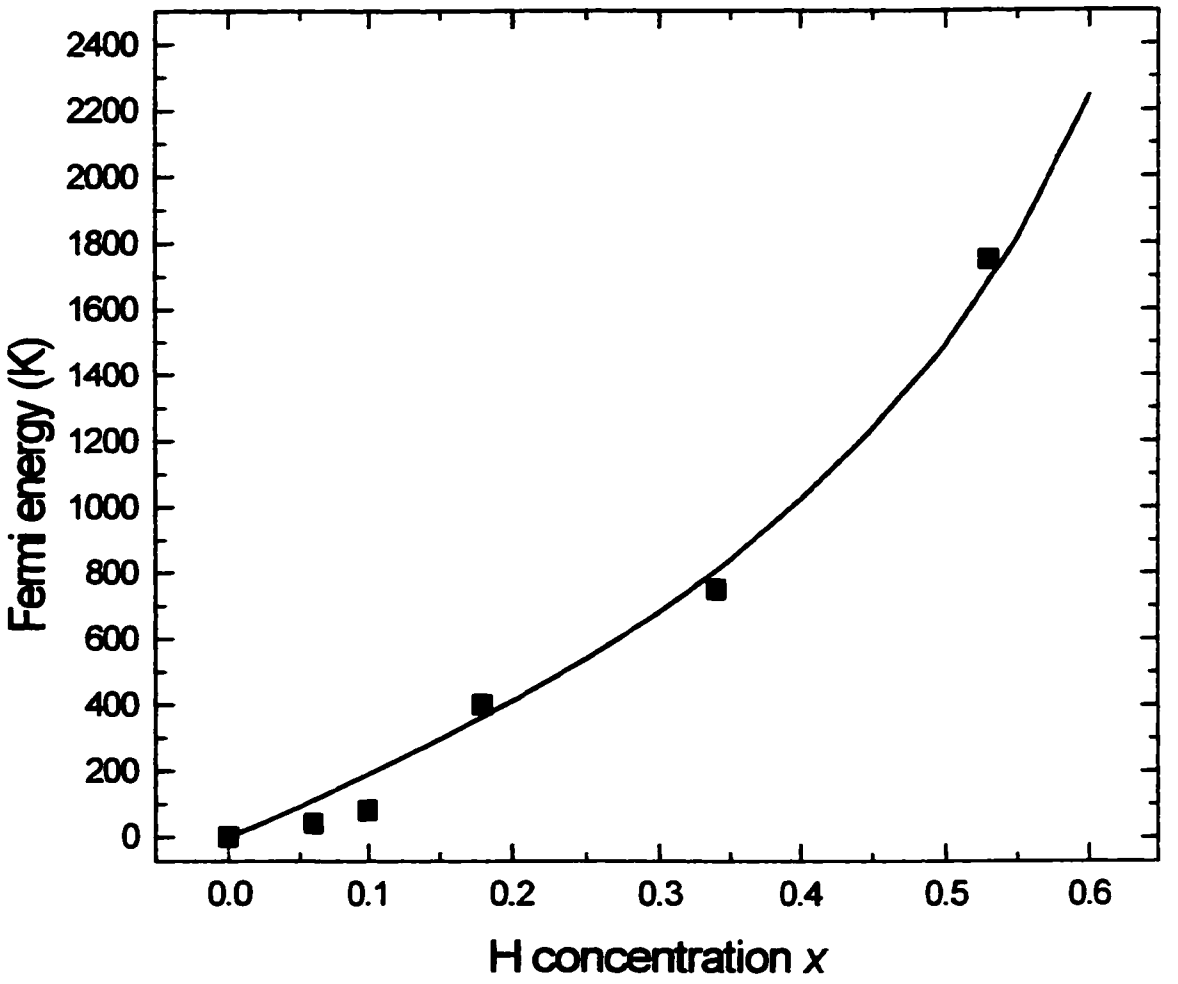

Figure 3.23: Shift of the Fermi energy *vs.* H concentration (x). The points were determined from the elastic constant measurements. The solid line was computed from density of states results with the assumption that each H atom contributes one electron at the Fermi level.

structure induced changes to the elastic shear modulus. The discrepancy between elastic-constant derived shifts and those computed from the DOS in the range $0 \leq x \leq 0.1$ could be accounted for by a higher DOS in this range; the NMR measurements did not provide details about $N(\xi_F)$ in this range and the linear interpolation may not represent the actual situation.

Now the question of lattice instability in C15 Laves-phases and the relationship to the observed anomalous elastic properties will be addressed. There is evidence from a series of experimental studies that a structural phase transition occurs at roughly 100 K in cubic HfV_2 and ZrV_2 [95][97][106][107][108][109]. The first-order structural phase transition appears to be preceded by an electronic transition at 125 K and 160 K for HfV_2 and ZrV_2 respectively [95]. It is within this temperature range at which unusual effects were observed for Poisson's ratio, $G(T)$, $E(T)$ and $B(T)$ in these systems. The evidence suggests that the low-temperature phase of HfV_2 is either tetragonal or orthorhombic and that of ZrV_2 is either rhombohedral [110] or orthorhombic [88]. The symmetry of the low-temperature phases has not been determined conclusively and appears to be sensitive to the impurity content in the material [111].

The electronic model described above has been used to account for the anomalous elastic properties in the HfV_2 and ZrV_2 systems. Izyumov *et al.* [98] suggested that the total softening of c_{44} due to the cancellation of the positive normal ionic contribution (c_{44}^{i}) by the negative electronic contribution (c_{44}^{e}) was directly responsible for the lattice instability. It is known that the anomalies in specific heat and resistivity measurements observed for HfV_2 can be removed by the addition of small quantities of Nb (3 - 5 %),

stabilizing the cubic high-temperature phase [97]. It was also found that HfV_2 doped with 15 at. % Nb did *not* show a specific heat anomaly but *did* exhibit similar unusual elastic properties. This observation provided initial evidence for the arguments made by Chu *et al.* [97] that the softening of c_{44}^{e} may not be the underlying mechanism for the lattice instability. Chu *et al.* used first principle calculations to determine the total energy and electronic structure of C15 MV_2 (M = Ta, Hf and Zr) and estimated that the Fermi level of HfV_2 and ZrV_2 lies roughly 800 K above the double-degeneracy point. For this value of the Fermi level the model implies that the c_{44}^{e} contribution would stiffen with decreasing temperature below ≈350 K. Therefore, it was argued that the low-temperature phase transformation could not be caused by the cancellation of c_{44}^{l} by c_{44}^{e}. Instead it was proposed that the lattice instability in HfV_2 and ZrV_2 was related to the high value of the density of states (DOS) at the Fermi level ($N(\xi_F)$) and to the geometry of the Fermi surface [97].

A number of theoretical studies have confirmed the presence of a large, narrow peak in the DOS of HfV_2 and ZrV_2 and that the Fermi level lies on this peak [96][97][112]. A large $N(\xi_F)$ and a sharp peak in the DOS can result in a strong electron-phonon coupling. The physical effect of this coupling is dependent on the specific geometry of the Fermi surface. In the case of HfV_2 and ZrV_2 it was argued that Fermi surface nesting results in an incommensurate electronic charge density wave along the <100> direction. It was argued that the combination of the high electron-phonon coupling and the charge-density wave induced by Fermi surface nesting could cause the displacement of atoms at lower temperatures, leading to phonon softening, lattice instability and the phase transition [97].

Similar experimental studies [97][109] performed on TaV_2 have not shown any evidence for a phase transition: TaV_2 maintains the cubic C15 structure down to at least 4 K. The data reported here for $G(T)$ and Poisson's ratio show no discontinuities or inflection points throughout the temperature range studied. The lack of a phase transition in TaV_2 was rationalized by Chu *et al.* [97] who showed that TaV_2, having one more *d* electron per formula unit, has an increased Fermi energy resulting in both a reduction in $N(\xi_F)$ (as the Fermi level shifts away from DOS peak) and the disappearance of the Fermi surface nesting. As in the Hf-Nb-V system for > 5% Nb, the TaV_2 alloy displays anomalous elastic properties but without an associated structural phase transition [97].

However, as the electronic model implies, the results for C_{44} indicate that the Fermi level of TaV_2 appears to be very close to the double-degeneracy level at the *X*-point of the IBZ in contradiction to the band structure calculations [97]. It is interesting to note that if the calculated Fermi levels of HfV_2, ZrV_2 and TaV_2 are systematically lowered so that the ξ_F of TaV_2 is roughly 0 K above the *X*-point, then the ξ_F of HfV_2 and ZrV_2 would lie ~200 K below the *X*-point. For this value of ξ_F the electronic model would predict a softening of c_{44} for HfV_2 and ZrV_2 down to ~100 K, as observed. It seems reasonable that the negative electronic contribution to c_{44} may persist below room temperature and contribute to the lattice instability of HfV_2 and ZrV_2.

3.4.4 Conclusions

Measurements of the elastic shear modulus of polycrystalline $TaV_2H(D)_x$ over a temperature range of 3 - 345 K have revealed several striking features. Both the

temperature dependence and the magnitude of the shear modulus are highly dependent on the hydrogen concentration. At 20 K $G(T)$ for $TaV_2H_{0.53}$ is 55 % stiffer than that of TaV_2. For H concentrations $x \leq 0.10$, $G(T)$ shows anomalous stiffening with increasing temperature almost across the entire temperature range of study. $TaV_2H_{0.10}$ displays a minimum in $G(T)$ at roughly 40 K. For H concentrations $x \geq 0.18$ the temperature dependence of $G(T)$ is reversed compared to that of the lower concentrations, and exhibit softening with increasing temperature. Comparison of the results for $TaV_2H_{0.18}$ and $TaV_2D_{0.17}$ indicates that there is not a strong isotope effect on $G(T)$.

The results are in agreement with a model detailing electronic contributions to the single-crystal elastic constant c_{44}. The symmetry of the C15 structure results in doubly-degenerate electronic energy levels at the X point of the Brillouin zone. These levels couple to an e_4 strain with resulting effects on the single-crystal elastic constant c_{44} which subsequently modifies the shear modulus $G(T)$ of the polycrystalline samples. Hydrogen donates electrons to the conduction band, shifting the Fermi level above the double-degeneracy point. As a result, the electronic contributions to c_{44} are strongly affected. The shift of the Fermi energy as a function of the hydrogen concentration x determined from the elastic constant measurements is in remarkable agreement with the shift predicted from electronic density of states data available from nuclear magnetic resonance experiments. The present results indicate that each hydrogen atom contributes approximately one electron at the Fermi level.

3.5 Concluding Remarks

The $TaV_2H(D)_x$ system proved to be both well suited to ultrasonic measurements and to provide a number of interesting features in both the loss and modulus results. The $TaV_2H(D)_x$ compounds provided an excellent opportunity to study a 'clean' metal-hydrogen system, in the sense that there were no structural phase changes or hydrogen ordering effects down to at least 4 K for the H concentrations studied.

Three main studies of the $TaV_2H(D)_x$ system were conducted, concerning; the long-range diffusion of H(D), isotope effects on the local motion of H(D), and strong hydrogen-related effects on the shear elastic constant: the conclusions of these studies are reported in sections 3.2.4, 3.3.4 and 3.4.4 respectively. It would clearly be beneficial to perform these same experiments on a single crystal samples. This would allow for absolute confirmation that it is single crystal elastic constant c_{44} which is responsible for the electronic structure induced effects on the aggregate shear modulus. Also, by looking for mode-dependent effects on the ultrasonic loss, information concerning the geometry of the H(D) hopping mechanisms can sometimes be inferred.

The loss and modulus measurements were somewhat challenging as the ultrasonic loss in this system was rather high in the temperature range of 200 - 300 K, particularly for H concentrations ≥ 0.18. This made mode excitation, detection and identification difficult. Accurate preparation of RP samples also proved rather problematic for higher H concentrations due to the increasing brittleness of the hydrides, though this is not an unusual problem for materials of this kind. These experiments on $TaV_2H(D)_x$ have demonstrated the capabilities of RUS for making high-quality measurements of both the

ultrasonic loss and the elastic moduli. For the first time, RUS has been successfully applied to an intermetallic metal-hydride: the results would have been difficult to obtain with conventional ultrasonic techniques due to the limited sample sizes available.

REFERENCES

[1] H. Davy, *Philosophical Transactions of the Royal Society*, **107**, 77 (1817).

[2] F. Cuevas, J.-M. Joubert, M. Latroche and A. Perheron-Guégan, Appl. Phys. A **72**, 225 (2001).

[3] Z. S. Wronski, *International Materials Review* **46** (1), 1 (2001).

[4] J. Van Vucht, F. A. Kuijpers, H. Bruning: Philips Res. Rep. **25**, 133 (1970).

[5] J. N. Huiberts, R. Griessen, J. H. Rector, R. J. Wijngaarden, J. P. Dekker, D. G. de Groot, and N. J. Koeman, Nature (London) **380**, 231 (1996).

[6] R. Griessen, J. N. Huiberts, M. Kremers, A. T. M. van Gogh, N. J. Koeman, J. P. Dekker, and P. H. L. Notten, J. Alloys Compd. **253**, 44 (1997).

[7] Y. Fukai, *The Metal-Hydrogen System* (Springer-Verlag, 1993).

[8] G Alefeld and J Völkl, editors. *Hydrogen in Metals 1* (Springer-Verlag, 1978).

[9] G Alefeld and J Völkl, editors. *Hydrogen in Metals II* (Springer-Verlag, 1978).

[10] L. Schlapbach, editor. *Hydrogen in Intermetallic Compounds I* (Springer-Verlag, 1988).

[11] L. Schlapbach, editor. *Hydrogen in Intermetallic Compounds II* (Springer-Verlag, 1992).

[12] A. S. Nowick and B. S Berry, *Anelastic Relaxation in Crystalline Solids* (Academic Press, 1972).

[13] R. G. Leisure, in *Resonant Ultrasound Spectroscopy*, ed. by A. Migliori and J. L. Sarroa (J. Wiley and Sons, New York, 1997) Ch. 9.

[14] A. V. Granato, K. L. Hultman and K.-F. Huang, J. Phys. (Paris) **46**, C10 (1985).

[15] J. Jackle, L. Piche, W. Arnold and S. Hunklinger, J. Non-Crystal. Solids **20**, 365 (1976).

[16] K. W. Kehr, in *Hydrogen in Metals 1*, ed G Alefeld and J Völkl (Berlin: Springer, 1978) p. 197.

[17] J. Völkl and G. Alefeld, *Hydrogen in Metals 1*, ed G Alefeld and J Völkl (Berlin: Springer, 1978) p. 321.

[18] D. Richter, R. Hempelmann and R. C. Bowman, in *Hydrogen in Intermetallic Compounds II* ed L Schlapbach (Berlin: Springer, 1992) p. 97.

[19] J. D. Livingston, *High Temperature Silicides and Refractory Alloys*, Materials Research Society Symposium Proceedings **322** ed C L Bryant, J J Petrovic, B P Bewlay, A K Vasudevan and H A Lipsett (Pittsburgh, Pennsylvania: Materials Research Society, 1992) p. 395.

[20] J. Shinar, D. Davidov and D. Shaltiel, Phys. Rev. B **30**, 6331 (1984).

[21] R. Hempelmann, D. Richter, O. Hartmann, E. Karlsson and R. Wäppling, J. Chem. Phys **90**, 1935 (1989).

[22] C. U. Maier and H. Kronmüller, J. Phys.: Conden. Matter **4**, 4409 (1992).

[23] H. Reule, M. Hirscher and H. Kronmüller, Phil. Mag B **76**, 929 (1997).

[24] M. Kemali, C. E. Buckley, D. K. Ross, S. M. Bennington and S. F. Parker, Physica B **234-236**, 906 (1997).

[25] H. R. Sinning, Phys. Stat. Sol (a) **131**, 445 (1992).

[26] A. V. Skripov, J. C. Cook, C. Karmonik and V. N. Kozhanov, Phys. Rev. B **60**, 7238 (1999).

[27] K. Foster, R. G. Leisure and A. V. Skripov, J. Phys.: Conden. Matter **11** 799 (1999).

[28] G. Majer, W. Renz, A. Seeger, R. G. Barnes, J. Shinar and A. V. Skripov, J. Alloys Compounds **231**, 220 (1995).

[29] A. V. Skripov, M. Yu. Belyaev and A. P. Stepanov, Solid State Commun. **78**, 909 (1991).

[30] A. V. Skripov and M. Yu. Belyaev, J. Phys.: Condens. Matter **5**, 4767 (1993).

[31] D. Fruchart, A. Rousault, C. B. Shoemaker and D. P. Shoemaker, J. Less-Common Met. **73**, 363 (1980).

[32] V. A. Yartys, V. V. Burnasheva, N. V. Fadeeva, S. P. Solov'ev and K. N. Somenenko, Dokl. Akad. Nauk SSSR **225**, 582 (1980).

[33] Skripov A V, Pionke M, Randl O and Hemplemann R 1999 *J. Phys.: Condens. Matter* **11** 1489

[34] R. C. Bowman , B. D. Craft, A. Attalla and J. R. Johnson, Int. J. Hydrogen Energy **8**, 801 (1983).

[35] A. V. Skripov, S. V. Rychkova, M. Yu. Belyaev and A. P. Stepanov, J. Phys.: Condens. Matter **2**, 7195 (1990).

[36] A. V. Skripov, M. Yu. Belyaev, S. V. Rychkova and A. P. Stepanov, J. Phys.: Condens. Matter **3**, 6277 (1991).

[37] A. V. Skripov, M. Yu. Belyaev, S. V. Rychkova and A. P. Stepanov, J. Phys.: Condens. *Matter* **1**, 2121 (1989).

[38] A. V. Skripov, J. C. Cook, C. Karmonik and R. Hemplemann, J. Phys.: Condens. Matter **8**, L319 (1996).

[39] A. V. Skripov, J. C. Cook, D. S. Sibirtsev, C. Karmonik and R. Hemplemann, J. Phys.: Condens. Matter **10**, 1787 (1998).

[40] J. F. Lynch, J. Phys. Chem. Solids **42**, 411 (1981).

[41] V. A. Somenkov and A. V. Irodova, J. Less-Common Met. **101**, 481 (1984).

[42] P. Fischer, F. Fuath, A. V.Skripov, A. A. Podlesnyak, L. N. Padurets, A. L. Shilov and B. Ouladdif, J. Alloys Compounds **253/254**, 282 (1997).

[43] D. B Poker, G. G. Setser, A. V. Granato and H. K. Birnbaum, Phys. Rev. B **29**, 622 (1984).

[44] C. Cannelli, R. Cantelli and F. Cordero, Phys Rev. B **34**, 7721 (1986).

[45] B. S. Berry and W. C. Pritchett, Scripta Metall. Mater. **15**, 637 (1981).

[46] H. R. Sinning, Phys. Stat. Sol. **140**, 97 (1993).

[47] K. Foster, R. G. Leisure, J. B. Shaklee, J. Y. Kim and K. F. Kelton, Phys. Rev. B **61**, 241 (2000).

[48] J. Buchholz, J. Völkl and G. Alefeld, Phys. Rev. Lett. **30**, 318 (1973).

[49] R. R. Arons, J. Borman, M. Wizzenbeek, C. Tyn, G. Leferink and G. De Vries, Acta Metall. **15**, 144 (1967).

[50] F. M. Mazzolai, P. G. Bordoni and F. A. Lewis, J. Phys. F **11**, 337 (1981).

[51] Y. Cho and R. G. Leisure, Phys. Rev. B **38** 5748 (1988).

[52] P. Vajda, J. N. Daou, P. Moser and P. Rémy, J. Phys.: Condens. Matter **2**, 3885 (1990).

[53] R. G. Leisure, R. B. Schwarz, A. Migliori, D. R. Torgeson and I. Svare, Phys. Rev. B **48**, 893 (1993).

[54] H. Wipf and B. Kappesser, J. Phys.: Condens. Matter **8**, 7233 (1996).

[55] L. A. Nygren and R. G. Leisure, Phys. Rev. B **39**, 7611 (1989).

[56] B. Sobha, B. Coluzzi, F. M. Mazzolai, A. P. Craft and T. B. Flanagan, J. Phys.: Condens. Matter **4**, 3377 (1992).

[57] H.-R. Sinning, Phys. Rev. B **46**, 5989 (1992).

[58] H.-R. Sinning, Phys. Rev. Lett. **85**, 3201 (2000).

[59] W. Renz, G. Majer, A. V. Skripov and A. Seeger, J. Phys.: Condens. Matter **6**, 6367 (1994).

[60] W. Renz, G. Majer and A. V. Skripov, J. Alloys Compounds **224**, 127 (1995).

[61] K. Foster, J. E. Hightower, R. G. Leisure and A. V. Skripov, Phil. Mag B **80**, 1667 (2000).

[62] R. G. Leisure, K. Foster, J. E. Hightower, A. Ode and A. V. Skripov, J. Alloys Compound. (to appear 2001).

[63] D. Emin, M. I. Baskes and W. D. Wilson, Z. Phys. Chem., NF **114**, 231 (1979).

[64] R. G. Leisure, R. B. Schwarz, A. Migliori, D. R. Torgeson, I. Svare and I. S. Anderson, Phys. Rev. B **48**, 887 (1993).

[65] J. J. Balbach, M. S. Conradi, R. G. Barnes, D. S. Sibirtsev and A. V. Skripov, Phys. Rev. B **60**, 966 (1999).

[66] A. V. Skripov, J. C. Cook, T. J. Udovic and V. N. Kozhanov, Phys. Rev. B **62**, 14099 (2000).

[67] J. F. Fernandez, M. Kemali and D. K. Ross, J. Alloys Compounds **253-254**, 248 (1997).

[68] Yu. Kagan, J. Low Temp. Phys. **87**, 525 (1992).

[69] Yu. Kagan and N.V. Prokofev, Sov. Phys. JEPT **70**, 957 (1990).

[70] J. A. Garber and A. V. Granatao, Phys. Rev. B **11**, 3990 (1975).

[71] G. A. Alers, in *Physical Acoustics Vol. IV Part A*, edited by W. P. Mason (Academic Press, New York, 1966).

[72] W. L. Rehwald, Adv. Phys. **22**, 721 (1973).

[73] F. Willis and R. G. Leisure, Phys. Rev. B **54**, 9077 (1996).

[74] C. Weinmann and S. Steinemann, Sol. State. Commun. **15**, 281 (1974).

[75] F. Chu, M. Šob, R. Siegl, T. E. Mitchell, D. P. Pope and S. P. Chen, Phil. Mag. B **70**, 881 (1994).

[76] H. Anton, and P. C. Schmidt, Intermetallics **5**, 449 (1997).

[77] S. Hong and C. L. Fu, Intermetallics **7**, 5 (1999).

[78] G. W. Shannette and J. F. Smith, J. Appl. Phys. **40** (1), 79 (1969).

[79] R. J. Schlitz and J. F. Smith, J. Appl. Phys. **45** (11), 4681 (1974).

[80] R. L. Fleischer, R. S. Gilmore and R. J. Zabala, Acta metall. **37** (10), 2801 (1989).

[81] F. Willis, R.G. Leisure and I. Jacob, Phys. Rev. B **50**, 13 792 (1994).

[82] S. Hong, C. L. Fu and M. H. Yoo, Intermetallics **7**, 1169 (1999).

[83] B. Wolf, C. Hinkel, S. Holtmeier, D. Wichert, I. Kouroudis, G. Bruls, B. Luthi, M. Hedo, Y. Inada, E. Yamamoto, Y. Haga and Y. Onuki, J. Low Temperature Phys. **107**, 421 (1997).

[84] F. Chu, M. Lei, A. Migliori, S.P. Chen and T. E. Mitchell, Phil. Mag. B. **70**, 867 (1994).

[85] T. E. Mitchell, R. G. Castro, J. J. Petrovic, S. A. Maloy, O. Unal and M. M. Chadwick, Mater. Sci. Eng. A **155**, 24 (1992).

[86] D. Pope and F. Chu, *Proceedings of the International Symposium on Structural Intermetallics*, edited by R. Darolia, J. J. Lewandowski, C. T. Liu, P. L. Martin, D. B. Miracle and M. V. Nathal (Warrendale, Pennsylvania: Metallurgical Society of AIME), p. 637, (1993).

[87] S. P. Chen, A. F. Voter, R. C. Albers, A. M. Boring and P. J. Hay, J. Mater. Res **5**, 995 (1990).

[88] S. V. Vonsovskiy, Yu. A. Izyumov and E. Z. Kurmayev, *Superconductivity of Transition Metals*, (Berlin: Springer, 1982).

[89] A. C. Lawson, Phys. Lett. **38A**, 379 (1972).

[90] K. Inoue, K. Tachskawa and V. Iwasa, Appl. Phys. Lett.**18**, 235 (1971).

[91] Ö. Rapp and L. J. Vieland, Phys. Lett. **36A**, 369 (1971).

[92] J. Crangle, K. Neumann and K. Ziebeck, J. Phys. D: Appl. Phys. **29**, 2362 (1996).

[93] V. V. Nemoshkolenko, V. Ya. Nagornyy and M. T. Kogut, Mettallofizika **3**, 29 (1981).

[94] T. Takashima and H. Hayashi, Japan. J. Appl. Phys **12** (10), 1659 (1973).

[95] A. S. Balankin, Yu. F. Bychkov and Ye. I Yakovlev, Fiz. Metal. Metalloved **56** (1), 119 (1983).

[96] A. Ormeci, F. Chu, J. M. Wills, T. E. Mitchell, R. C. Albers, D. J. Thoma, and S.P. Chen, Phys. Rev. B **54**, 12753 (1996).

[97] F. Chu, D. J. Thoma, T. E. Mitchell, C. L. Lin, M. Šob, Phil. Mag. B **77**, 121 (1998).

[98] Yu. A. Izyumov, V. Ye. Naysh and V. N. Syromyatnikov, Fiz. Metal. Metalloved. **39**, 455 (1975).

[99] P. Bujard, R. Sanjines, E. Walker, J. Ashkenazi and M. Peter, J. Phys. F **11**, 775 (1987).

[100] A. C. Switendick, in *Hydrogen in Metals I*, ed. by Alefeld, G., and Volkl, J., Topics Appl. Phys. **28**, (Springer, Berlin, Heidelberg, 1978), p.101.

[101] A. V. Skripov and V. N. Kozhanov, unpublished results.

[102] G. K. White, *Experimental Techniques in Low Temperature Physics* (Oxford University Press, 1968), p.285.

[103] H. M. Ledbetter, *Materials at Low Temperatures*, ed. by R. P. Reed and A. F. Clark (Metals Park, Ohio: American Society for Metals), p.1, (1983).

[104] K. Foster, R. G. Leisure and A. V. Skripov, accepted to Phys. Rev. B, (August 2001).

[105] A. V Skripov, M. Yu. Belyaev, K. N. Mikhalev and A. P. Stepanov, J. Alloys and Compd. **177**, 63 (1991).

[106] A. C. Lawson and W. H. Zachariasen, Phys. Lett. A **38**,1 (1965).

[107] T. R. Finlayson, E. J. Lanston, M. A. Simpson, E. E. Gibbs and T. F. Smith, J. Phys. F. **8**, 2269 (1978).

[108] J. W. Hafstrom, G. S. Knapp and A. T. Aldred, Phys. Rev. B **17**, 2892 (1978).

[109] A. S. Balankin and D. M. Skorov. Sov. Phys. Solid State **24** (4), 681 (1982).

[110] V. A. Finkel and Ye. A. Pushkarev, Zh.eksp. teor. fiz. **78**, 842 (1980).

[111] A. S. Balankin, Sov. Phys. Solid State **24** (4), 2102 (1982).

[112] T. Jarlborg and A. J. Freeman, Phys. Rev. B **22** (5), 2332 (1980).

Chapter 4

A Resonant Ultrasound Spectroscopy Study of a Ti-Zr-Ni Icosahedral Quasicrystal and a 1/1 bcc Crystal Approximant

- **4.1 Background**
- **4.2 Elastic Moduli of a Ti-Zr-Ni Icosahedral Quasicrystal and a 1/1 bcc Crystal Approximant**
- **4.3 Ultrasonic Study of Hydrogen Motion in a Ti-Zr-Ni Icosahedral Quasicrystal and a 1/1 bcc Crystal Approximant**
- **4.4 Summary**
- **References**

4.1 Background

Quasicrystals and Periodic Approximants:

Just as one cannot expect to successfully tile a floor with regular pentagons without leaving gaps, one of the long-standing assumptions of conventional crystallography was that 3-dimensional crystals cannot possess certain 'forbidden' rotational symmetries [1]. It can be shown readily that lattices with one-, two-, three-, four- and six-fold rotation axes can be used to fill all of space while maintaining the required translational periodicity. This is not the case, for example, for crystals possessing 5-fold rotational symmetry, so it was rather unexpected when in 1984 Shectmann *et al.* reported [2] that the electron diffraction patterns of certain melt-spun alloys of Al-Mn displayed such 5-fold symmetry. Since this initial discovery a series of intermetallic alloys

displaying icosahedral symmetry (or other forbidden symmetries such as 8-fold rotation) have been discovered. Materials of this nature are referred to as quaiscrystals (QC). The field of QCs and their related alloys now forms a sizable branch of materials physics [3][4]. QCs do not have a periodic atomic structure in 3-d space but they are crystal-like in the sense that they display long-range (aperiodic) order as evidenced from their discrete diffraction patterns. Interestingly, by applying a specific kind of strain to a QC (a 'phason' strain [5]) they can be transformed into conventional crystals, typically of very large unit cell, called periodic approximants [6]. The arrangement of the atoms and indeed many of the physical properties of the approximants are expected to be very similar to those of the related QC [7].

The connection between quaiscrystals and the work of British mathematician, Roger Penrose, was immediately noted. Penrose was interested in forming quasi-periodic tilings using basis tiles of more than one shape. The tilings, now known as Penrose tilings, fill a 2-d plane without translational symmetry but with inherent long-range order. This order is introduced through certain 'matching' rules that dictate how the tiles should be orientated relative to one another as the plane is filled. Figure 4.1 shows an example of a Penrose tiling pattern [8]. The building blocks of this tiling are two rhombi of different geometries which are shown in figure 4.1 (a). (The matching rules for this particular tiling are described in detail elsewhere [8].) The resultant tiling is shown in figure 4.1 (b). This tiling has (long-range) 5-fold rotational symmetry. The tiling does not have a single axis of rotation through which this 5-fold symmetry is evident. Rather, the tiling must be rotated through 2π / 5 Rad *and* translated to project the tiling into itself. This may not be

immediately obvious to the reader, but following parallel lines within the tiling can aid the visualization; two of five 'rows' at angles of $2n\pi$ / 5 Rad (n = 1, 2, 3 and 4) with respect to each another have been highlighted in figure 4.1 (c). Levine and Steinhardt [9] had been working on a theoretical model for a three dimensional solid of icosahedral symmetry based on a 3-d form of Penrose tiling. This work provided much of the initial theoretical framework for describing the atomic structure of quasicrystals.

Most quasicrystals are based either on Al or Ti. Developments in materials synthesis have produced QCs and approximants of sufficient macroscopic size to make RUS experiments accessible. There is considerable interest in the elasticity of icosahedral phase QCs as they are expected, from theoretical considerations, to be elastically isotropic [10]. This is unlike the situation in regular crystals which are fundamentally anisotropic.

Present Work:

The elastic constants and the ultrasonic attenuation of a Ti-Zr-Ni quasicrystal (QC) and its related 1/1 bcc crystal approximant have been measured using the technique of resonant ultrasound spectroscopy. Section 4.2 reports the very first measurements of this kind to be made on a Ti-based quasicrystalline system. The measurements were made over a temperature range of 15 - 300 K. A knowledge of the elastic constants has become extremely relevant for these systems. Due to the lack of regular periodicity the atomic structure of QC systems is often rather difficult to determine. The elastic constants are regularly used as a test of first-principle total-energy calculations and for refining the form of the atomic potentials suggested for these complex structures. For these reasons a direct comparison between the elastic moduli of the QC and the approximant phase was desired.

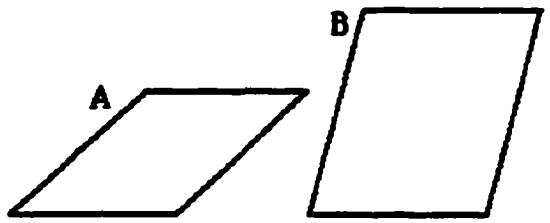

(a)

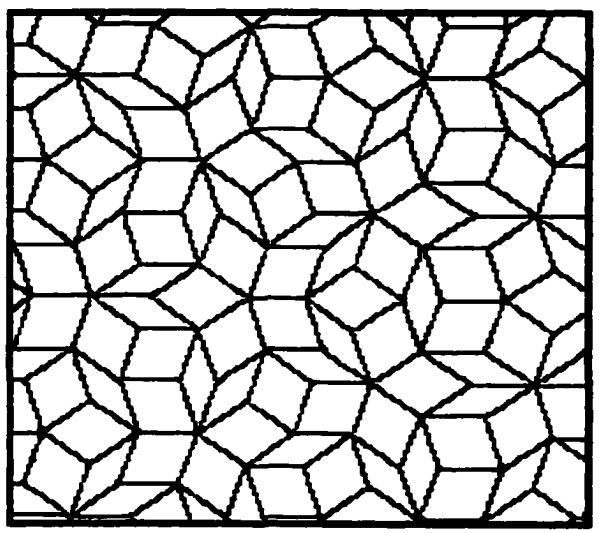

(b)

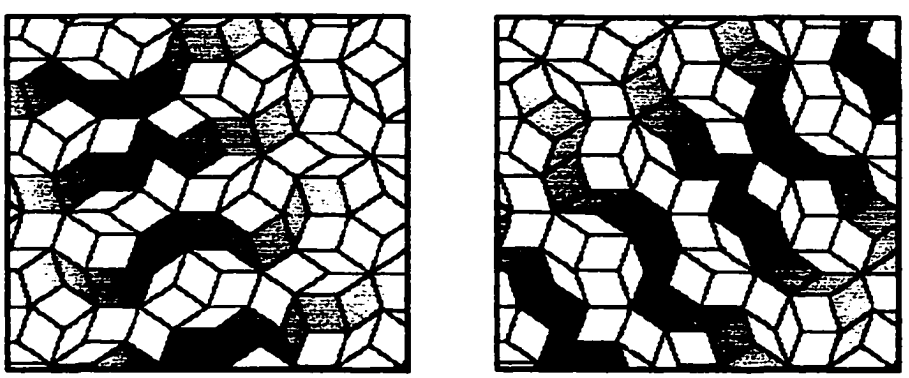

(c)

Figure 4.1: Example of a Penrose tiling [8]. Figure 4.1 (a) shows the two rhombi used to create the pattern shown in figure 4.1 (b). Rhombus 'A' has internal angles of 36° and 144°; rhombus 'B' has angles of 72° and 108°. In figure 4.1 (c) two sets of 'rows' are shaded to aid visualization of the 5-fold rotational symmetry.

It was found [11] that the Ti-Zr-Ni based quasicrystal can absorb and desorb hydrogen to a metal to hydrogen atom ratio of H / M = 1.88; making them of some interest for hydrogen storage applications. The specific theoretical interest in the hydrogenated systems stems from the apparent opportunity to investigate the dynamics of diffusion of light interstitials within a quasi-periodic lattice. It was hoped that by comparing the attenuation results for the QC to those of the approximant phase information on the similarity of the hydrogen environments in the two systems could be investigated. It was suggested that hydrogen could perhaps be used as a probe of the local structure in these materials. The results of an ultrasonic study of hydrogen motion within these materials is presented in section 4.3.

4.2 Elastic Moduli of a Ti-Zr-Ni Icosahedral Quasicrystal and a 1/1 bcc Crystal Approximant

4.2.1 Introduction

An ever growing body of theoretical and experimental work has been devoted to the study of quasicrystalline systems [12]. Most of the studies have dealt with the largest class of quasicrystals, based on aluminum. This class of materials were the first to be discovered and several phases are known to be stable. Several elastic modulus studies have been performed on the Al-based quasicrystals. These experiments [13][14][15][16] showed, with increasing precision, that the icosahedral phase quasicrystals exhibit the

theoretically expected [10][17] elastic isotropy. A more recent experiment [18] showed that the decagonal Al-Ni-Co quasicrystal is, as expected, transversely elastically isotropic.

While the largest class of quasicrystals is Al-based, the second largest is based on titanium [19]. Recently, a stable Ti-Zr-Ni quasicrystal has been discovered [20][21]. In addition, a closely related 1/1 crystal approximant to the stable Ti-Zr-Ni quasicrystals has been discovered [22][23]. There appear to have been no studies of the elastic properties of the Ti-based materials. Elastic constants are of fundamental importance. Ultrasonic measurements yield the adiabatic moduli and thus are the second derivative of the internal energy with respect to the strain. The lack of periodicity in quasicrystals makes the determination of their crystal structure difficult. To be viable, structures proposed from diffraction and electron microscopy studies should be stable to small fluctuations. Measured elastic constants are critical for refining the shape of the atomic potentials used in these studies. In addition, the elastic constant measurements can be used to calculate the low-temperature acoustic contribution to the specific heat [24] which has a characteristic T^3 dependence. In the case of Al-Mn-Pd and Al-Re-Pd icosahedral quasicrystals, the measured low-temperature T^3 specific heat was larger than expected from the sound velocity measurements, revealing an excess specific heat of unknown origin. Apparently there have been, as yet, no measurements of the low-temperature specific heat in the Ti-based quasicrystals.

Given the importance of the elastic moduli, the lack of data in this class of materials, and the availability of relatively large stable specimens, elastic constant measurements on both the Ti-Zr-Ni quasicrystal and the 1/1 crystal approximant phase

were made.

4.2.2 Experimental Details

Alloys of the desired composition, $Ti_{41.5}Zr_{41.5}Ni_{17}$ for the *i*-phase (icosahedral QC) and $Ti_{44}Zr_{40}Ni_{16}$ for the 1/1 approximant phase, were prepared (at Washington University, St. Louis) by arc-melting mixtures of the pure elements on a water-cooled copper hearth in a high-purity Ar gas atmosphere. The *i*-phase quasicrystal and the *W*-phase approximant were prepared by annealing the resulting ingots in a graphite crucible, which was placed inside a quartz tube. A Ti-Zr alloy used as an oxygen getter, was also placed in the tube, but was separated from the sample. The tube was then evacuated and sealed under a vacuum of 10^{-5} - 10^{-6} Torr. Oxygen contamination of the sample during annealing was prevented by first heating the Ti-Zr getter to 1000 °C for 10 min by rf induction, while keeping the alloy ingot in a graphite crucible at room temperature. The tube containing the sample and the getter was then annealed in a furnace for the following times: 64 h at 610 °C to obtain the *W*-phase and 64 h at 570 °C to form the *i*-phase. Phase-purity was confirmed by x-ray and transmission electron microscopy (TEM) investigations. TEM microstructural studies of both samples revealed a distribution of grain sizes, with a largest diameter of a few μm.

Samples were hand polished into accurate rectangular parallelepipeds for the ultrasonic measurements, as described in section 2.2. The final room temperature dimensions were 1.321*1.100*1.644 mm^3 for the *i*-phase and 2.197*1.318*1.621 mm^3 for the *W*-phase alloy. The room-temperature densities, determined by immersion weighing in

toluene, were found to be 6.081 ± 0.008 g/cm^3 and 6.066 ± 0.010 g/cm^3 for the *i* and *W*-phases respectively. Resonant ultrasound spectroscopy [25][26][27][28] was used to determine the elastic constants of these materials. This technique is one of the few experimental methods which could have facilitated elastic moduli determination on the millimeter-sized samples available for the present study. For both the *i* and *W*-phases 40-50 of the lowest frequency vibrational eigenmodes of the parallelepiped were excited. These modes were detected in a frequency range of 0.4 - 2.0 MHz. A section of the RUS spectrum for the *W*-phase material is shown in figure 4.2 at 295 K and 80 K. An increase in the resonant frequencies and a narrowing of the Lorentzian line shapes can clearly be observed for the modes at 80 K compared to those at 295 K. The ultrasonic loss in both alloys was low resulting in resonant modes of high quality factor ($Q > 10^4$), which enabled particularly accurate determination of center frequencies (≤ 5 in 10^6). The rms difference obtained for all samples in the present study was excellent, between 0.10 - 0.15 % for the 50 lowest frequency modes. The measurements were carried out using the gas-flow system at roughly ambient pressure in a ^{4}He atmosphere, over a temperature range of 15 - 300 K.

4.2.3 Results and Discussion

The measurements are analyzed in terms of two independent elastic constants as appropriate for isotropic materials. As mentioned in Section 4.2.2, the typical grain size of the materials is much smaller than the sample size. There is no reason to assume any preferred orientation (texture) of these grains, thus we assume elastic isotropy in the

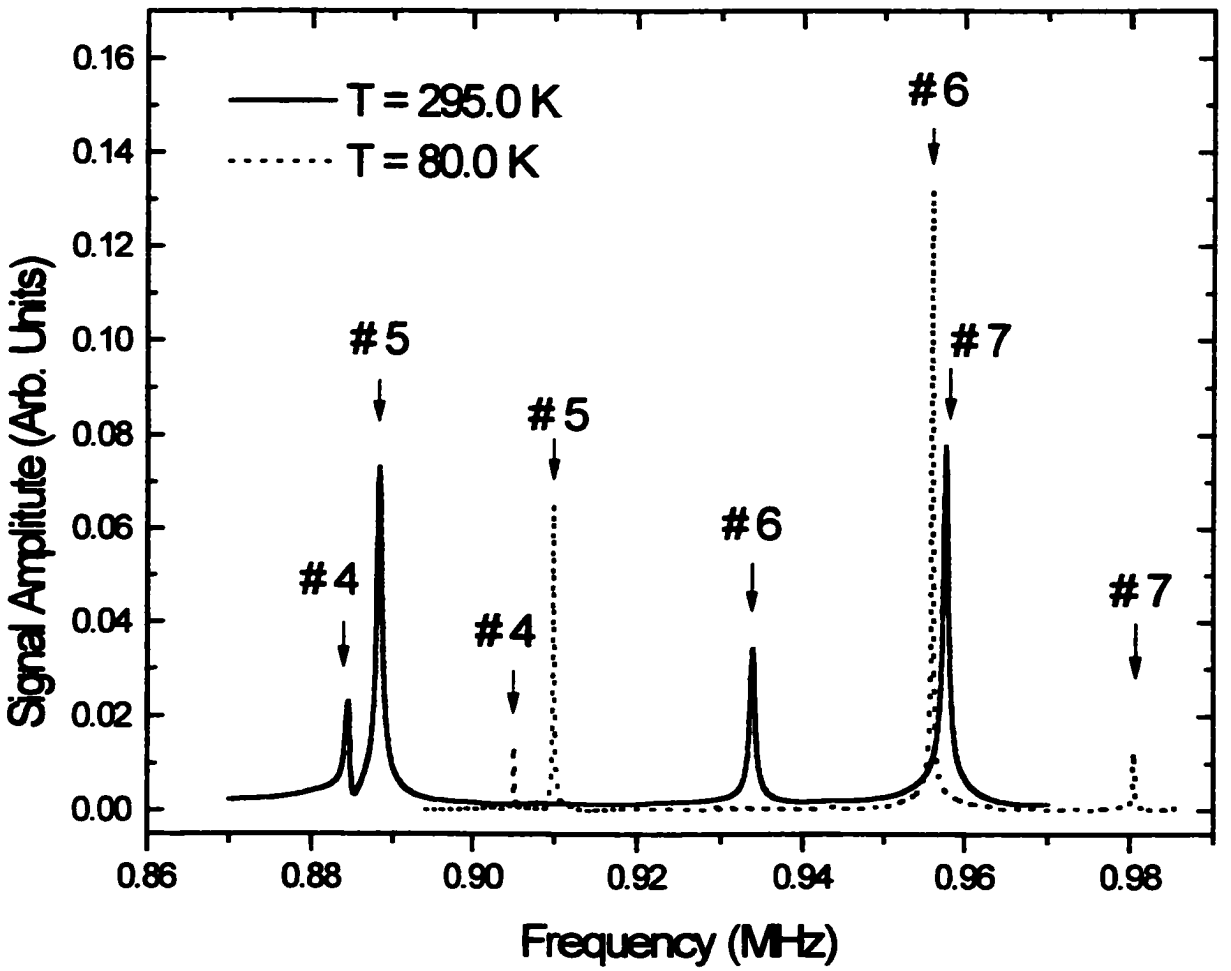

Figure 4.2: Low frequency section of the RUS spectrum for the *W*-phase Ti-Zr-Ni crystal approximant. Modes # 4 through # 7 are shown. For comparison the same four modes are shown at 295 K and at 80 K. Clearly the quality factor (Q) and center frequency (f_0) of the resonant modes have increased with decreasing temperature for the temperatures shown.

analysis. This argument applies to both the *i*-phase and *W*-phase alloys. It is expected that the *i*-phase material would be elastically isotropic [16][17] even if measurements could be made on a single grain. We fit our measured frequencies to the elastic constants C_{11} and C_{44} where the subscripts refer to the coordinate system aligned with the sample parallelepiped axes. We present the results, however, in terms of the shear modulus G and the bulk modulus B, where

$$G = C_{44} \qquad \text{and} \qquad B = C_{11} - \frac{4}{3}C_{44} \tag{1}$$

To the extent that the *i*-phase material is intrinsically isotropic, G and B represent the two independent elastic constants for the material. For the *W*-phase material, G and B represent the usual poly-grained averages. Figure 4.3 presents results for the shear modulus G over the temperature range of 15 - 300 K for both the *i*-phase and *W*-phase crystal approximant. Figure 4.4 presents similar results for the bulk modulus B. The overall temperature dependance of the moduli is similar for the two materials, although there is a small difference. The *W*-phase shows a slightly stronger increase in the moduli with decreasing temperature, and is, in some sense, more anharmonic. We estimate the accuracy of the measurements, based on the quality of the RUS fit and errors in the density measurement, to be 0.2 % for G and 2 % for B. The accuracy is higher for G than for B as most of the lower frequency modes depend much more strongly on G than on B. This point is highlighted in table 4.1 which presents a section of the RUS fit for the *W*-phase material. The 15 lowest frequency modes are shown. Of these modes, mode nine

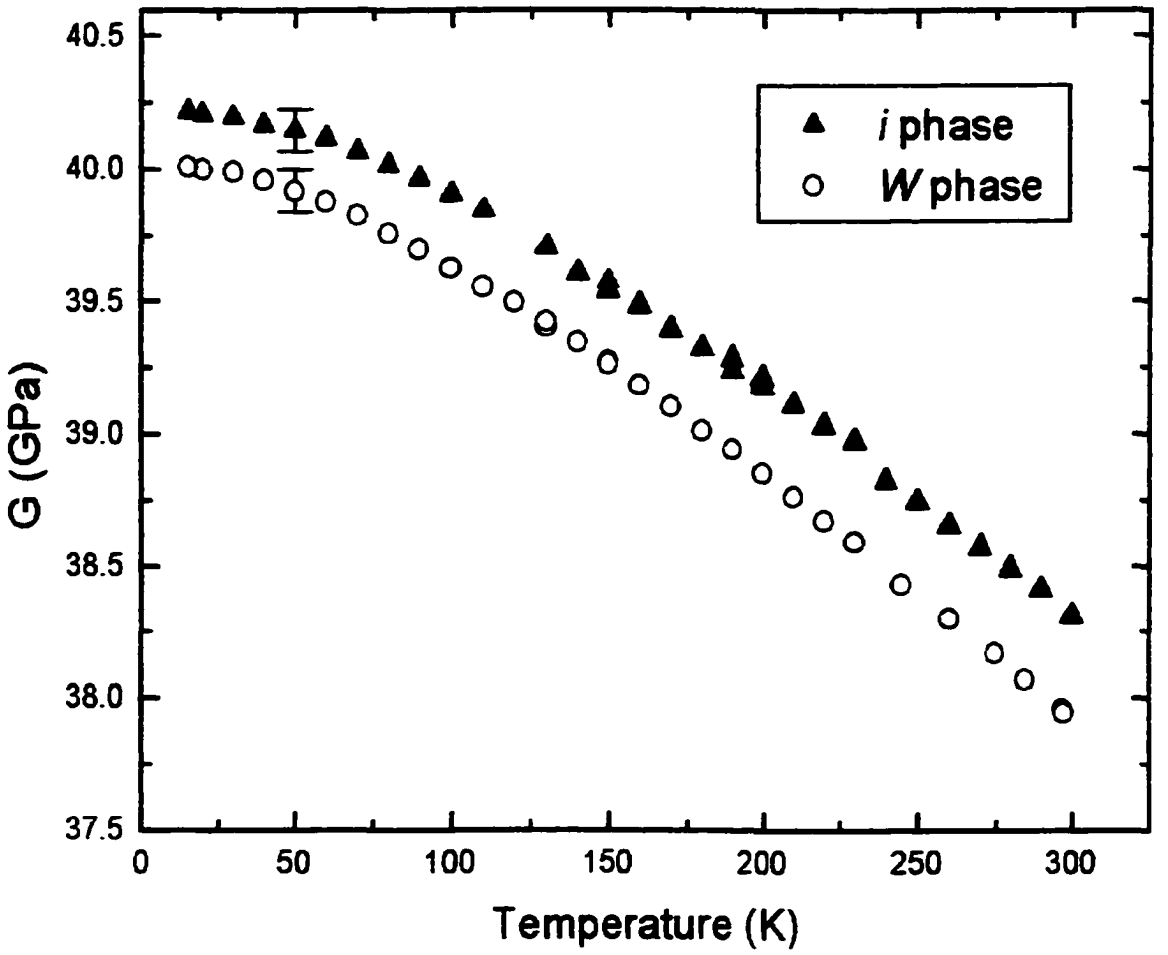

Figure 4.3: Shear Modulus G vs temperature for a Ti-Zr-Ni quasicrystal (i-phase) and a 1/1 crystal approximant (W-phase). Typical error bars for the absolute accuracy are shown.

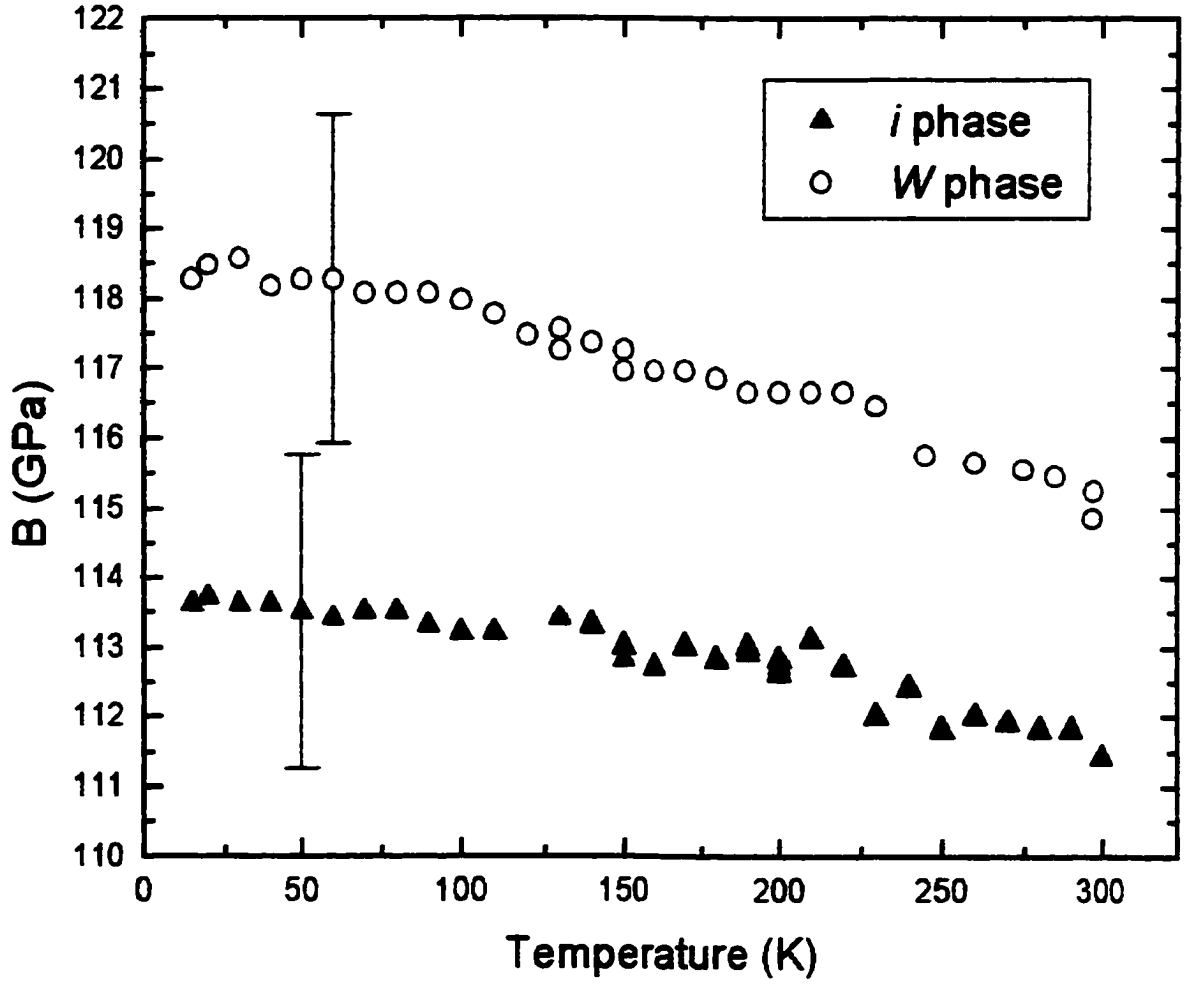

Figure 4.4: Bulk Modulus B vs temperature for a Ti-Zr-Ni quasicrystal (i-phase) and a 1/1 crystal approximant (W-phase). Typical error bars for the absolute accuracy are shown.

Table 4.1: Typical output of the RUS computation, for the *i*-phase Ti-Zr-Ni quasicrystal. Only the 15 lowest frequency modes (n) are shown. The measured frequencies (f_{expt}), calculated frequencies (f_{theory}) and their % difference (% err) are given. The weight given to each mode (wt) in the RUS fit to the elastic constants and the symmetry indexes (k, i) are shown. Finally the % dependence of each mode on the two independent elastic constants (C_{44} and C_{11}) are also listed.

n	f_{expt} (MHz)	f_{theory} (MHz)	% err	wt	k	i	% C_{44}	% C_{11}
1	0.742482	0.737205	-0.71	0	4	1	100	0
2	0.972942	0.974051	+0.11	1	7	2	92	8
3	1.045120	1.044561	-0.05	1	1	2	90	10
4	1.155710	1.150941	-0.41	1	4	2	100	0
5	1.165730	1.165954	+0.02	1	2	2	99	1
6	1.262720	1.265877	+0.25	1	5	1	97	3
7	1.283960	1.284933	+0.08	1	8	2	99	1
8	1.352700	1.349098	-0.27	1	3	2	96	4
9	1.378750	1.377635	-0.08	1	7	3	80	20
10	1.405010	1.405792	+0.06	1	6	2	94	6
11	1.442280	1.445083	+0.19	1	3	3	96	4
12	1.452100	1.454205	+0.14	1	5	2	96	4
13	1.521000	1.519779	-0.14	1	8	3	90	10
14	1.575350	1.571006	-0.28	1	3	4	97	3
15	1.591580	1.596678	+0.32	1	5	3	97	3

has the strongest dependence on C_{11} at just 20 %. Note also the excellent agreement between the computed and measured frequencies. From figures 4.3 and 4.4 it can be seen that the absolute error in the modulus measurements is considerably larger than any random scatter in the data presented. This is because the contributions to the total absolute error from the density and the quality of the RUS fit are systematic across the temperature range studied.

Thermal expansion data are not available for these materials at low temperatures so the results have not been corrected for thermal contraction; the room-temperature and densities have been used in the analysis. Taking into account the direct dimensional effect through the density, the elastic constants deduced from the measured frequencies vary inversely as the dimension. Metals such as Ti have a total thermal contraction between room temperature and 4 K of about 0.15 - 0.20 % [29]. Assuming that the materials in the present study behave similarly, the neglect of thermal contraction effects in the analysis of the data leads to a comparable error; that is, the total increase in the elastic constants as the temperature is lowered from room temperature to 15 K would be about 0.15 - 0.20 % greater than that shown in figures 4.3 and 4.4.

A comparison was made of the values of G and B obtained in the present experiment with literature values for those of the constituent metals Ti, Zr and Ni [30]. For a crude comparison a weighted average for $Ti_{41.5}Zr_{41.5}Ni_{17}$ (i-phase composition) was calculated. In this way values of 115.7 and 117.9 GPa were estimated for B at room temperature and 4 K respectively. Remarkably, these values are almost the same as those measured for the i and W- phase materials. For G, the computed aggregate value depends

on the method of averaging the single-crystal values. We used the mean of the Voigt and Reuss averages for the hexagonal metals titanium and zirconium. (The Voigt and Reuss averages differ by only a few percent in these cases.) For the cubic material we used the Kröner average [31]. The corresponding calculated values for G are 47.7 and 54.4 GPa at room-temperature and at 4 K respectively. The 4 K results are 35 % higher than those measured for the *i* and *W*-phases (at 15 K, the lowest temperature achieved). These results imply that for hydrostatic compression both phases behave as the weighted average of the constituent metals. Conversely, they are softer to shear than the weighted average of the constituent materials.

The present measurements can be used to compute the long-wavelength phonon contribution to the heat capacity C_{ac}. In the low temperature limit the specific heat is given by [32]

$$C_{ac} = \frac{2\pi^2 k_B^4}{5\hbar v_0^3} T^3, \tag{2}$$

where v_o is an average sound velocity, which in the present case is given by

$$\frac{1}{v_0^3} = \frac{1}{3}\left(\frac{1}{v_l^3} + \frac{1}{v_t^3}\right) \tag{3}$$

where the subscripts *l* and *t* refer to the longitudinal and transverse sound velocities respectively. Using the results reported above it is found that $v_o = 2.89*10^3 \pm 10$ m/s for

both the *i* and *W*-phase materials. The acoustic contribution to the low-temperature molar specific heat is found to be $C_{ac} / T^3 = 5.64*10^{-5} \pm 0.05 *10^{-5}$ J / (mol K^4) and $5.59*10^{-5} \pm 0.05*10^{-5}$ J / (mol K^4) for the *i* and *W*-phases respectively. These values are considerably larger than the predicted acoustic contribution in decagonal Al-Ni-Co ($0.89*10^{-5} \pm 0.05$ J/(mol K^4) [18][33], or icosahedral Al-Mn-Pd ($1.63*10^{-5} \pm 0.05$ J/(mol K^4) [24]. The reason for the difference is the lower v_o in the Ti-Zr-Ni systems as compared to the other materials.

4.2.4 Conclusions:

The shear modulus *G* and the bulk modulus *B* of icosahedral Ti-Zr-Ni (*i*-phase) and Ti-Zr-Ni crystal approximate (*W*-phase) have been measured. Assuming that the *i*-phase is intrinsically isotropic as is expected theoretically and experimentally for this symmetry, *G* and *B* represent the two independent elastic constants of this material. For the *W*-phase material, *G* and *B* represent the usual poly-grained averages. The elastic moduli of the two materials are almost identical. This result provides further evidence for the close similarity of the QC to its 1/1 crystal approximant. The temperature dependence of the moduli resembles those of ordinary metals. The moduli for the *W*-phase were slightly more temperature dependent than those of the *i*-phase. The results permit an estimation of the acoustic phonon contribution to the specific heat which was found to be considerably larger for the Ti-based materials than for the Al-based materials reported by others. These results should prove useful in the construction of atomic potentials for these

materials.

4.3 Ultrasonic Study of Hydrogen Motion in a Ti-Zr-Ni Icosahedral Quasicrystal and a 1/1 bcc Crystal Approximant

4.3.1 Introduction

An understanding of the motion of hydrogen in metals and intermetallics is of considerable importance for both technological and scientific reasons [34]. Metal-hydrogen systems are used in a variety of technological applications, as discussed in section 3.1.1. Most applications require a high diffusion coefficient of the hydrogen in the host material. From the scientific point of view, the interactions of these light interstitials with phonons and conduction electrons result in a rich variety of diffusion mechanisms that are not yet fully understood. The study of hydrogen in metals has progressed from simple crystalline systems to more complicated crystalline structures, to amorphous and nano-crystalline systems, and more recently, to quasicrystalline materials. The work detailed in the following sections involves an ultrasonic study of H motion in an intermetallic compound of quasi-periodic order.

Viano *et al.* [11] first demonstrated that the Ti-based QCs and their related alloys are able to absorb and desorb hydrogen. In most transition metal alloys, hydrogen atoms prefer to sit in tetrahedrally co-ordinated sites. For example, H diffusion in the polytetrahedral Laves-phases has been studied extensively [35][36][37][38] with a number

of different techniques. Chapter 3 of this thesis reported a detailed ultrasonic study of hydrogen motion in the C15 Laves-phase system $TaV_2H(D)_x$. Hydrogen motion in these intermetallic phases tends to be more complex than in simple metals due to the large number and variety of the interstices. Icosahedral QCs are also likely dominated by tetrahedral order and thus provide a variety of sites and migration paths for interstitial hydrogen [39][40].

There have been few reported studies of hydrogen motion in QCs. Neutron scattering, nuclear magnetic resonance (NMR), and various forms of mechanical spectroscopy are the usual methods of studying hydrogen hopping in materials. Hydrogen dynamics in icosahedral $Ti_{45}Zr_{38}Ni_{17}H_{150}$ were investigated by neutron scattering [41]. Hydrogen hopping in the $Ti_{45-x}V_xZr_{38}Ni_{17}$ system with $x = 0.00$ and 2.00 was also studied by NMR [42][43]. These materials were loaded to a hydrogen to metal atom ratio (H / M) as high as 1.88. It appears that there have been no studies of hydrogen motion in QCs with any form of mechanical spectroscopy. Ultrasonic measurements provide a powerful complement to NMR and neutron measurements for the study of hydrogen dynamics in materials [44][45]. Using ultrasound it is possible to investigate time-scales which are difficult or impossible to examine with other techniques. An ultrasonic study of hydrogen motion in QCs can therefore potentially add to the present quantitative and qualitative understanding of hydrogen diffusion in quasiperiodic systems. Based on the dearth of information about hydrogen dynamics in QCs, especially in the frequency range accessible to ultrasound, ultrasonic measurements were made on a Ti-Zr-Ni QC loaded with hydrogen. Additionally, measurements were made on a 1/1 bcc crystal approximant of the

QC. It appears that there is no information about the hydrogen dynamics in these closely related crystalline systems. A comparison of the ultrasonic attenuation results in the QC and the crystal approximant should provide information on the similarity of the hydrogen environments in these two systems.

4.3.2 Experimental Details

The same RP samples prepared for the measurement of the elastic constants of the *i* and *W*-phase alloys described in section 4.2 were used for this study. The samples were loaded with hydrogen (by W. J. Kim at Washington University, St. Louis, MO) from the gas phase to hydrogen to metal atom ratios of H / M = 0.79 and 0.20 for the *i* and *W*-phase respectively. Prior to the exposure to hydrogen, the samples were plasma-etched in argon and coated with a thin layer of Pd (approximately 15 - 30 nm). The Pd coating protects the samples from oxidation on subsequent exposure to air and enhances the disassociation of molecular hydrogen. The hydrogenation was carried out in stages at 350 °C. At each stage a small amount of hydrogen, corresponding to $\Delta H / M \approx 0.1$, was introduced into the chamber. Additional hydrogen was added only after the pressure reached equilibrium. The total charging time was 13 h for the *W*-phase and 44 h for the *i*-phase. The H / M ratios were determined directly by the weight gain due to hydrogenation using a Cahn electrobalance with an accuracy of ±5 μg, and by the hydrogen pressure change upon loading. As expected, the two techniques gave similar estimates for the amount of hydrogen absorbed. Since it is known that the amount of hydride phase formed after the full loading (H / M = 1.6) is small (less than 5 % volume

fraction), the samples for the present work (loaded to much lower H / M ratios) were assumed to be single phase.

The ultrasonic loss measurements were made over a temperature range of 15 - 345 K by measuring the Q values of several lower frequency modes. The 'background' ultrasonic loss of the hydrogen free materials had been measured in the same way over a similar temperature range.

4.3.3 Results and Discussion

Figure 4.5 shows the ultrasonic loss, $1/Q$, as a function of temperature for two frequencies in the W-phase material. Also shown is the loss in the hydrogen-free material. There is a prominent loss peak in the hydrogenated material with a maximum at about 250 K for a measurement frequency of ≈ 1 MHz. The peaks shift to higher temperatures with increasing frequency as expected for a thermally activated process. The relatively high loss near the attenuation maximum, combined with the small samples used, presented experimental difficulties. A coherent background signal, due to cross-talk between the transmitting and receiving transducers, gave a non-Lorentzian resonance signal in many cases, as described in section 2.2. In cases where the background was not too large compared to the signal from the sample, the data could be reliably corrected for this effect [46]. Good results were obtained for five modes in the frequency range of 0.72 to 1.86 MHz. The solid and dashed lines in figure 4.5 were calculated using parameters from a least squares fit of the data for these five frequencies. This fit is discussed later in this

section. Figure 4.6 shows attenuation results for the *i*-phase material for both the hydrogen-free and hydrogenated material. There are two apparent differences from the data shown in figure 4.5. Firstly, the attenuation due to hydrogen is higher in the *i*-phase material, likely due to the higher concentration of hydrogen in this material. Secondly, the attenuation peaks occur at a lower temperature - about 30 K lower - in the *i*-phase material. The solid lines in figure 4.6 are a guide to the eye, not a theoretical fit to the data. The higher attenuation in this material lead to a greater scatter in the data so unfortunately it was not feasible to fit the results reliably to theory to obtain an activation energy.

Turning to a more detailed discussion of the data for the *W*-phase, the attenuation peaks are interpreted as a Debye-type relaxation involving hydrogen hopping between two nearby interstitial sites, as discussed in section 3.1.3. It is usually assumed that the ultrasonic strain modulation of E is due to a modulation of A, not Δ_0 in which case relaxation attenuation occurs only if the two sites involved are nonequivalent with respect to the applied stress. According to the selection rules for anelasticity [47], anelastic relaxation is only possible if the interstitial site symmetry of the hydrogen is lower than the crystal symmetry. In the present case the location of the hydrogen is unknown so the theoretical rule cannot be applied, but the experimental fact that attenuation peaks are observed indicates that the rule is satisfied in both materials studied. We attempted to fit the loss data using **Eq.** (5) of chapter 3 with a simple Arrhenius expression for τ,

$$\tau = \tau_o \exp(E_a / k_B T) \tag{4}$$

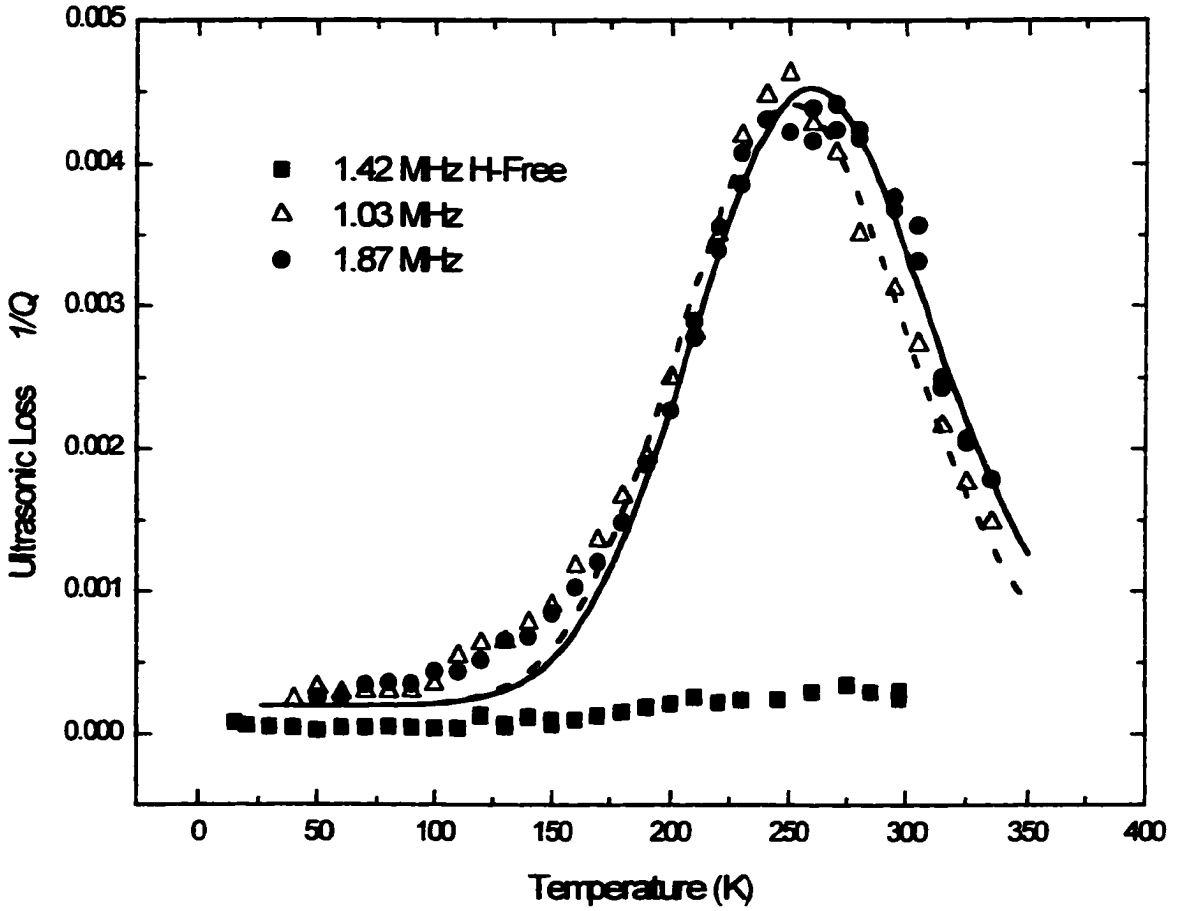

Figure 4.5: Ultrasonic loss (*1/Q*) verus temperature for *W*-phase Ti-Zr-Ni loaded to H / M = 0.20. The loss for the hydrogen free material is also shown. The solid and dashed lines represent a fit to the data using parameters given in the text. A constant loss of 0.0002 was added to the theoretical curves as a background attenuation.

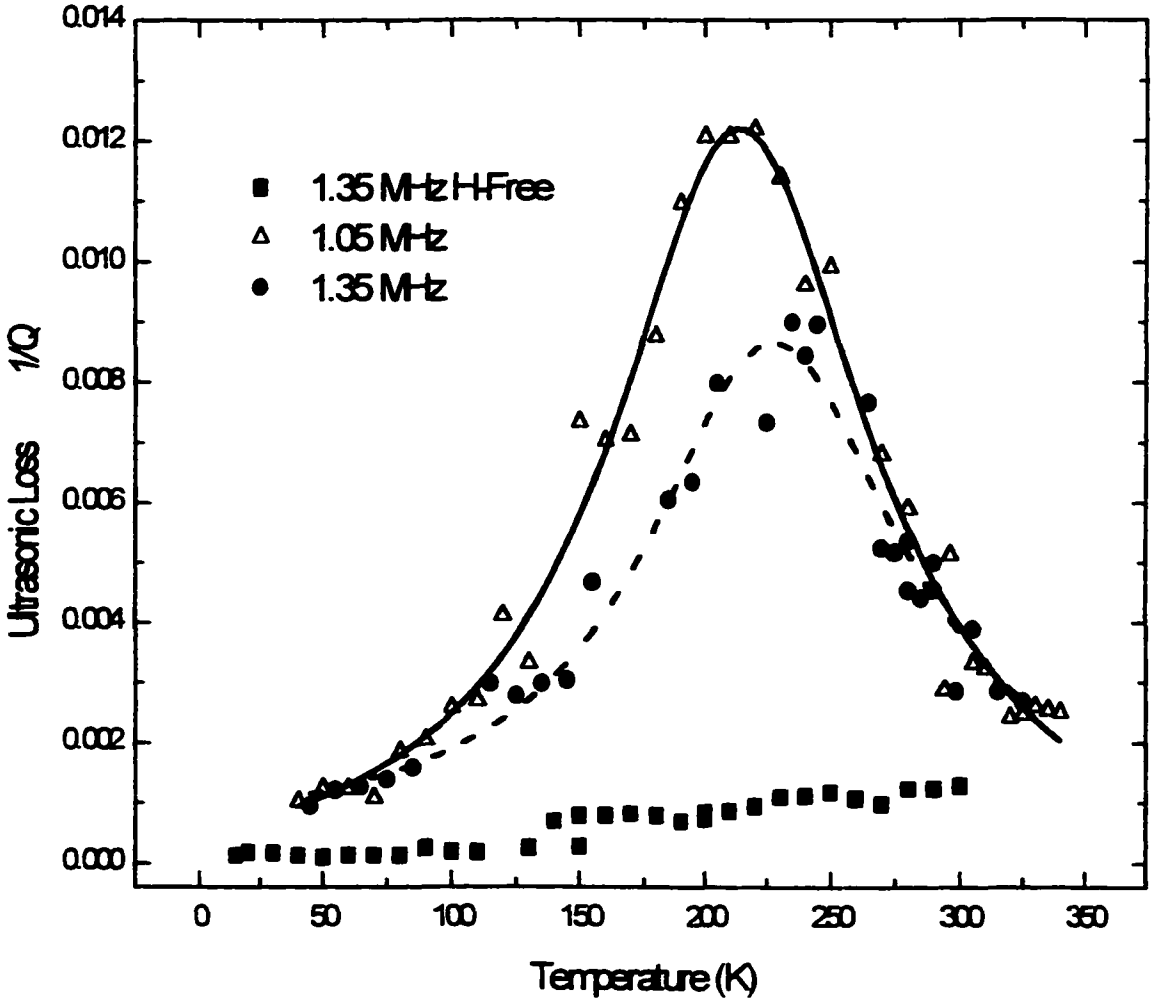

Figure 4.6: Ultrasonic loss ($1/Q$) verus temperature for *i*-phase Ti-Zr-Ni loaded to H / M = 0.79. The loss for the hydrogen free material is also shown. The symbols represent the data. The lines are guides to the eye and *do not* represent fits to the data.

where τ_0^{-1} is an attempt frequency and E_a is an activation energy. An Arrhenius plot of the temperature shift of the peak position with frequency provided an initial value for the activation energy. It was found that the peaks of figure 4.5 are much broader than can be fit by such a value for E_a. Attempts were therefore made to fit the results with a distribution of activation energies centered about some mean activation energy, *i.e.* by integrating **Eq.** (5) (chapter 3) over a Gaussian distribution of activation energies. As a justification, a distribution of interstitial *site* energies was needed to fit the pressure-composition isotherm data for the *W* and *i*-phases of Ti-Zr-Ni [48]. A least squares fit to the data was made for five frequencies in the range of 0.7 MHz to 1.9 MHz to determine the parameters E_a, σ, and τ_o. Here σ represents the width of the Gaussian distribution. This procedure gave a reasonably good fit to the data except at the lower temperatures. Below 180 K there is a systematic deviation of the data from the fit, observed for all the measured frequencies. Thus, only data above 180 K were used for the least squares fit. The solid and dashed lines in figure 4.5 represent these fits for the *W*-phase material. A constant background of 0.0002 was added to the theoretical curves to approximately match the measured background attenuation at low temperatures. The fit parameters for the *W*-phase are: $E_a = 0.40 \pm 0.05$ eV, $\sigma = 0.071$ eV, and $\tau_o = 1.6 \times 10^{-15}$ s. The value of 0.40 eV obtained for the activation energy is in good agreement with the value derived from the Arrhenius plot. There are no other ultrasonic measurements of hydrogen motion in the *W*-phase alloy available for comparison. However, a comparison may be made to neutron and NMR measurements on the icosahedral phase of Ti-Zr-Ni. In an NMR study

of icosahedral $Ti_{45}Zr_{38}Ni_{17}$ loaded to a H / M = 1.88 Shastri *et al.* [44] found that a distribution of activation energies was required to fit the ^1H spin-lattice relaxation data with the resulting parameters: E_a = 0.35 eV, σ = 0.053 eV, and $\tau_o = 1.7 \times 10^{-13}$ s. This value for the activation energy lies just within the error range of the activation energy derived from the ultrasonic measurements on the *W*-phase with H / M = 0.20. The values for τ_o, however, differ by a factor of 100, which deserves further comment. The value of τ_o required to fit the ultrasonic data depends exponentially on the value of E_a chosen. For example, if E_a = 0.35 eV was assumed, which is at the bounds of the experimental error, the value of τ_o required would be 1.5×10^{-14} s, only a factor of 10 different from the NMR results. It is interesting to note that the one neutron scattering study on *i*-phase Ti-Zr-Ni revealed an inelastic peak at 130 meV. This corresponds to a hydrogen vibration period of 3.2×10^{-14} s, a value that is quite compatible with our results. (The value of σ required also depends on the value chosen for E_a. With E_a = 0.35 eV our optimum value of σ = 0.057 eV is essentially the same as the NMR value.) A further similarity between the present ultrasonic results on the *W*-phase and the earlier NMR results on the *i*-phase is the deviation between theory and experiment for temperatures below the maximum. This occurs below 300 K for the NMR results (measured at much higher frequencies) and below 180 K in the present case. The fact that such deviations are observed in both experiments suggests that the cause is not specific to the type of experiment and may be an indication of a second relaxation process occurring on a different frequency scale. Alternatively a Gaussian distribution of activation energies may simply not be appropriate for the major relaxation process; however, the present data do not justify a more

complicated approach. The overall evidence indicates that the motion observed with ultrasound in the *W*-phase material is similar in nature to that observed by NMR in the *i*-phase and associated with long-range hydrogen diffusion.

Turning to the ultrasonic results for the *i*-phase, figure 4.6 shows considerable scatter in the data associated with the higher attenuation. It was, therefore, not possible to reliably fit the data to theoretical curves to obtain parameters for the hydrogen motion. Nevertheless, certain conclusions can be drawn. The most important point is that for similar measurement frequencies the peaks clearly occur at lower temperatures in the *i*-phase as compared with the *W*-phase. From the parameters derived from fitting the *W*-phase attenuation data, the H motion in the *i*-phase is estimated to be at least an order of magnitude faster than that in the *W*-phase. Unfortunately, the H / M ratios are different for the two materials, making it difficult to discern whether this faster motion reflects a basic difference between the structural configuration of the interstitial sites of the two materials, or whether it is due to concentration-dependent effects. Hydrogen diffusion coefficients have been observed to increase as a function of H / M in amorphous materials. This was attributed to the filling of sites with higher energies at higher H concentrations with a corresponding decrease in the average activation energy [49]. Such an effect may be important in the present materials.

4.3.4 Conclusions

Ultrasonic measurements were made on a Ti-Zr-Ni icosahedral quasicrystal and a closely related 1/1 bcc crystal approximant. The icosahedral and approximant materials

were hydrogenated to a hydrogen to metal ratio of 0.79 and 0.20 respectively. Temperature-dependent attenuation peaks were observed in the alloys containing hydrogen, while the hydrogen-free material showed no unusual features. The peaks shifted to higher temperatures with increasing ultrasonic frequency as expected for thermally activated motion. A Gaussian distribution of activation energies was required to fit the ultrasonic loss data. A mean activation energy for the hydrogen motion of 0.40 ± 0.05 eV with a distribution width of 0.07 eV was found for the crystal approximant phase. The data did not permit a determination of the activation energy for the icosahedral phase, but the attenuation peaks for this phase clearly occurred at lower temperatures than for the crystalline material. The results indicate that hydrogen motion is roughly an order of magnitude faster in the icosahedral phase in the temperature range of 225 K. Whether this result is due to a basic difference in the hydrogen environment in the two materials, or due to a dependence on the hydrogen concentration cannot be determined from the present measurements. Future experiments at Colorado State as a function of hydrogen concentration are planned to answer this question. The results demonstrate that mechanical spectroscopy is a useful tool for studying hydrogen motion in this unusual class materials.

4.4 Summary

The conclusions of the RUS investigation into the elastic properties of a Ti-Zr-Ni based quasicrystal and its related 1/1 bcc crystal approximant were reported in section 4.2.4. Similarly the conclusions of the study into the H motion in the same systems were

provided in section 4.3.4. It has been shown that RUS can be used successfully to measure both the elastic constants and ultrasonic attenuation in these systems.

However, the success of the work on the hydrogenated systems was limited for two main reasons. Firstly, the H concentration in the QC and the approximant was different, so it was impossible to deduce with certainty if the discrepancy in the attenuation results for the two systems originated from a variation of the hydrogen environments of the two systems or is related to hydrogen concentration effects. To elucidate this concern is of prime interest. Related to this is the fact that the H concentration of $H / M = 0.79$ in the QC was high enough to cause very strong attenuation in this system, at temperatures where $\omega\tau \approx 1$, resulting in lower quality loss data. To eliminate both of these factors our collaborators at Washington University, St. Louis are presently preparing a quasicrystalline sample of a similar (lower) concentration to that of the approximant phase we have already measured ($H / M = 0.20$). Secondly, the work was completed on the gas-flow system, with the samples at ambient pressures. Section 2.5 showed that by reducing the gas pressure about the sample, as can be done with the recently acquired Oxford Instruments ^{4}He cryostat, significant improvements to the quality of the loss measurements can be achieved. Experiments using the new system are already underway.

Additionally, it would also be very interesting to compare the effects of hydrogen on the temperature dependence and magnitude of the elastic constants of the QC and approximant phases, as was done with the Laves-phase system described in section 3.4. The work presented here provides a basis for these future studies.

REFERENCES

[1] C. Kittel, *Introduction to Solid State Physics*, (John Wiley and Sons, New York, 1967), p. 30.

[2] D. Shectman, I. Blech, D. Gratias, and J. W. Cahn, Phys. Rev. Lett. **53**, 1951 (1984).

[3] C. Jarnot, *Quasicrystals: a Primer* (Clarendon Press, Oxford, 1992).

[4] *Quasicrystals*, ed. by M. V. Jaric and S. Lunqvist (World Scientific, Singapore, 1990).

[5] Per Bak, Phys. Rev. B **32**, 5764 (1985).

[6] A. Yumamoto, Phys. Rev. B **45**, 5217 (1992).

[7] C. L. Henley, Phys. Rev. B **43**, 993 (1991).

[8] R. Penrose, *The Emperor's New Mind: Concerning Computers, Minds and the Laws of Physics*, (Oxford University Press, 1989).

[9] D. Levine and P. J. Steinhardt, Phys. Rev. B **34**, 596 (1986).

[10] P. S. Spoor, Ph. D. dissertation, unpublished (1997).

[11] A. M. Viano, R. M. Stroud, P. C. Gibbons, A. McDowell, M. S. Conradi and K. F. Kelton, Phys. Rev. B **51**, 12 026 (1995).

[12] A. I. Goldman and K. F. Kelton, Rev. Mod. Phys. **65**, 213 (1993).

[13] G. A. M. Reynolds, B. Golding, A. R. Kortan, and J. M. Parey, Jr., Phys. Rev. B **41**, 1194 (1990).

[14] S. Satish, A. Kulik, and G. Gremaud, Solid State Commun. **77**, 403 (1991).

[15] Y. Amazit, M. de Boissieu, and A. Zarembowitch, Eorphys. Lett. **20**, 703 (1992).

[16] P. S. Spoor, J. D. Maynard, and A. R. Kortan, Phys. Rev. Lett. **75**, 3462 (1995).

[17] Per Bak, Phys. Rev. Lett. **54**, 1517 (1985).

[18] M. A. Chernikov, H. R. Ott, A. Bianchi, A. Migliori, and T. W. Darling, Phys. Rev. Lett. **80**, 321 (1998).

[19] K. F. Kelton, in *Intermetallic Compounds: Principles and Practices*, edited by J. H. Westbrook and R. L. Fleischer (Wiley, New York, 1995), pp. 453-491.

[20] R. M. Stroud, A. M. Viano, P. C. Gibbons, and K. F. Kelton, Appl. Phys. Lett. **69**, 2998 (1996).

[21] K. F. Kelton, W. J. Kim, and R. M. Stroud, Appl. Phys. Lett. **70**, 3230 (1997).

[22] W. J. Kim, P.C. Gibbons, and K. F. Kelton, Philos. Mag. Lett. **76**, 199 (1997).

[23] W. J. Kim, P.C. Gibbons, K. F. Kelton, and W. B. Yelon, Phys. Rev. B **58**, 2578 (1998).

[24] Ch. Wälti, E. Felder, M. A. Cernikov, H. R. Ott, M. de Boissiewu, and C. Janot, Phys. Rev. B **57**, 10 504 (1998).

[25] I. Ohno, J. Phys. Earth **24**, 355 (1976).

[26] A. Migliori, J. L. Sarrao, W. M. Visscher, T. M. Bell, M. Lei, Z. Fisk, and R. G. Leisure, Physica B **183**, 1 (1993).

[27] A. Migliori and J. L Sarrao, *Resonant Ultrasound Spectroscopy* (Wiley, New York, 1997).

[28] R. G. Leisure and F. A. Willis, J. Phys.: Condens. Matter **9**, 6001 (1997).

[29] G. K. White, *Experimental Techniques in Low-Temperature Physics* (Clarendon, Oxford, 1968).

[30] G. Simmons and H. Wang, *Single Crystal Elastic Constants and Calculated Aggregate Properties* (M.I.T. Press, Cambridge, 1971).

[31] H. Ledbetter, *Dynamic Modulus Measurements* (ASTM, Philadelphia, 1990), pp. 135-148.

[32] N. W. Ashcroft and N. D. Mermin, *Solid State Physics* (Saunders, Philadelphia, 1976), p. 457.

[33] A. D. Bianchi, F. Bommeli, E. Felder. M. Kenzelmann, M. A. Chernikov, L. Degiorgi, H. R. Ott, and K. Edagawa, Phys. Rev. B **58**, 3046 (1998).

[34] Y. Fukai, 1993 *The Hydrogen-Metal System* (Berlin: Springer-Verlag).

[35] W. Renz, G. Majer, A. V. Skripov and A. Seeger, J. Phys.: Condens. Matter **6**, 6367 (1994).

[36] A. V. Skripov, M. Yu. Belyaev, S. V. Rychkova and A. P. Stepanov, J. Phys.: Condens. Matter **1**, 2121 (1989).

[37] A. V. Skripov, J. C. Cook, D. S. Sibirtsev and R. Hemplemann, J. Phys.: Condens. Matter **10**, 1787 (1997).

[38] K. Foster, R. G. Leisure and A. V. Skripov, J. Phys.: Condens. Matter **11**, 799 (1999).

[39] D. R. Nelson and F. Spaepen, Solid State Phys. **42**, 1 (1989).

[40] J. C. Holzer and K. F. Kelton, in *Crystal-Quasicrystal Transitions*, edited by M. J. Yacaman and M. Torres (North-Holland, Amsterdam, 1993), p. 103.

[41] G. Coddens, A. M. Viano, P. C. Gibbons, K. F. Kelton and M. J. Kramer, Solid State Commun. **104**, 179 (1997).

[42] A. M. Viano, A. F. McDowell, M. S. Conradi, P. C. Gibbons and K. F. Kelton, in *Proceedings of the Fifth International Conference on Quasicrystals*, edited by C. Janot and R. Mosseri (World Scientific, Singapore, 1995), p. 798.

[43] A. Shastri, E. H. Majoub, F. Borsa, P. C. Gibbons and K. F. Kelton, Phys. Rev. B **57**, 5148 (1998).

[44] L. A. Nygren and R. G. Leisure, Phys. Rev. B **39**, 7611 (1989).

[45] R. G. Leisure, R. B. Schwarz, A. Migliori, D. R. Torgeson and I. Svare, Phys. Rev. B **48**, 893 (1993).

[46] H. Zhang, R. S. Sorbello, C. Hucho, J. Herro, J. R. Feller, D. E. Beck, M. Levy, D. Isaak, J. D. Carnes and O. Anderson, J. Acoust. Soc. Am. **103**, 2385 (1998).

[47] A. S. Nowick and B. S. Berry, *Anelastic Relaxation in Crystalline Solids* (Academic, New York, 1972).

[48] J. Y. Kim, E. Majzoub, P. C. Gibbons and K. F. Kelton, in *Quasicrystals*, edited by J.-M Dubois, P. A. Thiel, A.-P Tsai, and K. Urban, MRS Symposia Proceedings No. 553 (Materials Research Society, Pittsburgh, 1998). P. 483.

[49] U. Stoltz, M. Weller and R. Kirchheim, Scr. Metall. **20**, 1361 (1986).

Chapter 5

Acoustic Study of Texture in Polycrystalline Brass

- **5.1 Introduction**
- **5.2 Theoretical Background**
- **5.3 Experimental Details**
- **5.4 Results and Discussion**
- **5.5 Conclusions**
- **References**

5.1 Introduction

The elastic constants of single crystals reflect the symmetry of the crystalline lattice. For materials with cubic symmetry, only three independent elastic constants are necessary to fully describe the linear elasticity. The number of independent elastic constants required increases as the symmetry of a particular system decreases, e.g., nine elastic constants are required for crystals of orthorhombic symmetry [1]. In contrast, polycrystalline materials are often assumed to be elastically isotropic, thus requiring just two independent elastic constants to describe their elasticity. Elastic isotropy results in polycrystalline aggregates when the polycrystalline grains are small compared to the length scale of the experiment and are randomly orientated within the sample. However, in many materials of practical interest a non-random distribution of the grain orientations may occur. This situation can arise as a result of various mechanical processing and / or heat

treatments. Such preferred orientation, called texture, results in elastic anisotropy of polycrystalline aggregates. Texture can have significant practical implications on the formability, ductility and non-destructive testing of polycrystalline materials. In principle, any physical-mechanical property not representable by a scalar depends on an aggregate's texture. Texture has been described theoretically [2][3][4] in terms of an orientation distribution function (ODF) w, where $w(\xi,\psi,\phi)d\xi d\psi d\phi$ is the probability of finding crystallites with orientations between (θ,ψ,ϕ) and $(\theta+d\theta,\psi+d\psi,\phi+d\phi)$. Here $\xi=\cos\theta$, and θ,ψ and ϕ are the Euler angles [4] denoting the orientation of the crystallite axes with respect to the specimen axes. The orientation-distribution function may be expanded in terms of generalized spherical harmonics. The expansion coefficients W_{lmn} are called orientation distribution coefficients (ODCs). Detailed information about the ODCs can be obtained from both x-ray diffraction and neutron scattering experiments: however, these techniques are not always ideally suited, or convenient, for non-destructive testing or process control. As a result, there is an interest in using ultrasonic techniques to provide information about texture in polycrystalline materials [5][6][7][8][9]. The effects of texture on the propagation of Rayleigh-waves and Lamb-waves have been studied [7][9] in the past but the interpretation was complicated due to dispersive effects associated with Rayleigh and Lamb-wave propagation in plates. Some of the ODCs have also been obtained from acoustic shear-wave birefringence measurements [6][8].

The objective of this study was to apply the technique of resonant ultrasound

spectroscopy (RUS) to the investigation of anisotropic elasticity in textured materials and to compare the results to theoretical expressions previously derived [5][7][9]. Measurements were made on rolled polycrystalline plates of Cu, Cu-5 % Zn and Cu-15 % Zn. The ultrasonically derived results are compared to neutron diffraction measurements on the same set of alloys.

5.2 Theoretical Background

5.2.1 Anisotropic elasticity and ODCs

The effects of texture on rolled plates were studied. It is generally assumed that the macroscopic properties of rolled-plates possess three mutually perpendicular mirror planes. Thus, the resulting elastic-constant matrix is expected to exhibit orthorhombic symmetry, requiring nine independent components [7]. The chosen co-ordinate system is illustrated in figure 5.1, where x_1, x_2 and x_3 refer to the plate-rolling, -transverse and -normal directions, respectively. X_1, X_2 and X_3 designate the principle-axis system of a crystallite within the aggregate. The Euler angles give the orientation of (X_1, X_2, X_3) with respect to (x_1, x_2, x_3) [7]. It is straightforward to transform the elastic-constant matrix from the crystallite co-ordinate system to the specimen co-ordinate system [1]. The results obviously depend on the symmetry and orientation of the crystallite with respect to the specimen. To obtain the aggregate results, the transformed elastic constants are averaged over all possible orientations using the ODCs described above. For the case of crystallites with cubic symmetry and a specimen of orthorhombic symmetry the results for the aggregate elastic constants are given by **Eqs.** (1) [7][9].

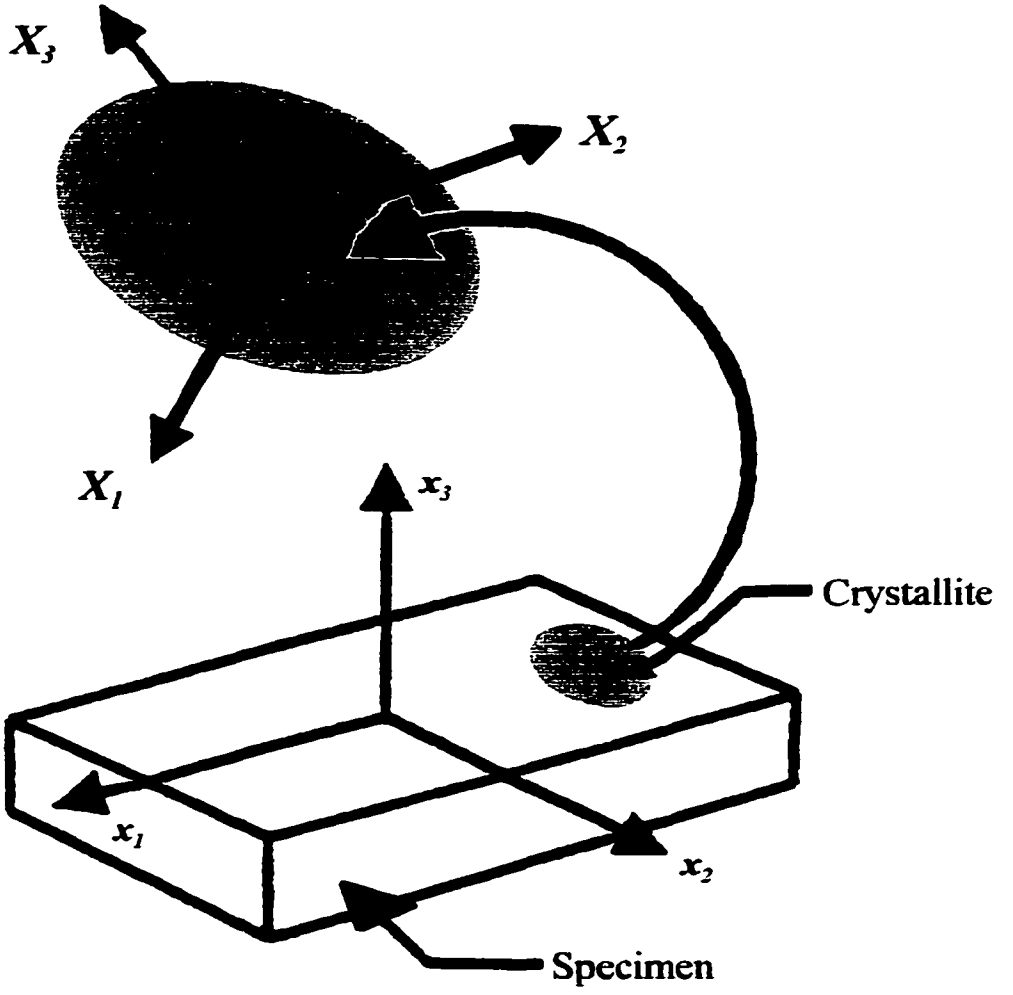

Figure 5.1: The coordinate systems used to describe the rolled plate specimen (x_1,x_2,x_3) and a crystallite in the sample (X_1,X_2,X_3). For the specimen, x_1 = rolling direction, x_2 = plate-transverse direction, and x_3 = plate normal direction.

$$
\begin{aligned}
C_{11} &= \lambda + 2\mu + \left(\frac{12\sqrt{2}c\pi^2}{35}\right)\left[W_{400} - \left(\frac{2\sqrt{10}}{3}\right)W_{420} + \left(\frac{\sqrt{70}}{3}\right)W_{440}\right] \\
C_{22} &= \lambda + 2\mu + \left(\frac{12\sqrt{2}c\pi^2}{35}\right)\left[W_{400} + \left(\frac{2\sqrt{10}}{3}\right)W_{420} + \left(\frac{\sqrt{70}}{3}\right)W_{440}\right] \\
C_{33} &= \lambda + 2\mu + \left(\frac{32\sqrt{2}c\pi^2}{35}\right)W_{400} \\
C_{44} &= \mu - \left(\frac{16\sqrt{2}c\pi^2}{35}\right)\left[W_{400} + \sqrt{\frac{5}{2}}W_{420}\right] \\
C_{55} &= \mu - \left(\frac{16\sqrt{2}c\pi^2}{35}\right)\left[W_{400} - \sqrt{\frac{5}{2}}W_{420}\right] \\
C_{66} &= \mu + \left(\frac{4\sqrt{2}c\pi^2}{35}\right)\left[W_{400} - \sqrt{70}W_{440}\right] \\
C_{12} &= \lambda + \left(\frac{4\sqrt{2}c\pi^2}{35}\right)\left[W_{400} - \sqrt{70}W_{440}\right] \\
C_{13} &= \lambda - \left(\frac{16\sqrt{2}c\pi^2}{35}\right)\left[W_{400} - \sqrt{\frac{5}{2}}W_{420}\right] \\
C_{23} &= \lambda - \left(\frac{16\sqrt{2}c\pi^2}{35}\right)\left[W_{400} + \sqrt{\frac{5}{2}}W_{420}\right]
\end{aligned}
\tag{1}
$$

where λ and μ are the Lamé constants for the texture free material, and c is an anisotropy parameter for the crystallite. Different averaging methods (Voigt, Ruess, Hill, others) are reflected only in the values of λ, μ and c: the ODCs contribute in the same way for each method. In principle λ, μ and c can be determined from the single-crystal elastic constants using one of these averaging methods. For copper, Ledbetter [10] compared nine averaging methods and found that Kröner's method gives the best measurement to theory agreement. The absolute value of c depends on the chosen averaging scheme. For Copper, the Voigt, Hill and Reuss averaging schemes give c = -104.4, -99.0 and -94.0 GPa, respectively. The Kröner value falls between the Hill and Voigt results. Thus a

difference in c of around 2 % would produce no significant effect on the results and conclusions presented. The problem of choosing an averaging method for λ and μ was avoided in the present work by measuring all nine elastic constants for the textured plates, and fitting **Eqs.** (1) to the results to obtain the five parameters λ, μ, W_{400}, W_{420} and W_{440}. As can be seen from **Eqs.** (1), c always appears as a multiplier of the ODCs so cannot be determined independently from these experiments. Therefore, c was calculated from single-crystal c_{ij}

using the usual anisotropy relationship $c = c_{11} - c_{12} - 2c_{44}$, where the c_{ij} are the single-crystal values [11]. These results are presented in table 5.1.

Table 5.1: Single-crystal elastic constant data for copper-zinc alloys [11] used to compute the anisotropy parameter c (also given).

Material	c_{11} (GPa)	c_{12} (GPa)	c_{44} (GPa)	c (GPa)
Copper (100%)	168.4	121.4	75.5	-104.4
Copper (95.9%)-Zinc(4.1%)	163.2	117.6	74.4	-103.2
Copper (82.9%)-Zinc(17.1%)	149.9	109.7	71.5	-102.8

The relative values of the ODCs will not be affected by the choice of c. In our experience, the laboratory-laboratory variation in measured c_{ij} is about 1 in 10^3, thus insignificant for present purposes.

5.2.2 Acoustic pole plots

It is convenient to describe the orientation of the crystallites in terms of a distribution function for reciprocal-lattice vectors. Figure 5.2 illustrates the situation for a particular reciprocal-lattice vector $\mathbf{t}_i$. The orientation of $\mathbf{t}_i$ in the crystallite co-ordinate system is specified by the angles Θ_i and Φ_i. For example, these angles are $\pi / 2$ and $\pi / 4$, respectively for a [110] reciprocal-lattice vector. This vector is specified by the angles χ_i and η_i in the *plate* co-ordinate system. Let $q_i(\zeta,\eta)d\zeta d\eta$ be the probability of finding $\mathbf{t}_i$ between (χ,η) and $(\chi+d\chi,\eta+d\eta)$ where $\zeta=\cos(\chi)$. It has been shown [5][7] that

$$q_i(\zeta,\eta)=\frac{1}{4\pi}+S(\Xi_i,\Phi_i)\left[P_4^0(\zeta)W_{400}+2P_4^2(\zeta)\cos(2\eta)W_{420}+2P_4^4(\zeta)\cos(4\eta)W_{440}\right]$$

$$+\text{ higher order terms,} \qquad (2)$$

where

$$S(\Xi_i,\Phi_i)=\frac{2\sqrt{2\pi}}{3}\left[P_4^0(\Xi_i)+\frac{10}{\sqrt{70}}P_4^4(\Xi_i)\cos(4\Phi_i)\right] \qquad (3)$$

with $\Xi_i=\cos(\Theta_i)$. The $P_l^m(z)$ are the normalized associated Legendre functions. It is convenient to display the information about the distribution of reciprocal lattice vectors as pole plots, which are projections of $4\pi q_i(\zeta,\eta)$ onto the x_1 - x_2 plane. Typical pole figures obtained from neutron diffraction measurements are presented in figure 5.3.

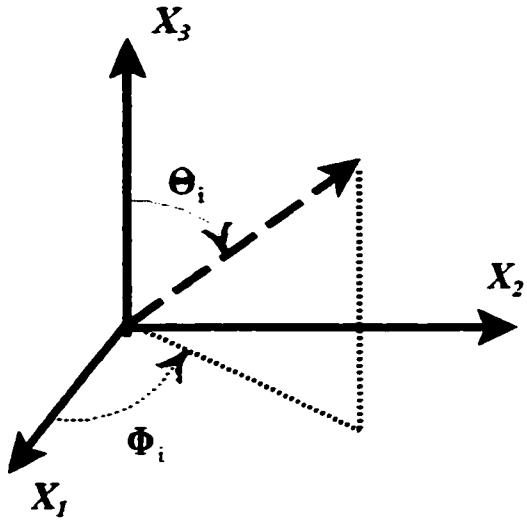

(a)

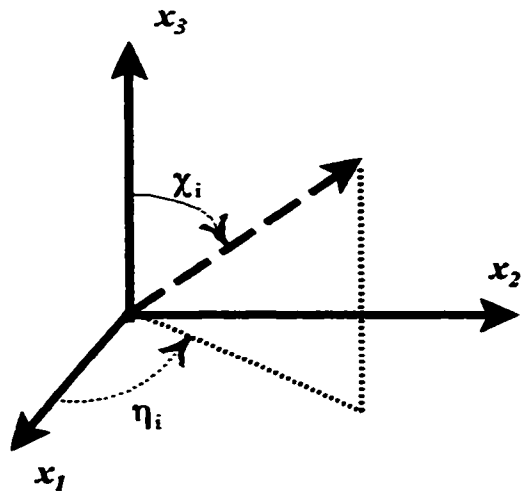

(b)

Figure 5.2: The angles used to describe the orientation of a particular reciprocal lattice vector t_i in a crystallite (a) and in the rolled-plate (b).

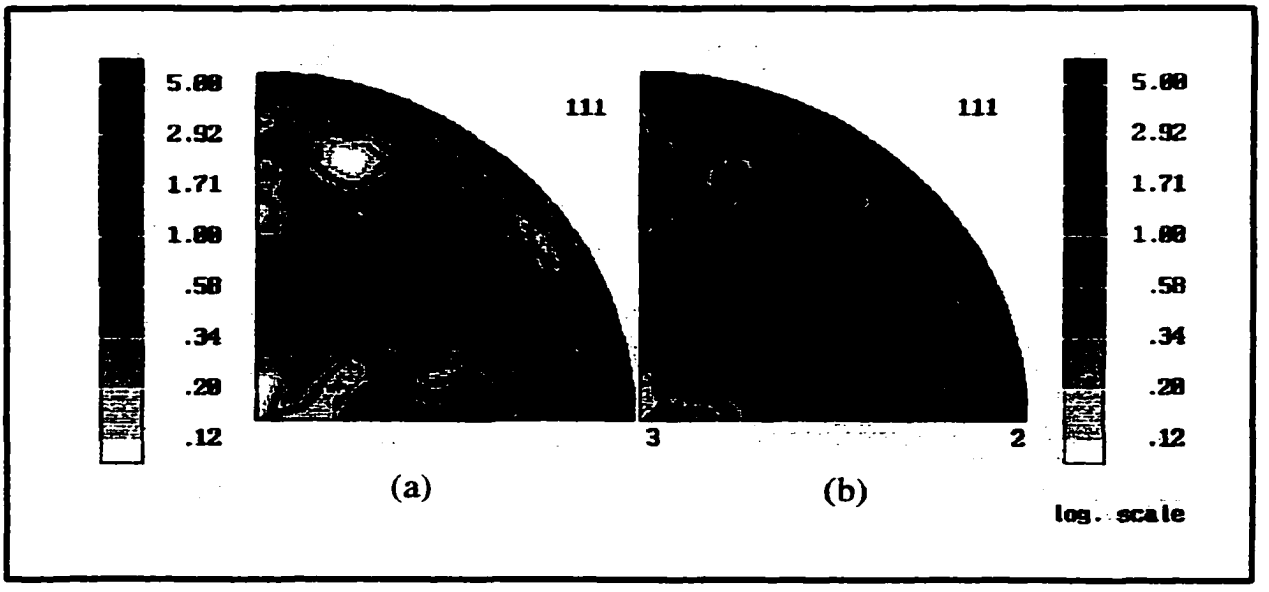

Figure 5.3: [111] pole figures were obtained from time-of-flight neutron-diffraction measurements at the High Intensity Powder Diffractometer at the Manuel Lujan Jr. Neutron Scattering Center at Los Alamos National Laboratory: (a) Cu - 5% Zn; (b) Cu - 15% Zn. (Neutron measurements made by D. Balzar, *Materials Science and Engineering Laboratory, NIST, Boulder, CO 80303.*)

5.3 Experimental Details

The study was carried out on Olin Corporation copper and copper-zinc alloys (brass) in collaboration with a group from the Materials Science and Engineering Laboratory Division of NIST, Boulder, Colorado. The specimens used for the study were cut using a low-speed diamond saw from 3.17-mm-thick plates. Three types of material were studied: Olin type 110 copper containing 0.021-wt. % oxygen; Olin type 210 copper-5 % zinc alloy: and Olin type 230 copper-15 % zinc alloy. The crystallites within the alloys have the same crystal structure as copper: face-centered cubic. Copper dissolves zinc substitutionally up to approximately 40 %. Optical microstructures taken at NIST revealed that the grain morphology was reasonably uniform throughout the thickness of the plates. The grain size was roughly 0.01 mm in the 110 and 210 materials, and somewhat smaller in the 230 material. The Cu-5 % Zn alloy appeared to have been heavily deformed. The microstructure strongly suggests (but not conclusively) the presence of strong texture in this material; microstructural evidence for texture was less obvious for the Cu and Cu-15 % Zn alloys. The neutron-diffraction pole figures (figure 5.3) confirm this. From these measurements the texture index [12] was determined as 4.7 and 1.6 for the Cu-5 % Zn and Cu-15 % Zn alloys respectively.

Room temperature elastic-constant measurements were carried out both at Colorado State University and at NIST. Measurements on a number of specimens of each type of material were performed at CSU using Resonant Ultrasound Spectroscopy [13][14][15]. The samples varied somewhat in size, but each was an accurate rectangular parallelepiped typically 1.5 - 2.5 mm on an edge. The specimen axes were aligned with

the original plates axes so as to maintain the orthorhombic symmetry. Specimen dimensions were measured to an accuracy of 0.1 % or better. The sample preparation procedures were described [14] in section 2.2. The elastic constants were determined in the usual way from the measured frequencies by an iterative procedure [14]. The root-mean-square (rms) difference between the measured and computed frequencies for the first 50 modes was excellent, at 0.1 % - 0.2 %. In addition to the resonance measurements, elastic constants for all three materials were measured at NIST using a pulse-echo method and a Marx-oscillator technique [16]. Densities were determined by the Archimedes method at NIST, using distilled water as a standard. There is a typical uncertainty in the density of about 5 in 10^4 for the specimen sizes used here.

5.4 Results and Discussion

Table 5.2 presents the results for the orthorhombic elastic constants from a large number of measurements on the Cu-*x* % Zn system. The "±" in table 5.2 indicates the standard deviation of the measurements as a percentage of the mean value.

If there were no preferred orientation (no texture) then, as **Eqs.** (1) shows, we would expect: $C_{11} = C_{22} = C_{33}$; $C_{44} = C_{55} = C_{66}$; $C_{12} = C_{13} = C_{23}$; and $C_{44} = 1/2(C_{11} - C_{12})$. By these measures, an inspection of table 5.2 shows that the Cu-5 % Zn material is the most anisotropic, while the Cu has the smallest anisotropy. These observations agree with the microstructural analysis and the neutron-diffraction pole figures. Figure 5.3 shows the [111] neutron-diffraction pole figure as this geometry is

used most regularly for interpretation purposes.

Table 5.2: Orthorhombic elastic constants for Cu-x % Zn alloys. The '±' indicates the standard deviation of the measurement as a percentage of the mean.

x	0	5%	15%
C_{11} (GPa)	201.2 ± 0.59%	203.3 ± 0.38%	193.6 ± 0.72%
C_{22} (GPa)	201.0 ± 0.39%	200.8 ± 1.53%	191.8 ± 0.10%
C_{33} (GPa)	199.4 ± 1.38%	196.0 ± 0.32%	191.2 ± 0.34%
C_{44} (GPa)	45.50 ± 0.12%	41.84 ± 0.33%	46.80 ± 0.02%
C_{55} (GPa)	45.79 ± 0.25%	45.30 ± 0.21%	44.39 ± 0.03%
C_{66} (GPa)	45.43 ± 0.24%	44.12 ± 3.24%	43.63 ± 0.00%
C_{23} (GPa)	110.2 ± 0.04%	101.9 ± 3.94%	102.5 ± 1.41%
C_{13} (GPa)	111.2 ± 2.42%	104.8 ± 1.09%	100.2 ± 0.67%
C_{12} (GPa)	109.6 ± 1.71%	99.53 ± 1.57%	101.0 ± 0.00%
ρ (g/cm^3)	8.903 ± 0.05%	8.852 ± 0.05%	8.730 ± 0.05%

For a more detailed comparison of the experimental results with the theoretical expressions we performed a least-squares fit of the data of table 5.2 to the theoretical expressions of **Eqs.** (1) to determine the five parameters $W_{400}, W_{420}, W_{440}, \lambda$ and μ. For the parameter c we used the values listed in table 5.1. The results of this fitting are presented in table 5.3. The 'rms error' is the root-mean-square difference between the measured elastic constants and those calculated by **Eqs.** (1) using the parameters of table 5.3. The derived ODCs indicate that Cu-5 % Zn is significantly more anisotropic than the

other materials, in qualitative agreement with the microstructure and neutron diffraction pole figures. Table 5.3 also lists the W's determined from neutron-diffraction measurements on the same alloys. It can be seen that the ultrasonic and neutron values are in reasonable agreement.

Figure 5.4 presents a comparison of the measured to the computed C_{ij} using the parameters presented in table 5.3. The two sets of values agree well with one another, except for C_{11} and C_{33} for the Cu-5 % Zn material. To further explore the comparison of theory and measurement we note that **Eqs.** (1) indicate various relationships amongst the elastic constants. For example, it is expected that $C_{11} - C_{22} = C_{44} - C_{55} = C_{23} - C_{13}$. For an isotropic material these numbers would all be equal to zero. The experimental numbers for these three quantities are, respectively (in GPa): (Cu) +0.2, -0.29, -1.0; (Cu-5 % Zn) +7.3, -3.46, -2.95; (Cu-15 % Zn) +1.80, +2.41, +2.27. These numbers are all in excellent agreement with the theoretical expressions *except* for the value of $C_{11} - C_{22}$ for the Cu-5 % Zn alloy. It can also be seen that the Cu material is the most nearly isotropic, while the Cu-5 % Zn material is the most anisotropic. The discrepancy of $C_{11} - C_{22}$ for the Cu-5 % Zn alloy possibly suggests departures from the assumed orthorhombic symmetry.

For a visual comparison of the ODCs determined acoustically with the low-order W's derived from the neutron diffraction measurements, we turn to the pole plots. Figures 5.5 and 5.6 are contour plots of $4\pi q_i(\zeta, \eta)$ for the [100] reciprocal-lattice vector

(a)

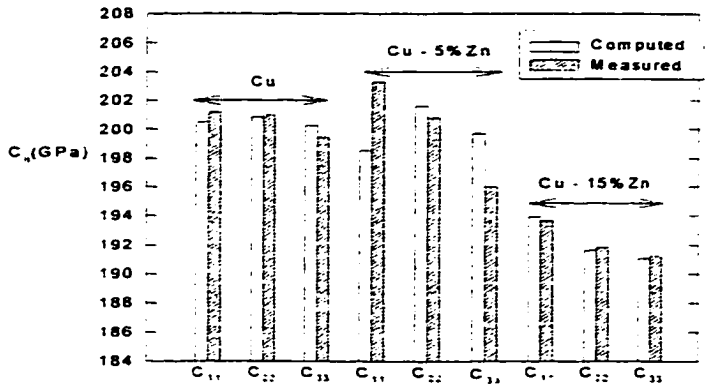

(b)

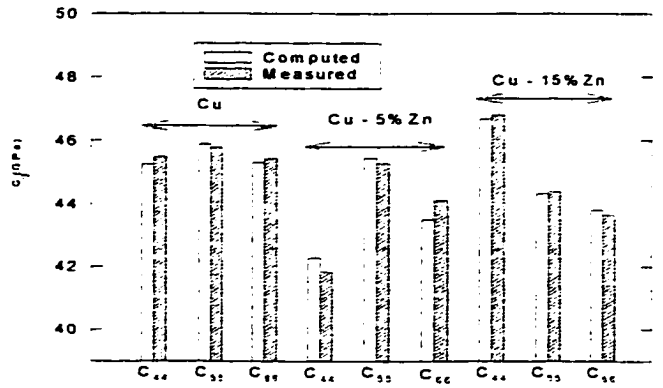

(c)

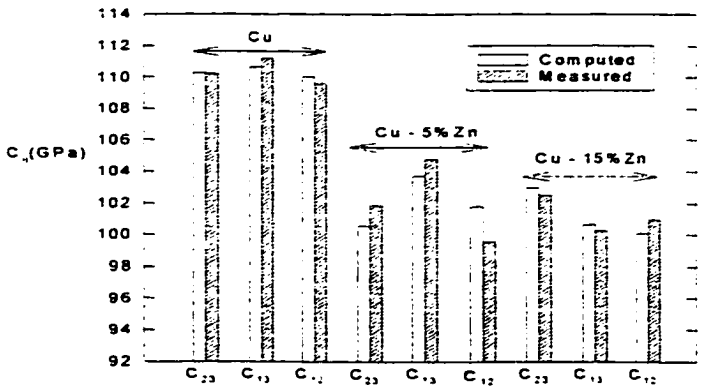

Figure 5.4: Comparison of measured and computed values of the elastic constants (a) C_{11}, C_{22} and C_{33}, (b) C_{44}, C_{55} and C_{66}, (c) C_{23}, C_{13} and C_{12}, for Cu, and two Cu-Zn alloys. The computations used the parameters of table 5.2.

projected onto the x_1-x_2 plane for the Cu-15 % Zn and Cu-5 % Zn alloys respectively.

Table 5.3: ODCs (W's) and Lamé contants (λ and μ) for Cu-x % Zn alloys obtained by fitting the experimental results of table 5.2 to **Eqs.** (1). Also listed are the ODCs obtained from neutron-diffraction measurements for the 5 % and 15 % Zn material.

x	0	5 % Ultrasound	5 % Neutron	15 % Ultrasound	15 % Neutron
W_{400}	$4.93*10^{-4}$	$-2.98*10^{-3}$	$-1.73*10^{-3}$	$5.34*10^{-4}$	$9.95*10^{-5}$
W_{420}	$-1.76*10^{-4}$	$-1.53*10^{-3}$	$-1.91*10^{-3}$	$1.14*10^{-4}$	$9.77*10^{-4}$
W_{440}	$6.72*10^{-6}$	$-2.05*10^{-3}$	$-3.17*10^{-4}$	$-9.18*10^{-4}$	$-8.44*10^{-4}$
λ (GPa)	110.1	104.1	n/a	101.5	n/a
μ (GPa)	45.38	45.83	n/a	45.15	n/a
rms	0.31%	1.5%	n/a	0.39%	n/a

These pole figures are constructed using only the lower order Ws. The ultrasonically derived pole plots are shown in figures 5.5 (a) and 5.6 (a) and those from the neutron measurements in figures 5.5 (b) and 5.6 (b). Light and dark colors represent high and low intensity respectively. It is clear from figure 5.5, to the resolution presented, that the two plots are almost identical for the Cu-15 % Zn alloy. The quantity $4\pi q_{[100]}(\zeta,\eta)$ has a maximum value in the plane of the plate at approximately 50° to the rolling direction. The maximum (minimum) values of $4\pi q_{[100]}(\zeta,\eta)$ are 1.21 (0.74) for the ultrasonic results and 1.17 (0.80) for the neutron results. A value of unity corresponds

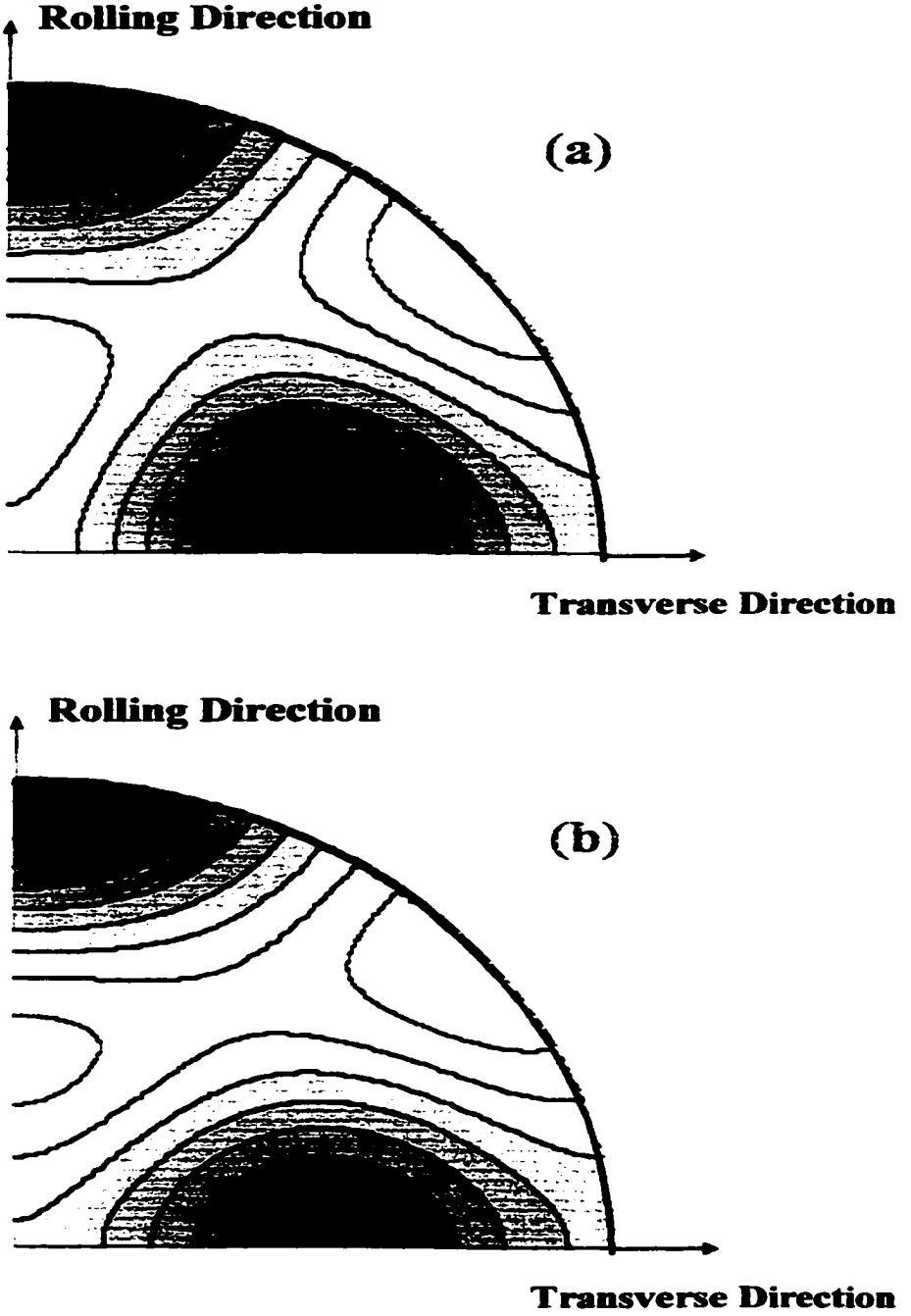

Figure 5.5: [100] pole plots for the Cu-15% Zn material. Light (dark) represents high (low) intensity. (a) Derived from acoustic measurements. The intensity ranges from 0.74 to 1.21. (b) Derived from neutron measurements. The intensity ranges from 0.80 to 1.17.

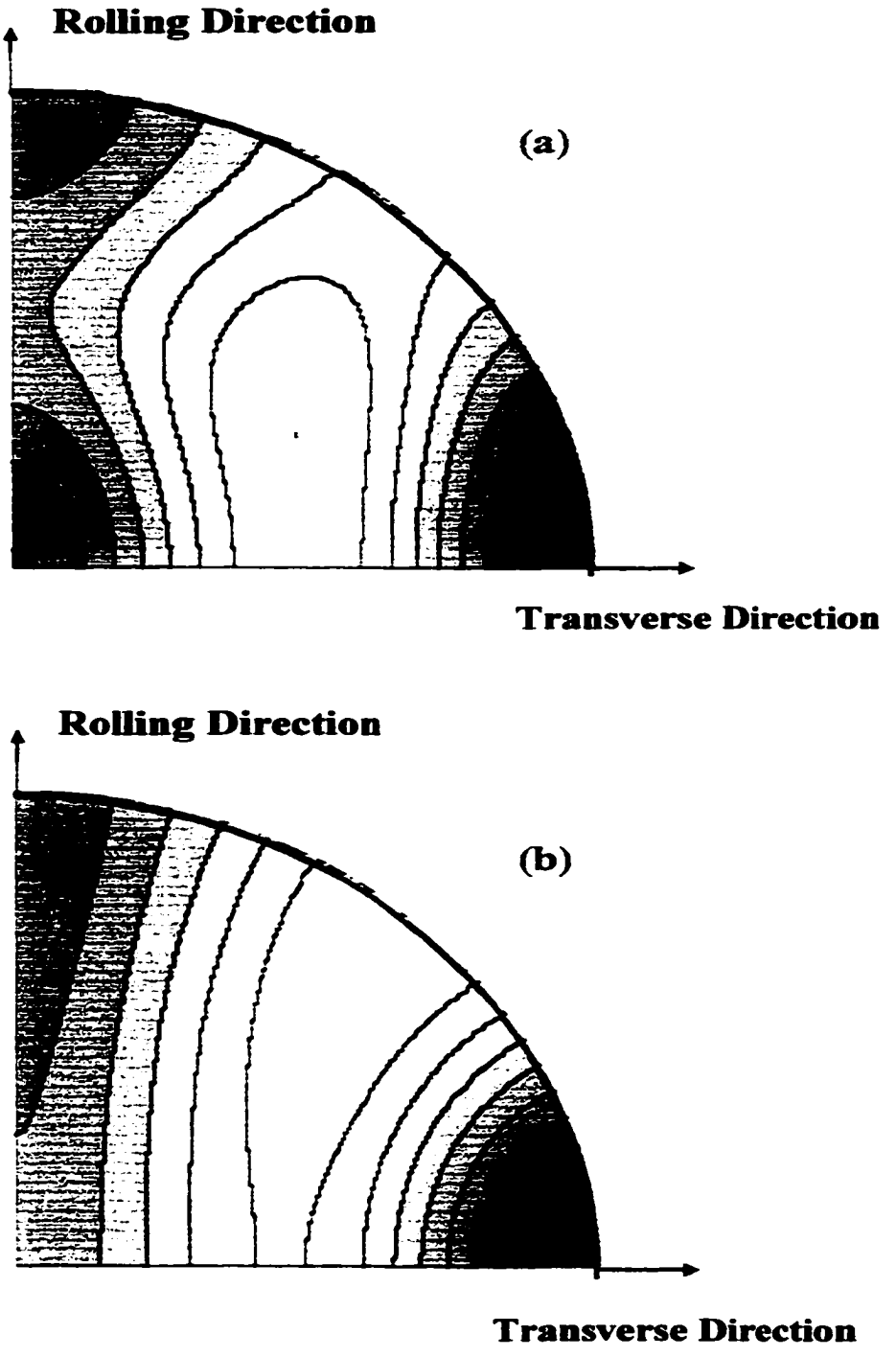

Figure 5.6: [100] pole plots for the Cu-5% Zn material. Light (dark) represents high (low) intensity. (a) Derived from acoustic measurements. The intensity ranges from 0.25 to1.39. (b) Derived from neutron measurements. The intensity ranges from 0.08 to 1.46.

to an isotropic distribution. Although the ultrasonic and neutron results are qualitatively similar for the Cu-5 % Zn alloy as shown in figure 5.6, the correspondence is not as good as that shown in figure 5.5. The maximum (minimum) values in figure 5.6 are 1.39 (0.25) for the ultrasonic results and 1.46 (0.08) for the neutron results.

Previous workers [6][8] have compared ultrasonic and neutron results for W_{420} and W_{440}. The present agreement between the neutron-derived and acoustic-derived results is comparable to that found previously. Ultrasonic methods are often unable to determine W_{400} with high accuracy. As has been discussed by Hirao *et al.* [7], the ultrasonic result for W_{400} is critically dependent on the averaging scheme used to compute the isotropic parameters, λ, μ and c from the single crystal data. Our method is different: we compute only the anisotropy parameter *c* from the single crystal data, *and* the results are not critically dependent on *c*.

Comparison of the acoustic and neutron-diffraction ODFs in figures 5.5 and 5.6 deserves additional discussion. These pole figures are constructed using only lower-order ODF coefficients W_{400}, W_{420} and W_{440}. As such, they clearly do not represent the complete pole figures. For example, the measured neutron-diffraction [111] pole figures (figure 5.3) show considerably more detail than the pole plots of figures 5.5 (b) and 5.6 (b). Nevertheless, in terms of the effect of the ODF on the overall physical and mechanical properties of polycrystals, the low-order ODF coefficients play the leading role. In fact, for tensorial properties, only the low-order ODF coefficients come into play. This result, known as the truncation theorem, [12][17] is evident in Eqs. (1) where only

those ODCs through order four enter the averaging of the elastic constants, which are fourth-rank tensors. Likewise, for the second-rank tensorial properties such as thermal expansion and thermal conductivity, only ODCs through order 2 enter the averaging process.

5.4 Conclusions

Acoustic methods have been used to obtain the elastic constants of rolled plates of Cu, Cu-5 % Zn and Cu-15 % Zn polycrystalline materials. It was assumed that the macroscopic properties of the rolled plates have orthorhombic symmetry. The experimental results were compared to theoretical expressions to obtain the ODCs. The results for the Cu-15 % Zn material showed considerable elastic anisotropy. The results were in good agreement with the theoretical expressions, and the ODCs were in good agreement with neutron measurements for W_{400}, W_{420} and W_{440}. The acoustic and neutron pole plots for W_{ijk} through order 4 were almost identical. The ultrasonic results indicated that the Cu-5 % Zn material is the most anisotropic, in qualitative agreement with microstructures; however, the agreement between theory and measurement was not as good for this material, especially for C_{11} and C_{22}. The reasons for this disagreement are not known; perhaps this material possesses less than orthorhombic macroscopic symmetry, which would then require additional W_{ijk}. The analysis was based, of course, on orthorhombic symmetry, the usual assumed symmetry for a rolled plate. One can imagine rolled plates with less than orthorhombic symmetry because of non-homogeneous

deformation, for example. Nevertheless, the acoustic and neutron plots for this material were in qualitative agreement. Overall, the results presented here certainly support the idea that ultrasonic measurements may be used for quantitative texture corrections of tensorial physical quantities.

REFERENCES

[1] F. I. Fedorov, *Theory of Elastic Waves in Crystals* (Plenum, New York, 1968).

[2] R.-J. Roe and W. R. Krigbaum, J. Chem. Phys. **40**, 2608 (1964).

[3] R.-J, Roe, J. Appl. Phys. **36**, 2024 (1965).

[4] R.-J, Roe, J. Appl. Phys. **37**, 2069 (1966).

[5] C. M. Sayers, J. Phys. D **15**, 2157 (1982).

[6] C. M. Sayers, D. R. Allen, G. E. Haines, and G. G. Proudfoot, Philos. Tran. R. Soc. London, Ser. A **320**, 187 (1986).

[7] M. Hirao, K. Aoki, and H. Fukuoka, J. Acoust. Soc. Am. **81**, 1434 (1987).

[8] A. V. Clarke, Jr., R. C. Reno, R. B. Thompson, J. F. Smith, G. V. Blessing, R. J. Fields, P. P. Delsanto, and R. B. Mignogna, Ultrasonics **26**, 189 (1988).

[9] Y. Lee and R. B. Thompson, J. Acoust. Soc. Am. **91**, 1298 (1992).

[10] H. Ledbetter, in *Dynamic Modulus Measurements* (ASTM, Philadelphia), pp. 135-148 (1990).

[11] J. A. Rayne, Phys. Rev. **112**, 1125 (1958).

[12] H. Bunge, *Texture Analysis in Materials Science* (Butterworths, London, 1982).

[13] A. Migliori, J. L. Sarrao, W. M. Visscher, T. M. Bell, Ming Lei, Z. Fisk, and R.G. Leisure, Physica B **183**, 1 (1993).

[14] A. Migliori and J. L. Sarrao, *Resonant Ultrasound Spectroscopy* (Wiley, New York, 1997).

[15] R. G. Leisure and F. A. Willis, J. Phys.: Conden. Matter **9**, 6001 (1997).

[16] H. Ledbetter, Cryogenics 20, **637** (1980).

[17] M. Ferrari and G. Johnson, Mech. Mater. **8**, 67 (1989).

Chapter 6

Conclusions

The novel technique of Resonant Ultrasound Spectroscopy (RUS) has successfully been applied to the study of the elastic properties of three quite different physical systems. The results reported in this thesis would have been extremely difficult to obtain using more conventional acoustic techniques. The use of RUS, particularly in measuring the ultrasonic loss of hydrogenated intermetallic and quasicrystalline systems has been extended.

The elastic moduli and the ultrasonic loss of a C15 Laves-phase intermetallic compound, TaV_2H_x, were measured over a temperature range of 2.8 - 350 K. Compounds of various hydrogen (H) concentrations, $x = 0.00$, 0.06, 0.10, 0.18, 0.34 and 0.53 were examined. The compounds form single-phase solid solutions of hydrogen and maintain the cubic C15 structure down to low temperatures. Hydrogen sits on the g-type interstitial sites, which from a series of interlinked pentagons and hexagons. Large ultrasonic loss peaks centered at roughly 240 K were observed for all hydrogenated compounds for measurement frequencies of about 1 MHz. Shifts in the resonant frequencies of the modes were also observed in the same temperature region. Both the loss and dispersive effects were associated with the long-range motion of hydrogen from hexagon to hexagon. Parameters of the hydrogen motion, including activation energies,

attempt frequencies and relaxation strengths were derived from these data. The values of the activation energies and the attempt frequencies were in good agreement with those determined from nuclear magnetic resonance measurements. The relaxation rates for $x \leq 0.18$ were best described as a sum of two Arrhenius processes which were interpreted as phonon-assisted tunneling between ground states and between excited states. For $x = 0.34$ and 0.53 only a single Arrhenius process was needed to fit the results, although the two-Arrhenius mechanism could not be ruled out from these measurements over the given temperature range. The magnitude of the effects depended linearly on the hydrogen concentration, implying that it is the relaxation of isolated H atoms that is contributing to the mechanical damping; these results appear to be the very first which clearly demonstrate the existence of the Snoek effect in intermetallic-hydrides.

Similar measurements were made on the related compound, $TaV_2D_{0.17}$ and the results compared directly to those of $TaV_2H_{0.18}$. The $TaV_2D_{0.17}$ alloy showed a similar attenuation peak centered at about 240 K which was interpreted in the same way as those of the hydrogenated compounds. A weak isotope effect was observed with the H hopping rate being somewhat faster than that for the D. Interestingly, a second, much weaker attenuation peak centered at approximately 20 K was observed for the deuterated compound, but was completely absent in the loss data for $TaV_2H_{0.18}$. This peak was attributed to a much more rapid localized motion of D atoms, *within* g-site hexagons. The large isotope effect observed at low temperatures implies that this local motion is dominated by quantum processes. The absence of the peak in the hydrogenated sample is probably due to the fact that the local motion is occurring at rates above the ultrasonic

frequency. The low-temperature peaks were not fit to a theoretical expression. The fast local motion of H(D) at low-temperatures has only been observed for a handful of metal-hydride systems and is not particularly well understood. This work provided a clear demonstration of a strong isotope effect in a metal-hydride system. Unlike the NMR results, the peaks attributed to the two frequency scales of D motion were separately resolved in temperature. These results will hopefully aid in further developing a picture of quantum-mechanical tunneling in metal-hydrides.

The magnitude and temperature dependence of the shear elastic modulus, $G(T)$, of the $TaV_2H(D)_x$ system was found to be highly dependent on the H(D) concentration, x. $G(T)$ of TaV_2 anomalously increased with increasing temperature from 3 K to 350 K. The effect of adding hydrogen was both to systematically increase the magnitude of $G(T)$ and to completely reverse the temperature dependence for all $x \geq 0.18$. A minimum in $G(T)$ was observed for $TaV_2H_{0.10}$ at roughly 40 K. $G(T)$ of $TaV_2H_{0.53}$ was 55 % greater than that of the H free material at 20 K. This is a much stronger effect on the magnitude of the elastic constants than is observed for most metal-hydrides. Both the magnitude and temperature dependent effects were described quantitatively in terms of an electronic band structure model. The position of the Fermi level relative to doubly-degenerate electronic levels at the X-point of the Brillouin zone is the key parameter of the model. If the Fermi level lies close to this point, a strong negative electronic contribution to the single crystal elastic constant c_{44} is predicted. This in turn modifies the shear modulus of the polycrystalline samples. The effect of adding hydrogen is to increase the Fermi level, shifting its position relative to this point, thereby modifying the electronic contribution to

$G(T)$.

Similar measurements were made on a Ti-Zr-Ni based icosahedral quasicrystal (QC) and the 1/1 bcc crystal approximant. The shear and bulk moduli of the materials were derived in a temperature range of 15 -345 K. The temperature dependencies resembled those of ordinary metals with the moduli of the QC and the approximant phase being almost the same across the temperature range of study, thus providing further confirmation of the similarity of the QC and approximant phases. These results represent the very first elastic moduli measurements on the large class of Ti-based QC systems. Both phases absorb hydrogen in solid solution up to H concentrations of $x \leq 1.7$. The ultrasonic loss of the QC and approximant phases loaded to H concentrations of $x = 0.79$ and 0.20 respectively, was measured. Strong, broad attenuation peaks were observed, centered at roughly 250 K for the hydrogenated materials and were associated with the H motion. A Gaussian distribution of activation energies was required to fit the loss data for the approximant, with a mean activation energy of 0.40 eV. The loss peaks for the QC phase were not fit to theoretical expressions as there was too much scatter in the data. However, the results clearly indicated that the H motion in the QC, in this temperature range, is at least one order of magnitude faster than that of the approximant phase. To determine whether this result is due to an intrinsic difference between the hydrogen environments of the two materials or is related to H concentration effects is unclear at present. These results were the very first internal friction measurements to be made on a hydrogenated Ti-based QC and its related approximant phase.

In the final study, RUS was applied to a project of more practical interest. The

texture, the non-random orientation of crystallites within a polycrystalline aggregate, of rolled sheets of copper and brass was investigated. Rolled sheets are generally assumed to possess macroscopic orthorhombic symmetry. RUS was used to measure all nine room-temperature elastic moduli of the plates. The values of the elastic constants were used to determine the elastic anisotropy of the sheets, and hence characterize the nature of the texture. The elastic constants were compared to theoretical expressions to determine the orientation distribution coefficients (ODC). The ODCs determined ultrasonically were in good agreement with those from neutron measurements as evidenced by the remarkable agreement between the acoustic and neutron pole figures. The results support the idea that ultrasonic techniques can be used for quantitative textural corrections of tensorial physical properties.